CHARACTERIZATION AND MODELING
OF INDUCTORS

By

Long-Ching Yeh

A DISSERTATION PRESENTED TO THE GRADUATE COUNCIL OF
THE UNIVERSITY OF FLORIDA
IN PARTIAL FULFILLMENT OF THE REQUIREMENTS FOR THE
DEGREE OF DOCTOR OF PHILOSOPHY

UNIVERSITY OF FLORIDA

1984

ACKNOWLEDGEMENTS

TABLE OF CONTENTS

Abstract of Dissertation Presented to the Graduate Council
of the University of Florida
in Partial Fulfillment of the Requirements
for the Degree of Doctor of Philosophy

CHARACTERIZATION AND MODELING
OF INDUCTORS

By

LONG-CHING YEH

December 1984

Chairman: Dr. J. Kenneth Watson
Major Department: Electrical Engineering

This dissertation presents the modeling and
characterization of inductors wound on a ferrite core, an
amorphous alloy (Metglas$^{®}$) core, a permalloy 4 mil tape
wound core and three permalloy 1 mil tape wound cores with
different kinds of heat treatment, and an MPP core. Many
kinds of measurements have been made including normal
inductance   measurements,   incremental   inductance
measurements, inductance quality factor measurements,
effective series resistance measurements, hysteresis loop
observations and measurements of waveform distortion.

All the materials studied were found to have certain
common features: the normal inductance increases as signal
amplitude increases but eventually passes through a maximum
value.   Incremental   inductance,   on   the   other   hand,   is
independent of direct current below a critical value, and
then decreases for larger values of current.

The critical d-c field for incremental inductance was found to have the same value as the peak a-c field at which there is a change of the rate of increase of normal inductance. Both critical fields may be attributed to the same physical process, the onset of irreversible motion of domain walls. This new finding, for the first time, relates normal inductance and incremental inductance measurements.

A new mathematical model for inductors is worked out using a computer curve-fitting program to describe the inductance and equivalent series resistance measured with a-c signal levels ranging from low to high amplitude. The model, which may be used to calculate the quality factor and the power loss of inductors, also explains Legg's equation in an extended form.

The voltage waveform of an inductor was found to be somewhat distorted even when the applied current is a pure sinusoid. The measured distortion was less than is predicted by a new "instantaneous" model of permeability, but was in reasonable agreement with a domain-state interpretation of the Rayleigh model.

Other findings include a critique and extension of Legg's equation, an experimental validation of a domain wall model for incremental inductance, and the recognition of a domain-wall un-pinning model to explain the increase of permeability with a-c amplitude.

CHAPTER 1
INTRODUCTION

This dissertation can be separated into two parts: in the first part we study the modeling of inductors under a-c performance. A modified model and a new model will be presented. In the second part we study the nonlinear properties of magnetic materials of inductive type with emphasis on the effects due to different magnetic reversal processes. The first part includes chapter 2 and chapter 3, the second part includes chapter 4 through chapter 9.

Device modeling for inductors is very important for magnetic circuit designers, but there are only a few models which exist. Three of them, the model by Legg [Le36], the model by Jordan [Jo24], and the model by Rayleigh [Ra87], are only applicable to small signal levels. No models has been derived for large signal performances. Yet large signal applications are important because they save expense and reduce the size and weight of devices.

A simple circuit model of an inductor consists of a resistance in series with a pure inductance, with impedance $Z = R + j\omega L$. The equivalent series resistance may usually consist of two terms,

$$R = R_w + R_{ac} \qquad (1-1)$$

where R_w is the winding resistance and R_{ac} is the core-loss resistance.

The quality factor Q, which gives the ratio of energy stored to energy dissipated per cycle, is given by

$$Q = \frac{\omega L}{R_w + R_{ac}} \qquad (1\text{-}2)$$

In general applications of inductors where Q and/or power losses are of interest, the engineer may wish to know how R_{ac} and how L vary with signal amplitude and frequency. These subjects are studied in the first part of this dissertation.

In 1936, Legg derived a relation between R_{ac} and permeability based on the classical assumptions that permeability is linear and is uniform inside the material [Le36], his final result is

$$\frac{R_{ac}}{\mu f L} = aB_m + c + ef \qquad (1\text{-}3)$$

where a is the hysteresis loss coefficient, c is the residual loss coefficient, and e is the eddy current loss coefficient.

With regard to eddy current losses this expression is derived from losses in laminations, while the hysteresis losses are obtained from the Rayleigh equation. In MKS units, $e = \pi d^2 / 3\rho$, where d is the thickness of the lamination and ρ is the resistivity of the material.

In chapter 2 we use the left hand side format of Eq.(1-3) as a basis to study the Legg model at low B_m for many inductive magnetic materials which are not limited to lamination cores.

Limitations of Legg's model are pointed out and a modified form is given. A mathematical model that shows how pure inductance and series resistance vary with f and B_m is developed. Chapter 3 describes the applications of this mathematical model for quality factor and power losses in the inductors.

The materials selected for this study are described as follows: a linear ferrite (Ferroxcube 3E2A), an amorphous alloy (Metglas® 2605SC with high frequency anneal, Fe 81%, B 13.5%, Si 3.5%, C 2%)), and a permalloy 4 mil tape wound core with special anneal (Magnetic Metals: core size 1321; Ni 80.5%, Mo 4.6%, Fe and impurities 14.9%; core #6), a powder permalloy (Magnetics, MPP 160 μ), and three special annealed permalloy 1 mil tape wound cores made by different annealing processes (HYMU 80, core #1, #8, #14).

All of the materials are in toroidal geometry possessing no air gap (except MPP), a geometrical shape which exposes the intrinsic material properties most simply.

All these materials are of commercial importance and are interesting both for physicists and engineers [Ma80,Kr79,Ts79,Na80,Bo81].

The electrical models we derived in chapter 2 and 3 are relevant to such a broad class of materials as described

above; thus the models might be applicable to all inductor cores without airgap.

After concluding the first part of this study (inductor electrical model, chapter 2,3), this dissertation concentrates on the characterization of inductive magnetic core materials. The following introduction is given for the study in this area.

The materials mentioned above are "soft" magnetic materials of "inductive" type. The outstanding properties of these materials is the ease with which their intensity of magnetization can be varied. The term "soft" refers to a large response of the magnetization to a small applied field. The term "inductive" means that the materials have low remanence; thus their B-H characteristics are predominately sloping, so that the concept of permeability $\mu = B/H$ is meaningful.

From a technical point of view, the most important region of the magnetization of this kind of material is that below the "knee," as shown in Fig. 1-1, but it is unfortunately just this region that is most difficult to interpret, since the processes involved depend on small irregularities in the material. The magnetization processes also depend on the domain arrangements as well as the factors that determine the easy directions of magnetization. The magnetic response of the material, thus, shows nonlinear and hysteresis nature. The second part of this dissertation studies in this area.
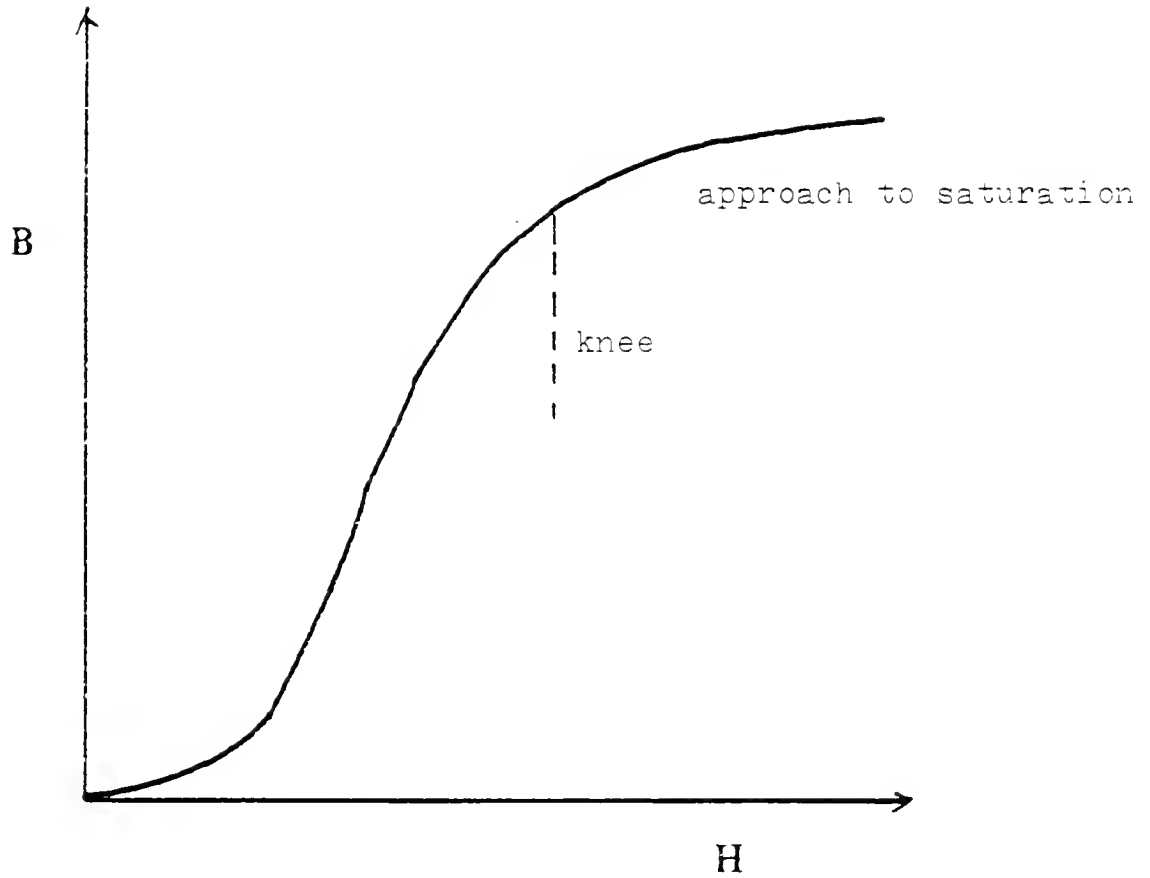
Fig. 1-1 A representative magnetization curve of an
          "inductive" magnetic material.

In a recent study [Wa81], Watson carried out some exploratory work on linear ferrites, investigating the non-linear responses of ferrite cores to a variety of electrical measurements. At large signal levels, there is generally poor agreement between reversible permeability, normal permeability, and pulse permeability. In a theoretical model, he assumed that reversal takes place by rotational processes and assumed that the core saturates at a specific field, he found that actual measurements of ferrite response do not fit the model. Puzzling aspects were part motivation for these research.

Domain theory plays a very important role in the study of nonlinear behavior of magnetic materials. In 1907, Weiss [We07] introduced the great concepts of domain hypothesis and the spontaneous magnetization by molecular field. For a period of nearly forty years, investigators made virtually no application of domain concepts in attempting to explain the nonlinearity or the mechanism of magnetic hysteresis. It was not until 1949, when Williams, Bozorth and Shockley [Wi49] published their work on the experimental evidence of domain structure of a real material, that domain theory became absolutely central to any discussion of nonlinearity and hysteresis of materials. Chapter 8 and 9 use the domain theory to explain the experimental results of normal inductance and incremental inductance.

The study of nonlinear properties of magnetic materials in general falls into two categories of approach: physical theory and empirical modeling.

The theoretical approach in general consists of two methods: one is based on arbitrary natural assumptions, like that of Preisach-Neel model [Pr35]. The other method, which is theoretically more sound, is based on the micromagnetic theory, like those of Brown [Br59] and Aharoni [Ah59]. However, these methods do not yield a simple equation of state for a ferromagnetic. In recent study [Ji83], Jiles and Atherton published their work on the theory of ferromagnetic hysteresis based on a mean field approximation in which each domain is assumed to interact with the field H and a weighted mean of the bulk magnetization. However in their derivation of the theory, they did not take into account how different reversal processes can influence the response of the material.

Using the empirical method, there have been many attempts to fit equations to actual magnetization data [De80,Ri81,Ma73]. However, no single equation has been developed to describe all the data satisfactorily: Attempts to describe the behavior of ferromagnets have always been handicapped by their restriction to only narrow ranges of field. For example, according to the review by Cullity [Cu72], there are only three instances where the magnetization curve can be explained by algebraic expressions. These are the high field magnetization curve of single crystals as

in the work of Williams [Wi37], the high field magnetization curves of polycrystals which are governed by the law of approach to saturation as indicated by Chikazumi [Ch64], and the low fields magnetization curves of polycrystalline specimens which exhibit Rayleigh loops [Ra87].

In this study, instead of using the above methods of research, we first characterize the materials empirically, and then seek the evidences of the effects of different reversal processes on the nonlinear properties of the materials.

Three kinds of measurements were used to characterize the materials. They are normal inductance measurement, incremental inductance measurement, and hysteresis loop observation. The relationships of the nonlinear responses under these three kinds of measurements for each material will be given. We hope the relationships we have found can help us to understand the nonlinear properties of the materials in application.

It is well known that there are three important types of reversal processes that account for the magnetization of a material by domain theory: (1) reversible boundary displacement, (2) irreversible boundary displacement, and (3) reversible rotation. To identify the effect of different reversal processes, one needs to know the critical field at which different reversal processes begin to involve.

In addition, device geometry can cause nonlinear response in application [Wa80]. Thus to characterize the

intrinsic properties of the magnetic material, one needs to take into account the geometry effect. This effect is considered when we explain the transition regions around the critical fields of normal inductance and incremental inductance in chapter 7.

In characterization of the material, since our purpose is to study the intrinsic properties of the material, we selected a set of measurements which are made at low frequency. These measurements exclude the errors due to parasitic capacitance and to the eddy current shielding effect in which the applied field can not penetrate completely through the whole magnetic material.

In chapter 4 we present the data of normal inductance; chapter 5 presents results for incremental inductance measurements. In chapter 6, we characterize the materials by B-H observations. Chapter 7 investigates the relationships among normal inductance, incremental inductance and B-H loops for each core. A model that accounts for the change of mode of reversal around the threshold fields is presented. Chapter 8 and chapter 9 proposes physical mechanisms to explain the experimental results. In the beginning of chapter 8, the distortion mechanisms of V-I relation due to nonlinear B-H relation are studied first in order to lay a foundation for a proposed physical model for normal magnetization. Chapter 10 gives conclusions of this research.

The following formulae are used for our core testing, which are usually used in electrical engineering.

$$V_{rms} = 4.44 \times B_m ANf \times 10^{-8} \qquad (1-4)$$

where

B_m = Peak flux density in gauss

N = Turns

A = Effective core area in cm^2

f = Frequency in Hz

Equation (1-4), Faraday's law, allows one to determine at what voltage to excite a core for measurement at a certain flux density. This equation is valid only when the signal waveform is sinusoidal and is usually used when the signal level is low.

$$H = NI/l_m \qquad (1-5)$$

where

H = Field strength in A/m

l_m = Mean path length in meter of toroidal core

Equation (1-5) allows one to determine at what current to excite a core for measurement at a certain field strength.

$$\mu = B/H \qquad (1-6)$$

where

B = Flux density in Tesla

H = Field strength in A/m

$$L = \frac{N^2 \mu A}{l_m} \qquad (1-7)$$

Equation (1-6) and (1-7) determine amplitude permeability, μ, ($\mu = \mu_0 \mu_r$, μ_r is relative permeability). The amplitude permeability is a parameter which is determined by measuring inductance; permeability is calculated using equation (1-7).

$$L = N^2 P. \qquad (1-8)$$

where

L = Inductance in Henries

P = Permeance in Henry/turns squared

Equation (1-8) defines inductance from the permeance, P. For a toroidal core without air gap, $P = \mu A / l_m$. In Eq.(1-8), given the P, one can either calculate the inductance or determine the turns needed if the inductance is known.

CHAPTER 2
MODELING OF INDUCTORS

In this chapter, measurements of inductance, L, series resistance, R, and quality factor, Q, are made for five different magnetic cores. Data are analyzed as a function of B_m and frequency.

The Legg's coefficients for each core are presented. The limitations of Legg's equation are indicated; Legg's equation is modified to extend its vadility of application. An empirical mathematical model of pure inductance and loss resistance as a function of frequency and B_m is given for higher B_m application. The relation of this model to Legg's model is shown.

2.1 Introduction

This chapter presents the results of a study on the model of an inductor when signal level varies from low to high. Equation (1-3) is used as a basis for an empirical determination of the coefficients for five different magnetic materials that are suitable for inductors. They are a ferrite, an amorphous Metglas[c] with high frequency anneal, a 4 mil tape wound core with special anneal (core #6), an MPP core, and a permalloy 1 mil tape wound core with tranverse magnetic anneal (core #8).

Experimental values for the Legg coefficients calculated for each core material are given. The limitations of the Legg coefficients to the modeling of the five magnetic materials are also examined.

A mathematical model is used to describe how the Legg coefficients vary with B_m and frequency. This model is based on the observation that inductance was found initially to increase as B_m increases, and that R_{ac} was found to increase with frequency and B_m. The parameters of the model were derived with a computer curve fitting program. This model also lays the foundation for the analytic expression of Q factor and power losses in an inductor.

2.2 Measurements and Calculations

Measurements of inductance, R, and Q were made using an HP 4274A LCR meter in the frequency range from 100 Hz to as high as 100 KHz in some cases. Measurements were made for specified values of B_m according to Eq.(1-4) by keeping V/f constant. The measured data were manipulated into the format of the left side of Eq.(1-3), and then were analyzed by B_m and frequency in order to determine the Legg coefficients. In the analysis, permeability was allowed to vary with B_m and with f (permeability is defined by Eq.(1-7)). Thus we actually worked

$$\frac{(R-R_w)n^2A}{fL^2 l_m} = aB_m+c+ef \qquad (2-1)$$

for each data point as the left hand side of Eq.(1-3), where A is the core cross section and l_m is the mean path length. When the values of Eq. (2-1) are plotted against frequency, the slope is interpreted as coefficient e; extrapolation to zero frequency gives intercept aB_m+ c. Constants a, c can be determined from the family of intercept values for different values of B_m. Figure 2-1 illustrates this processes for ferrite data in which coefficient e is found. Figure 2-2 shows the same process for Core #8. Figure 2-3 and 2-4 shows the processes to determine the coefficients a, c for ferrite and core #8 separately.

The same procedure was carried out for each of the other four core materials that were studied, with the results summarized as Legg coefficients a, c, in Table 2-1. Coefficient e_0 will be explained later. The table also gives the range of frequency and of B_m. The value of B_m indicates where the intercept (aB_m + c) begins to depart from linear dependence on B_m.

The low frequency limitations of Table 2-1 were imposed by the accuracy of determining R_{ac} by subtraction, see Eq.(1-1). At low frequencies where core losses are small, the measured R hardly exceeds the winding resistance especially for ferrite and for MPP cores. The high frequency limit indicates the approximate value of frequency at which a curve such as in Fig. 2-1 begins to deviate from linearity to become concave down.
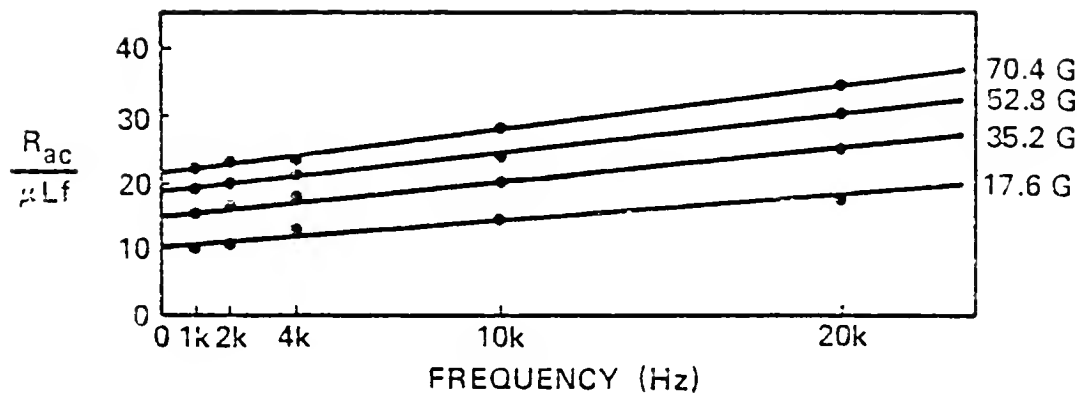
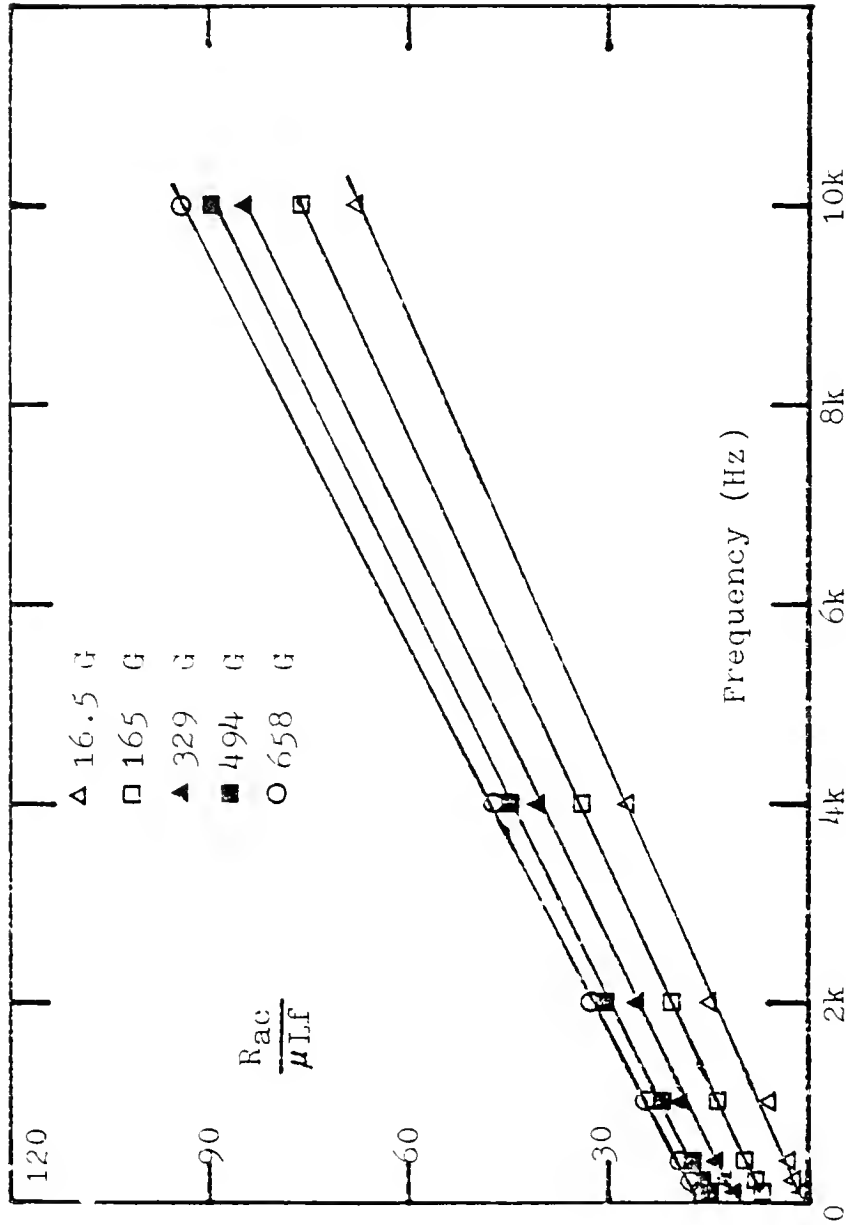Fig. 2-1 $R_{ac}/\mu Lf$ vs frequency at various B_m for ferrite.

Fig. 2-2 $R_{ac}/\mu Lf$ versus frequency at various B_m of core #8.
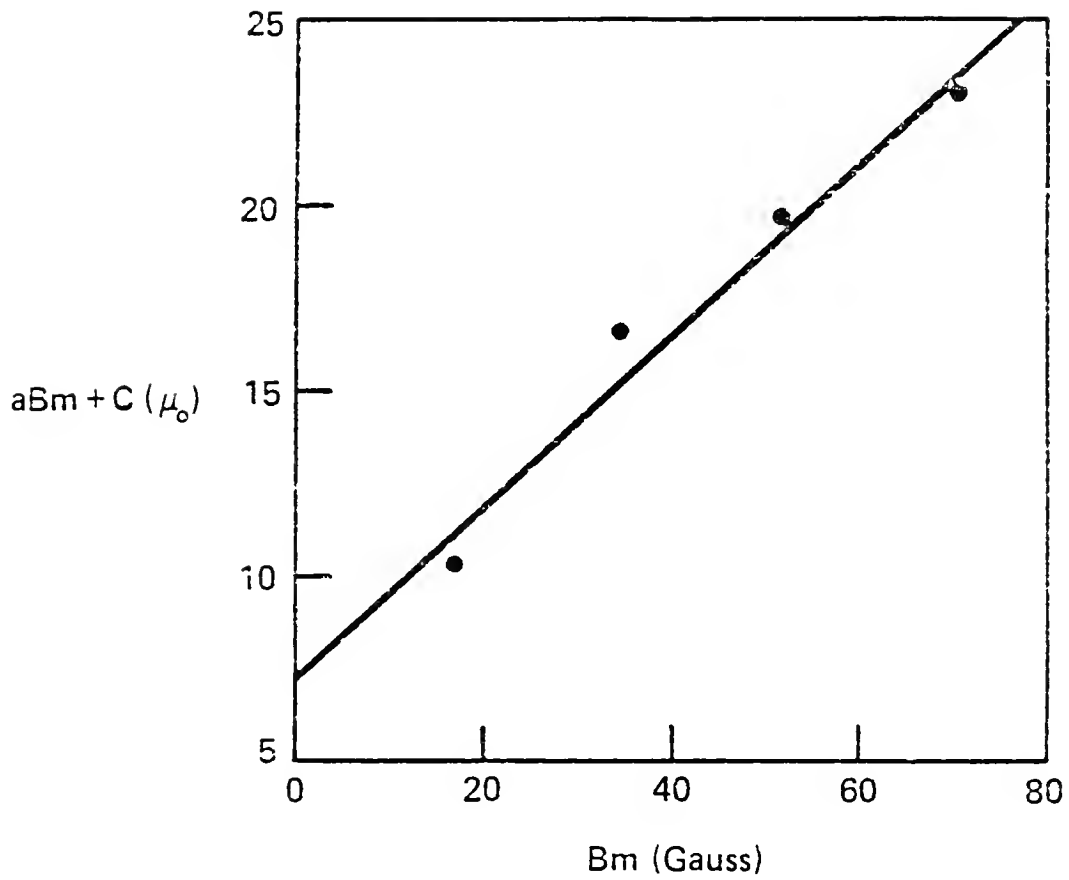
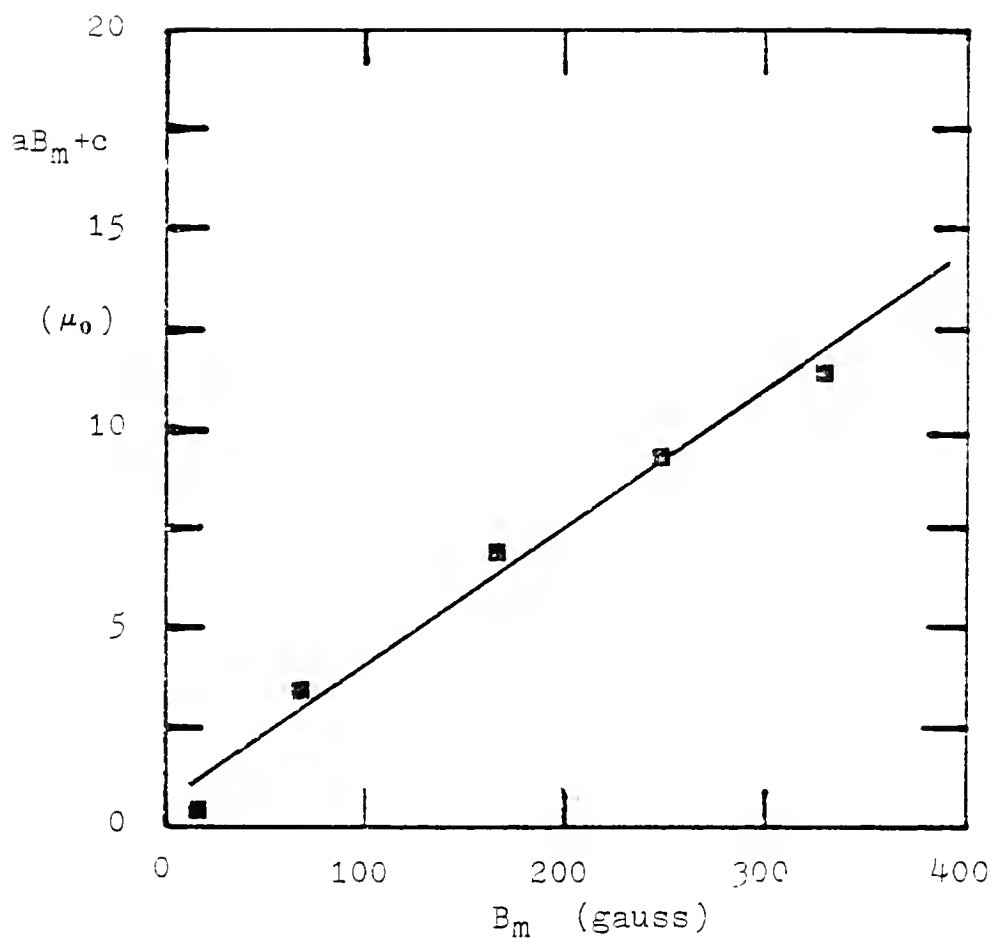Fig. 2-3   Intercepts (at f=0 from Fig. 2-1) vs B_m. (ferrite)

Fig. 2-4 $aB_m + c$ vs B_m of core #8 at low field range.

Table 2-1   Legg coefficients for five magnetic materials.

Core Material	Coefficients			Data Region	
	a	c	e_0	f	B_m, Gauss
Ferrite 3E2A (768-T-188)	2.6×10^{-7}	9.2×10^{-6}	4.3×10^{-10}	$1k < f \leq 20k$	≤ 70
Amorphous Alloy Metglas 2605 SC (T-889-4)	5.3×10^{-8}	6.2×10^{-6}	5.3×10^{-9}	$f \leq 20k$	≤ 300
Permalloy 4 mil Special Anneal Core #6	2.9×10^{-7}	1.0×10^{-6}	9.0×10^{-8}	$f \leq 4k$	≤ 20
MPP Core (S6B-55252-A20)	2.4×10^{-6}	2.7×10^{-5}	1.8×10^{-8}	$4k < f \leq 40k$	≤ 10
Permalloy 1 mil Special Anneal Core #8	5.3×10^{-8}	6×10^{-8}	8.4×10^{-9}	$1k < f \leq 10k$	≤ 400

2.3 Limitations of Legg's Model and Modified Model

When the family of curves of Fig. 2-1 or 2-2 is exam-
ined carefully, it may be observed that the lines are not
exactly parallel. The slopes are found to increase slightly
with B_m, as shown in Fig. 2-5. A similar variation was also
found for all the core materials, with core #8 as another
example, as shown in Fig. 2-6. Others are not shown here.
The intercept at $B_m=0$ for the figure of e versus B_m is the
coefficient e_0, listed in Table 2-1. In the data range of
study, this variation of slope was found significant for
ferrite, core #6, core #8 and MPP core. For this reason,
data for these three materials may be modeled more accu-
rately by modifying the e term of the right side of Eq. (1-
3). Thus we modify the Legg's equation as follows:

$$\frac{R_{ac}}{\mu f L} = aB_m+c+e(1+dB_m)f \qquad (2-2)$$

For the geometries and turns used, coefficient d was
found to be 1.37×10^{-2} for ferrite and $d = 2.33 \times 10^{-3}$ for
core #6, 2.52×10^{-4} for core #8 and 2.13×10^{-3} for MPP. Only
negligible dependence was observed for Metglas in the range
of the study.

It is of interest to compare the results of Legg coef-
ficients we worked out for MPP core with catalog data, which
data were found only for the MPP core: $a = 0.9 \times 10^{-6}$, $c =
2.5 \times 10^{-5}$, $e = 1.7 \times 10^{-8}$ for $\mu = 160$ (suitable below 200 g,
frequency limit unspecified). Our results agree within
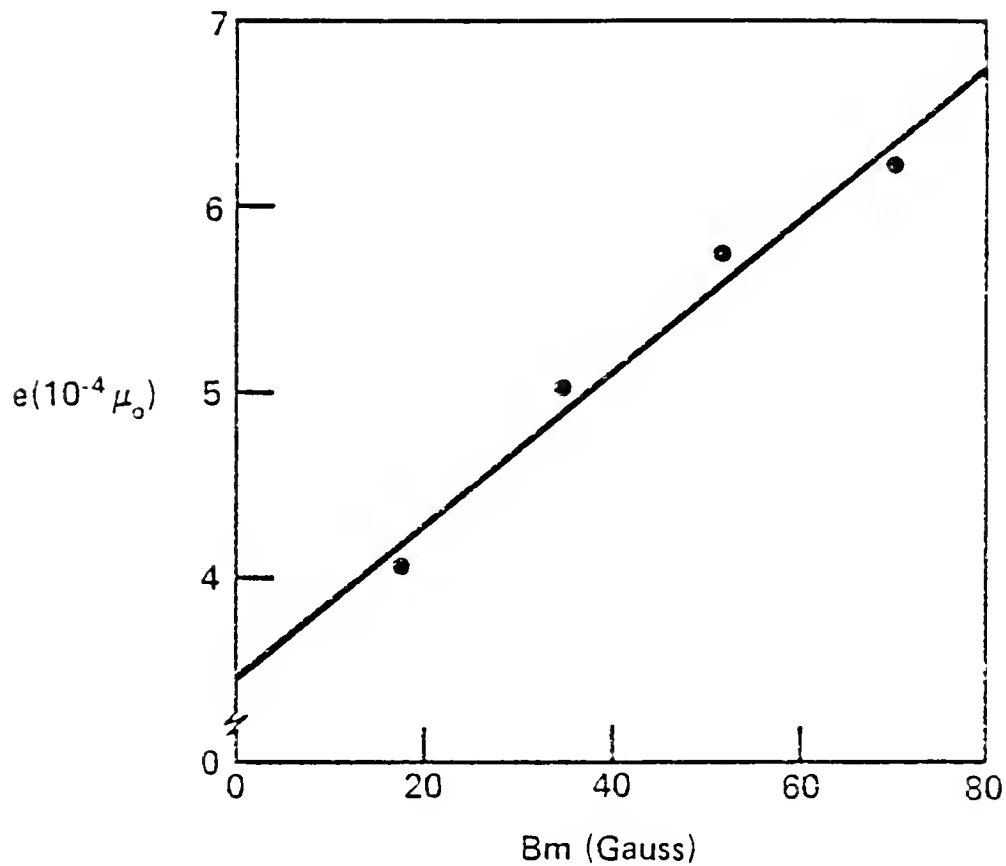
Fig. 2-5 Slopes (of lines from Fig. 2-1) vs B_m interpreted as e. The line is a linear regression with e_o = 3.4 x 10-4 μ_0 d = 4.67 x 10-6 μ_0 .
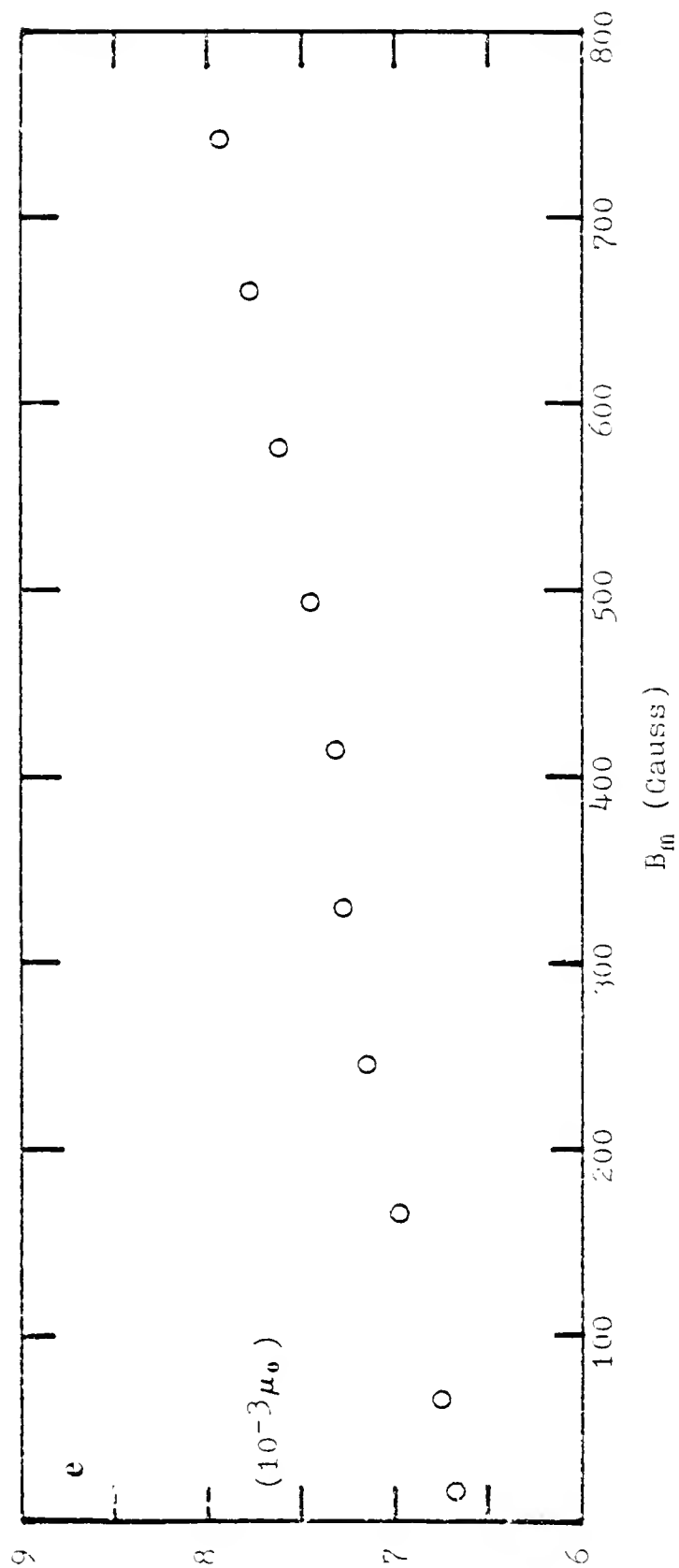
Fig. 2-6 Slopes (of lines of Fig. 2-2) vs B_m interpreted as coefficient e.

about 5 percent for e, c but are about 3 times higher for the hysteresis coefficient, a.

The more serious limitation of the Legg data is the low range of allowed induction, B_m. When the measuring induction B_m is increased beyond the listed value of Table 2-1, the value of (a B_m + c) is found to deviate from a linear relation with B_m. The data points of Fig. 2-7 and of Fig. 2-8 illustrate this effect and thereby raise the question whether the value of coefficient a is valid. The only approximate agreement of Fig. 2-7 with the data of Fig. 2-3 raises the additional question whether our procedure Eq.(2-1) leaves the term a entirely independent of the number of turns as it should be. For the high-field measurements of Fig. 2-7, n =40, whereas more turns (n =100) were used for the low field measurement of Fig. 2-3. The values of e versus B_m also show two different slopes at two different numbers of turns, as can be seen from Fig. 2-9 for ferrite as an example. Figure 2-10 shows another example the effect of number of turns on the value of aB_m + c for Metglas, thus the Legg coefficient a and coefficient d seem to be dependent on the number of turns of winding.

It interesting to note that although both the slope of aB_m + c and the slope of e as a function of B_m increase as n increases, as has been shown in Figs. 2-7, 2-9 and 2-10, their intercepts at B_m seem to be independent of the number of turns. This suggests that the coefficients c and e_0 might be independent of the number of turns.
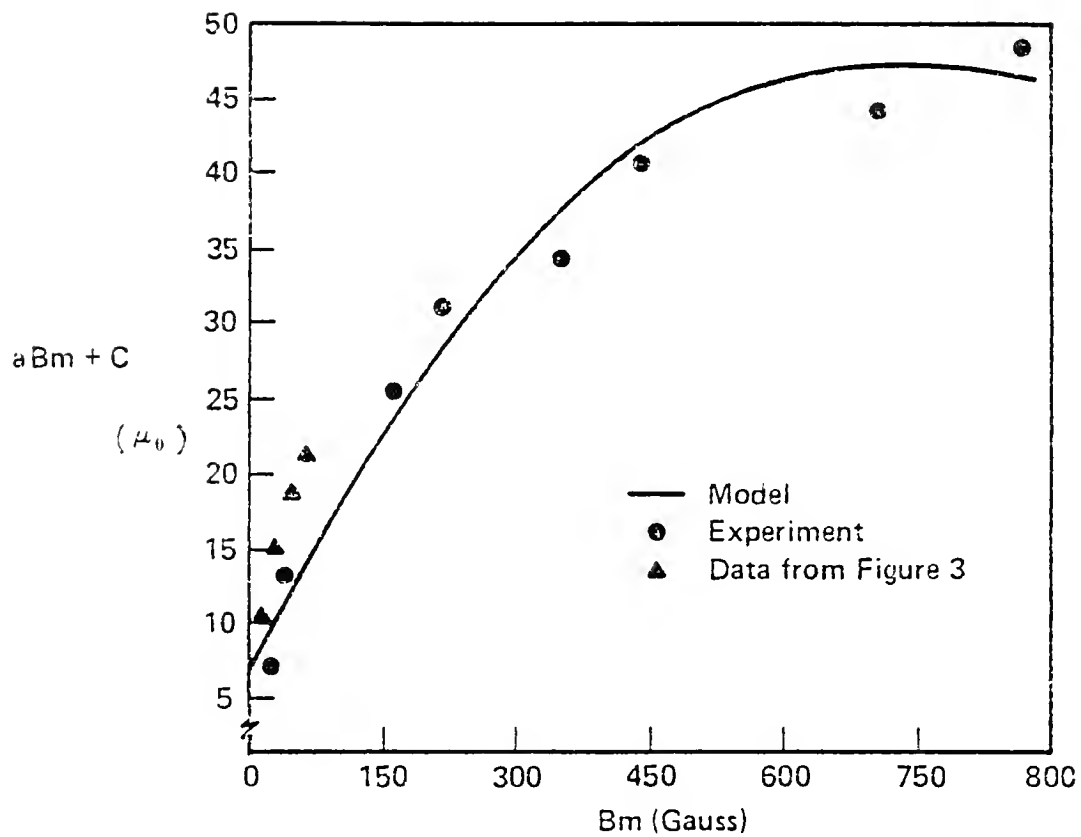
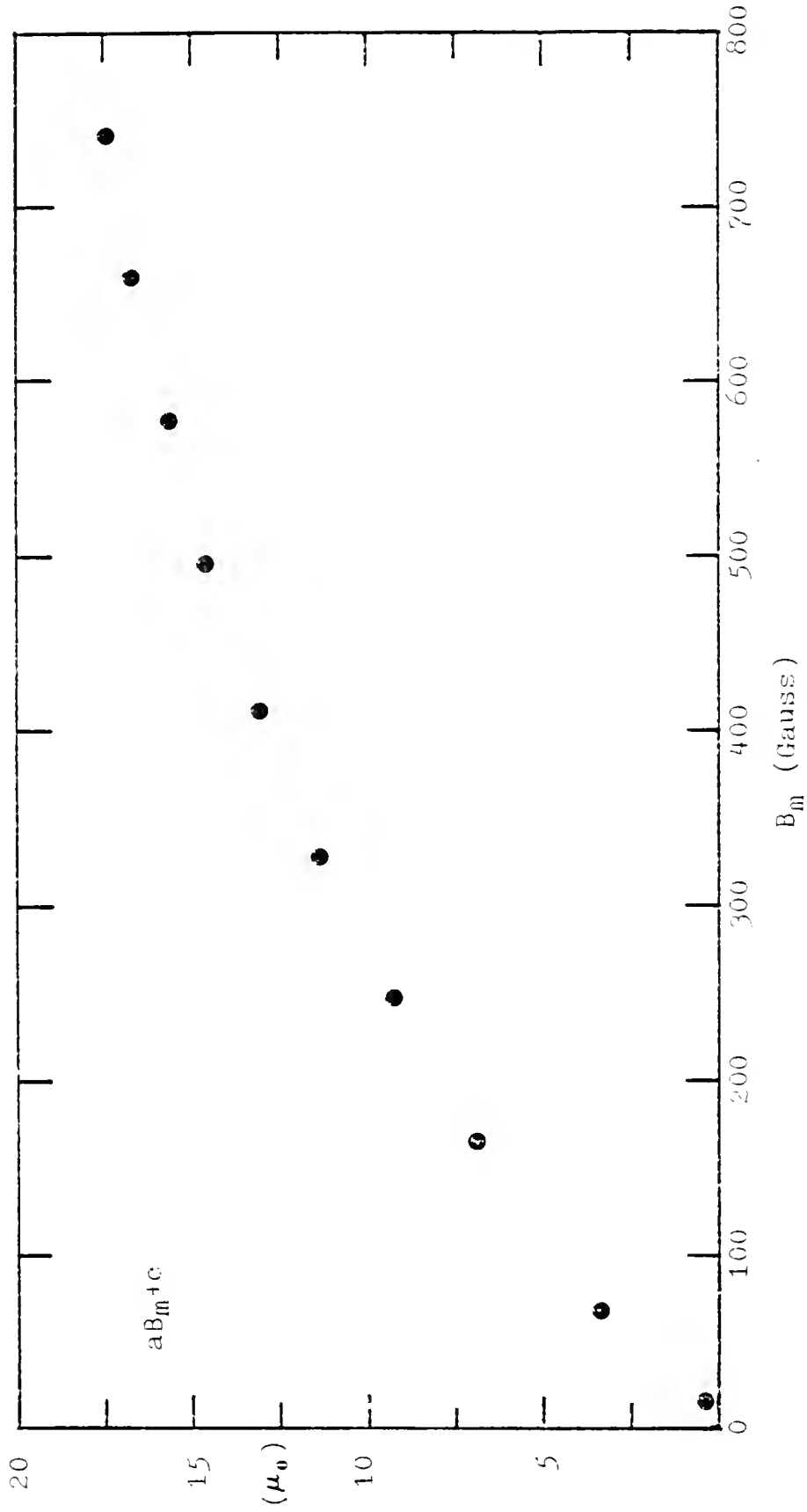Fig. 2-7 $(aB_m + c)$ vs B_m. (ferrite)

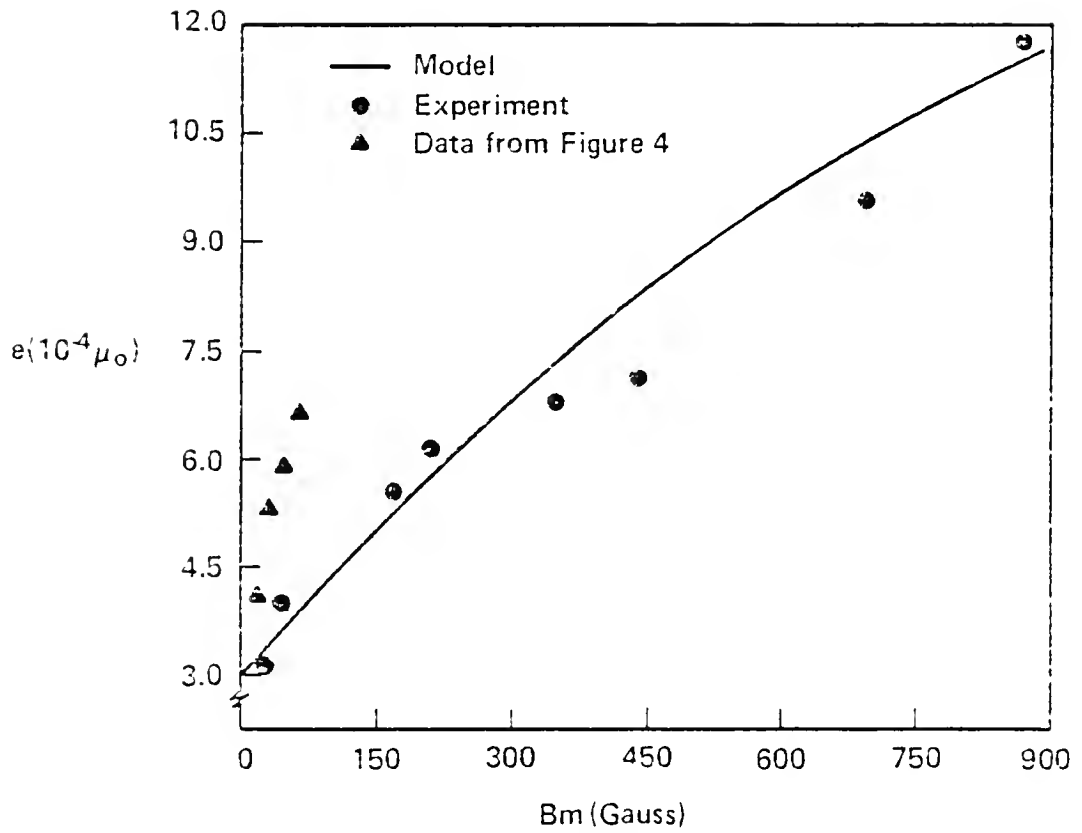Fig. 2-8 $(aB_m + c)$ vs B_m. (core #8)

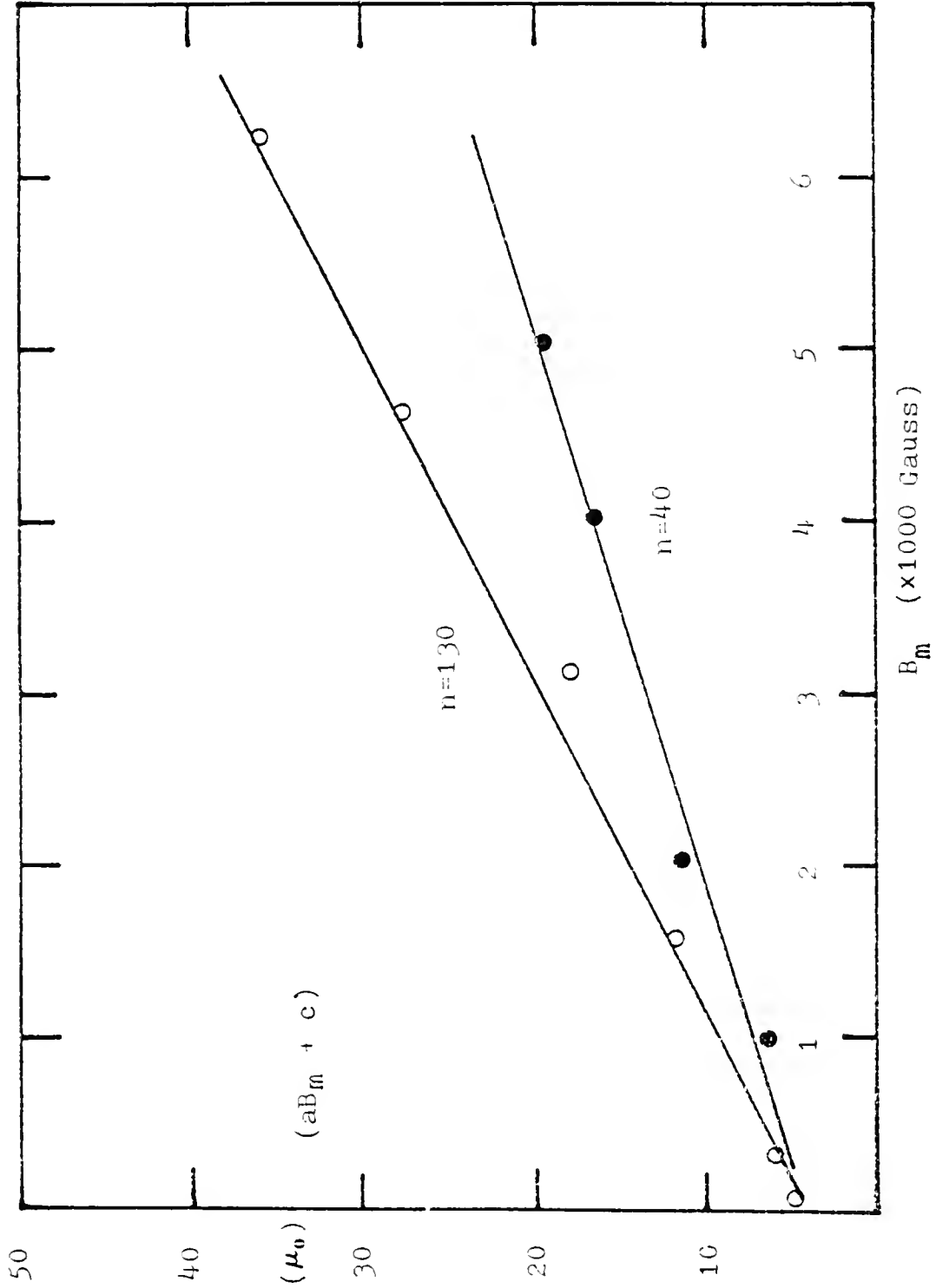Fig. 2-9 Coefficient e versus B_m. (ferrite)

Fig. 2-10 $(aB_m + c)$ vs B_m for Metglas at two different numbers of windings.

In the next section, presentation is made on an analytic model (results from a rather preliminary model) for lossy inductors that seems to be valid over a wider range of B_m as compared to the Legg coefficients. The model gives an interpretation of the Legg coefficients and also sheds light on the frequency and B_m dependence of quality factor, Q, and of power loss, P, which will be described in chapter 3.

2.4 A New Mathematical Model for Lossy Inductors

A new model is now proposed to represent a lossy inductor.

Normal inductance typically increases with the amplitude of the measuring signal, and is modeled here as

$$L = L_0(1+bB_m) \qquad (2-3)$$

where L is initial inductance and where coefficient b is the model parameter of interest. This trend was observed for all five materials of the present study: Figure 2-11 and Fig. 2-12 show typical results for ferrite and Metglas core as examples; others are not shown here.

The effective series resistance of an inductor may be represented as a series in powers of frequency, so that Eq.(1-1) becomes
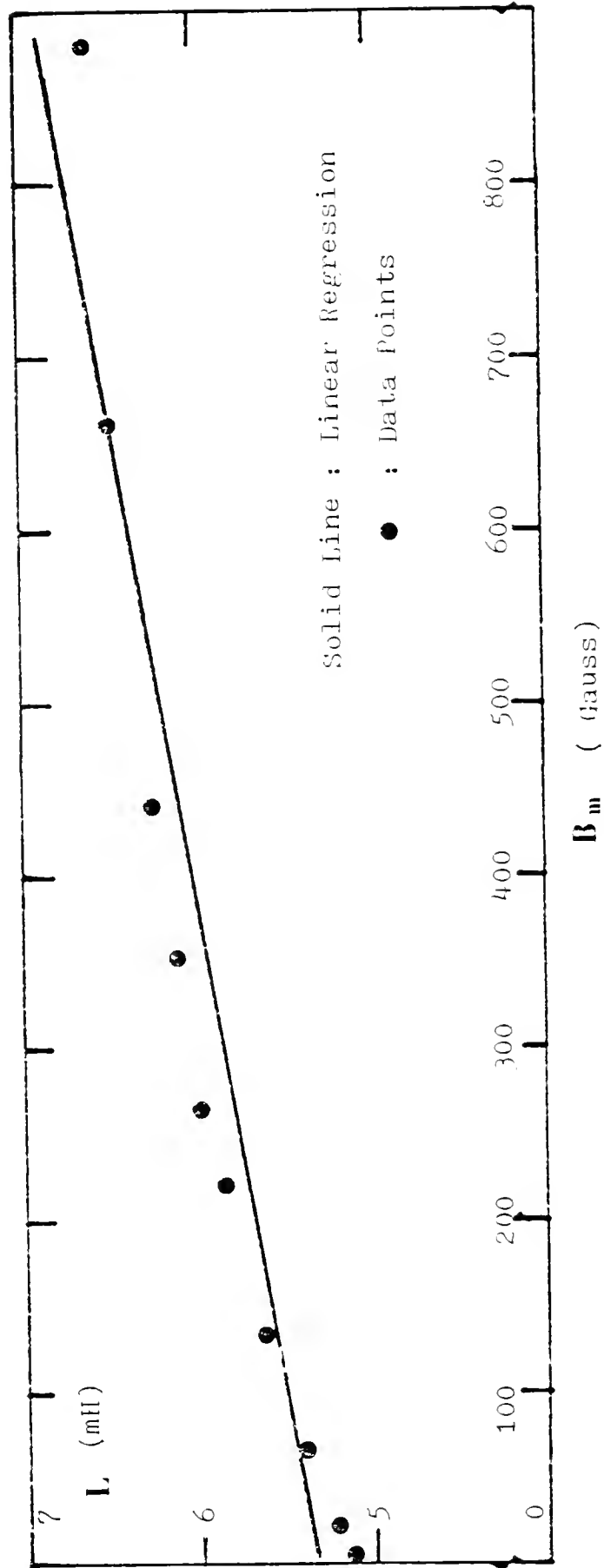
$$R = r_0 + r_1 f + r_2 f^2 \qquad (2-4)$$

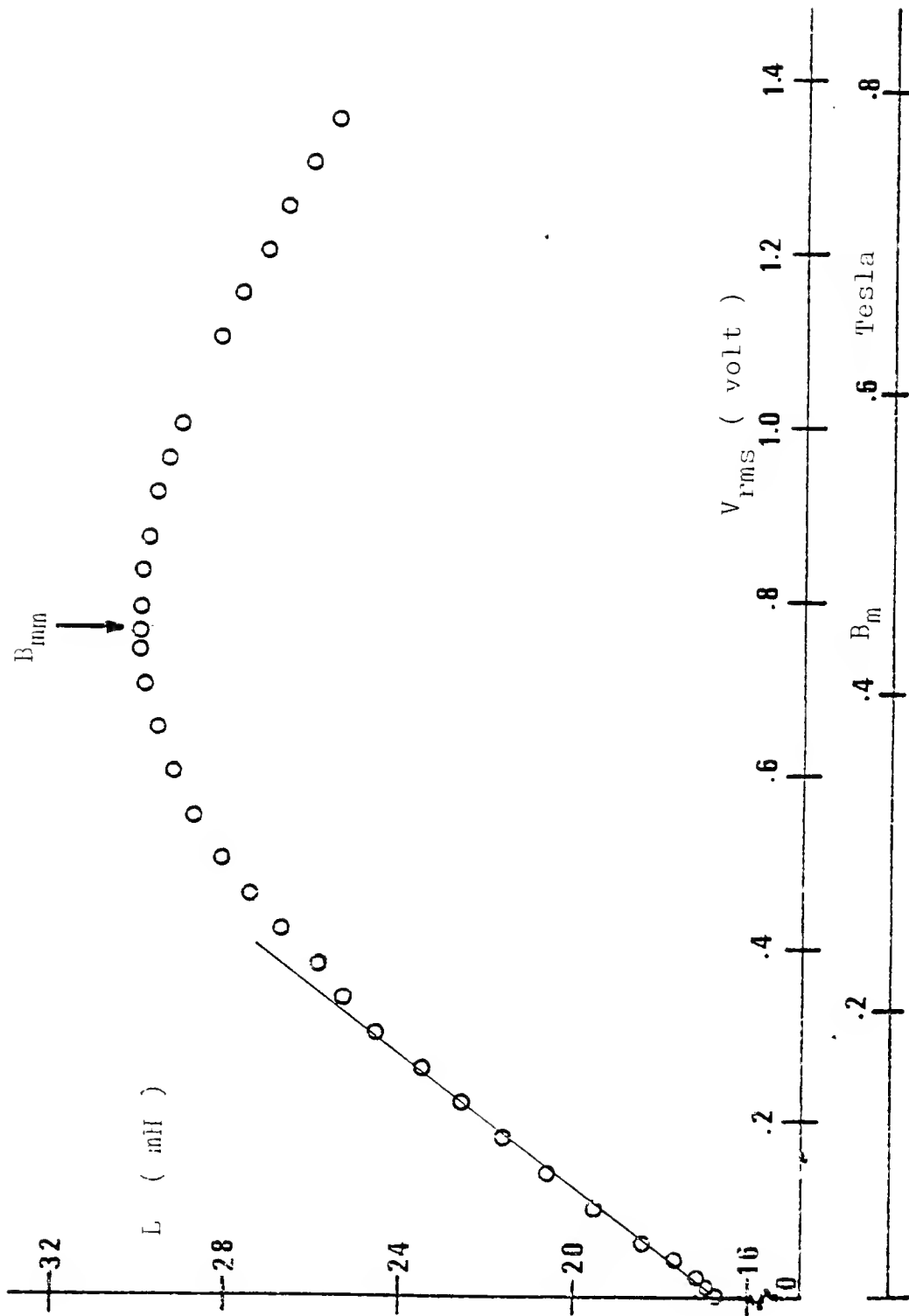Fig. 2-11 Normal inductance of ferrite core as a function of B_m.

Fig. 2-12   Normal inductance as a function of B_m.   (Metglas, n=70)

where r_0 is identified as the winding resistance R_w and thus the two higher order terms define the core loss parameter R_{ac}. A curve-fitting computer program was used to process our measured data for R using the format of Eq. (2-4), which turned out to match with our data very well. Figure 2-13 shows a calculation compared with data for the ferrite core inductor at B_m = 44 G, plotted vs frequency.

The coefficients resulting from the Eq.(2-4) analysis were found to vary with B_m (in units of gauss) and can be represented as

$$r_1 = r_{10} + r_{11}B_m + r_{12}B_m^2 \tag{2-5}$$

$$r_2 = r_{20} + r_{21}B_m \tag{2-6}$$

where again the coefficients were identified using the computer curve-fitting program, as shown in Figs. 2-14, 2-15. In summary, the model consists of Eqs. (2-3) through (2-6) for which the resulting coefficients are listed in Table 2-2 for three of the five materials. Due to the frequency limitation of the instrument, data for core #6 and Core #8 are not listed.

2-5 Relation of Model to Legg Equation

When model Eqs.(2-3) through (2-6) are substituted into Eq.(1-3), the Legg equations (1-3) and (2-1) take the form, with $k=n^2 A/l_m$, and omitting B_m^2 terms to simplify our analysis:
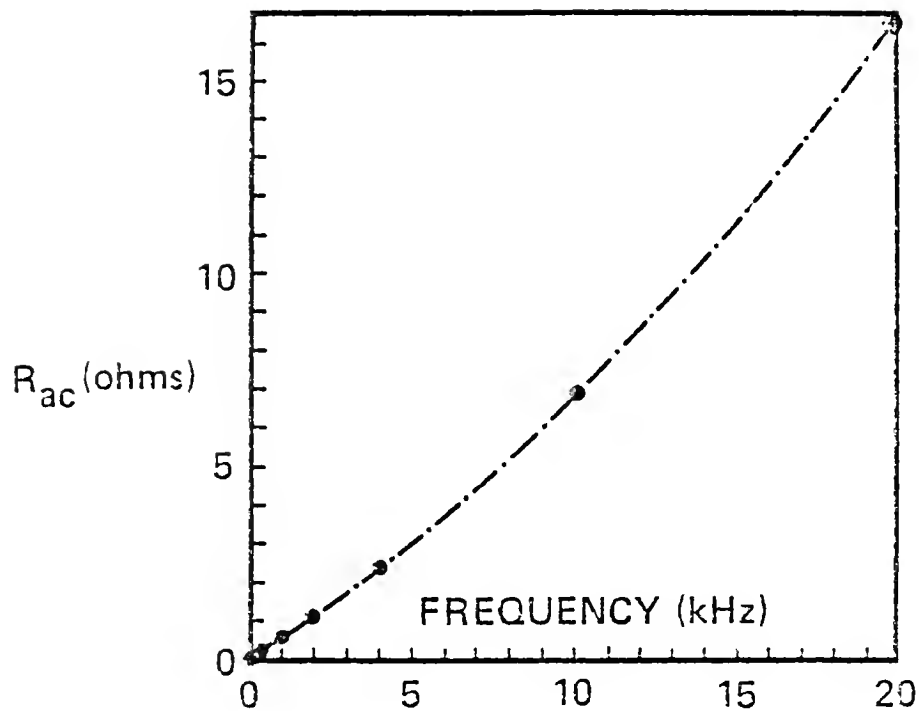
Fig. 2-13 R_{ac} vs f for ferrite inductor.
Dot points are measured data. curve is
calculated with $r_1 = 5.033 \times 10^{-4}$ and
$r_2 = 1.675 \times 10^{-8}$.
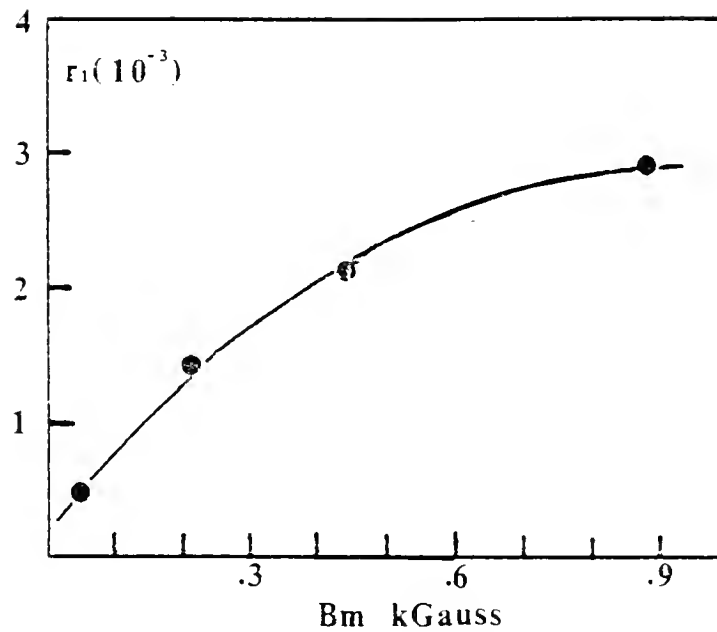
Fig. 2-14 Parameter r_1 vs B_m for ferrite core. Curve is calculated by model.
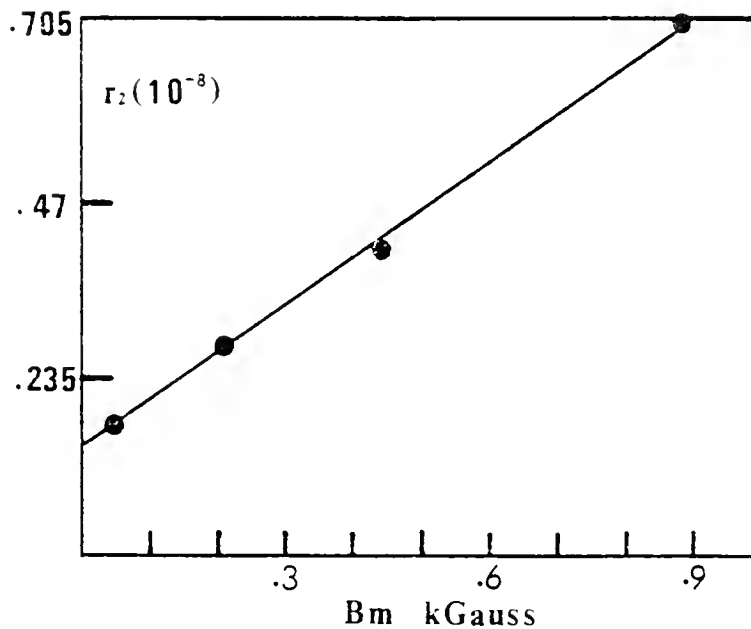
Fig. 2-15 Parameter r_2 vs B_m for ferrite core. Curve is calculated by model.

Table 2-2 Model parameters for three cores.

Parameter	Material		
	Ferrite	Metglas[c]	MPP Core
b	1.7×10^{-4}	$2.1 \times^{-4}$	6.3×10^{-5}
r_{10}	2.8×10^{-4}	1.2×10^{-4}	2.1×10^{-5}
r_{11}	5.7×10^{-6}	1.8×10^{-6}	1.8×10^{-6}
r_{12}	3.0×10^{-9}	0	0
r_{20}	1.4×10^{-8}	1.6×10^{-7}	3.0×10^{-8}
r_{21}	6.4×10^{-11}	1.1×10^{-10}	0
k	6.94×10^{-1}	6.37×10^{-1}	48.04

$$\frac{R_{ac}}{\mu L f} = \frac{r_1 + r_2 f}{L_0^2 (1 + b B_m)^2} k =$$

(2-7)

$$\frac{(r_{10} + r_{11} B_m) + (r_{20} + r_{21} B_m) f}{L_0^2 (1 + 2 b B_m + b^2 B_m^2) / k}$$

After some manipulation and assuming $2 b B_m \ll 1$, the right side of Eq. (2-7) takes the form

$$(a_0 + a_1 B_m - a_2 B_m^2) + (e_0 + e_1 B_m - e_2 B_m^2) f$$

(2-8)

which is a generalization of Eqs. (2-1) in which the actual Legg coefficients may be identified as

$$c = a_0, \quad a = (a_1 - 2 a_2 B_m), \quad e = e_0, \quad d = (e_1 - 2 e_2 B_m) / e_0.$$

(2-9)

The a and e parameters may be found from Eq. (2-7) as below, if each right side is multiplied by k/L_0^2

$$a_0 = r_{10}, \quad e_0 = r_{20}$$

(2-10a)

$$a_1 = (r_{11} - 2 b r_{10}), \quad e_1 = (r_{21} - 2 b r_{20})$$

(2-10b)

$$a_2 = 2 b r_{11}, \quad e_2 = 2 b r_{21}$$

(2-10c)

In Fig. 2-7, the smooth curve identified as the mathematical model is Eq. (2-8) plotted for $f = 0$, which is the a-series part of Eq. (2-8). The e-series multiplier of f in Eq. (2-8) is shown in Fig. 2-9 as the smooth curve. The new model is therefore consistent with a generalized form of the

Legg equation and is evidently applicable over a wider range of B_m. However, we have not addressed the problem of presenting the model in a form that is assured of being independent of geometry and of turns.

It is interesting to compare the data of e and the data of $aB_m + c$ as a function of B_m of the five materials, which are plotted as a function of f in log-log scale in Fig. 2-16 and Fig. 2-17. Core #6 has the highest e value; ferrite has the lowest e of the five; however, the e value of ferrite as a function of B_m increases sharply as B_m increases. Figure 2-17 shows that MPP core has the highest aB_m+c loss, while core #8 has the lowest aB_m+c loss of the five. The residual losses of core #6 and core #8 are very small.

2.6 Conclusion

An experimental investigation has been carried out on inductors wound on five different kinds of magnetic core materials, yielding values for their Legg coefficients that are listed in Table 2-1. These data may be interesting in their own right although they were found to be limited to low values of B_m. Legg's equation can be modified by adding a cross product term to the right side of Eq.(1-3) to increase its accuracy of application even when B_m is low.

A mathematical model of inductance and of R was evaluated for three of the five inductors, using a curve-fitting computer program to find coefficients to match the
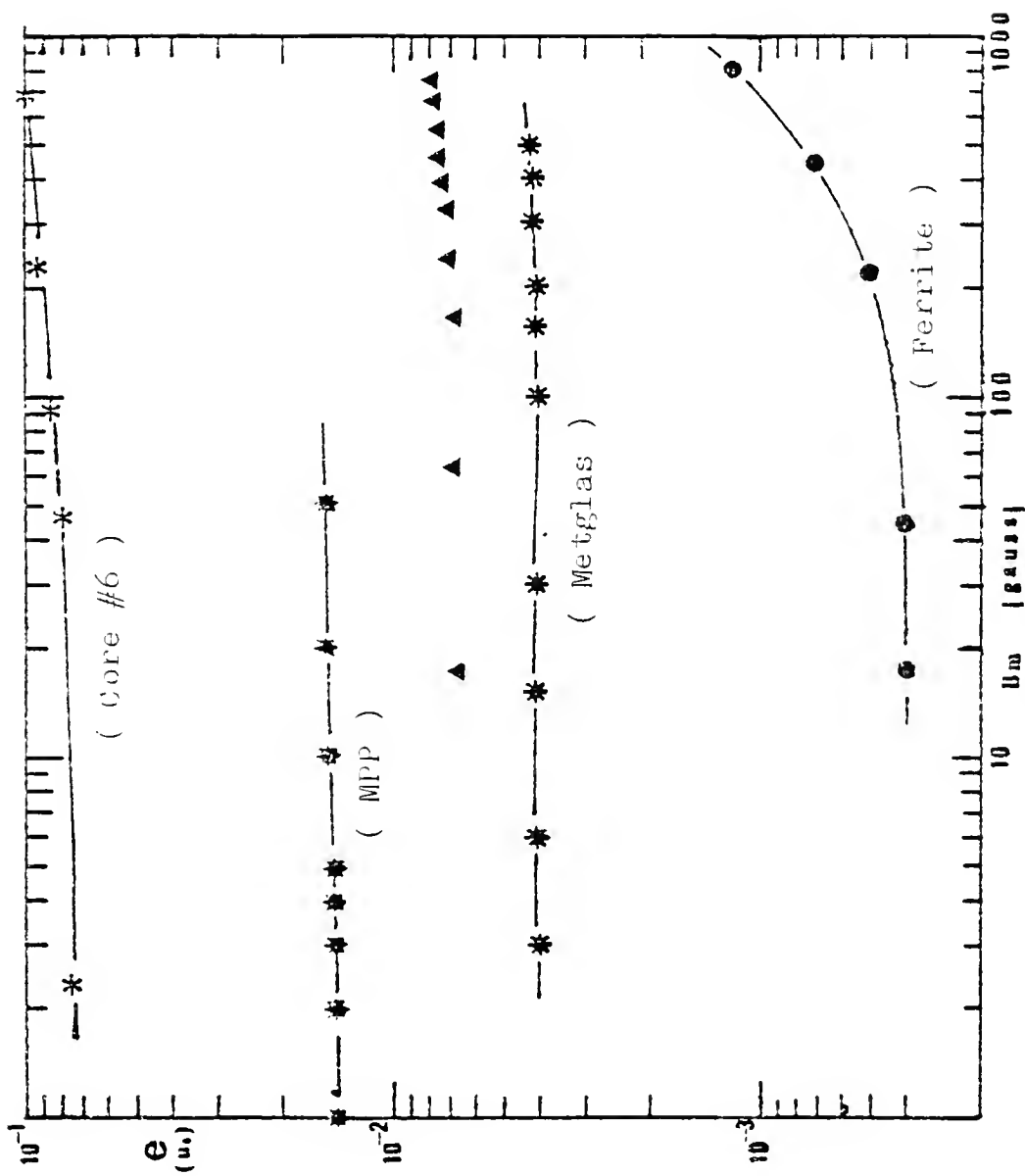
Fig. 2-16 Coefficient e as a function of B_m for five materials.
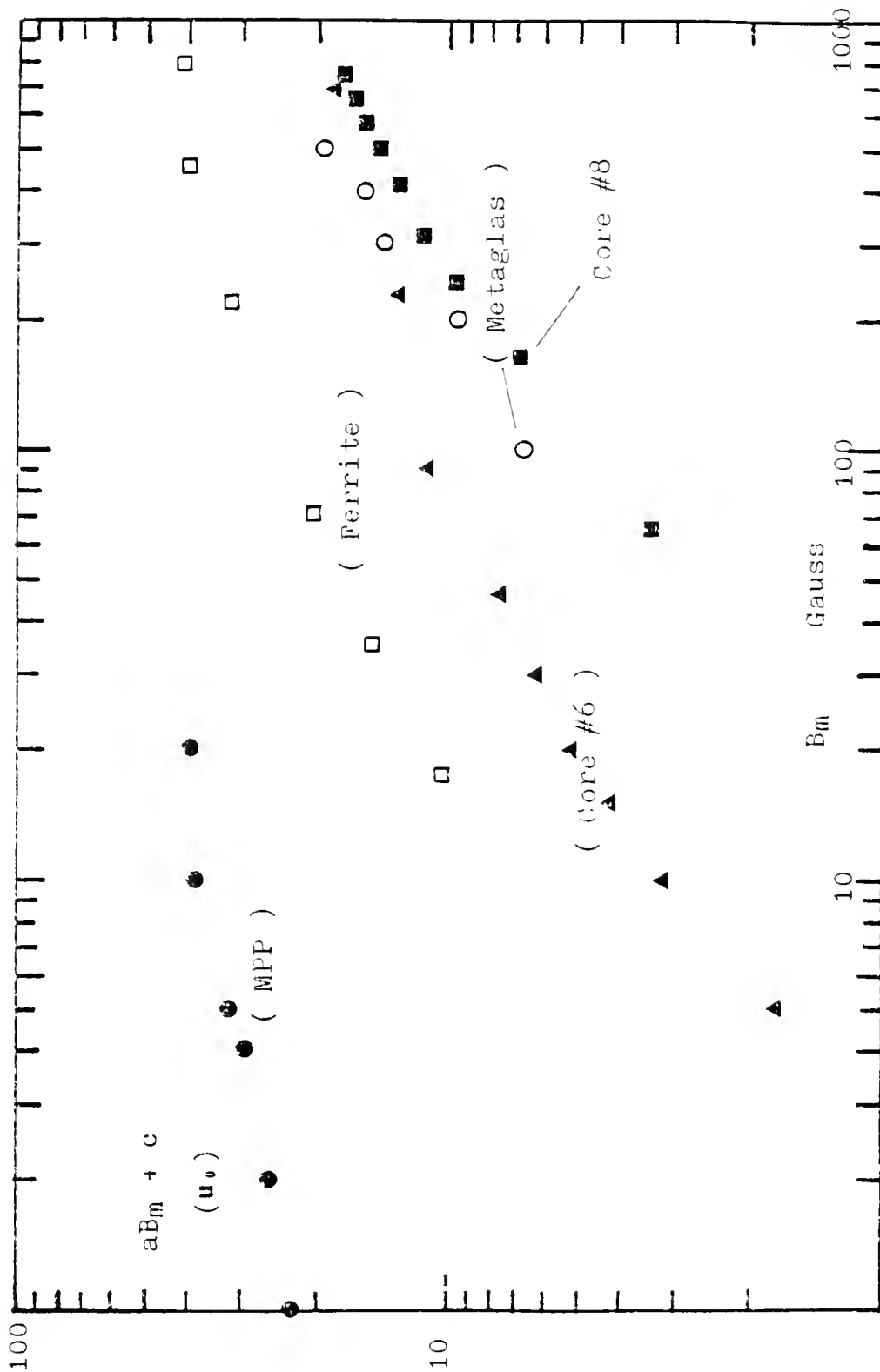
Fig. 2-17 $aB_m + c$ versus B_m for five magnetic materials in log-log scale.

experimantal data. The mathematical model was then manipulated into the form of a somewhat generalized Legg equation which seems applicable to a higher B_m. Frequency variations of inductance due to capacitance or other effects were not considered. The problem of making the model independent of geometry and turns has not yet been studied; so the coefficients listed in Table 2-1 may be specific to these specific inductors.

CHAPTER 3
APPLICATION OF LOSSY INDUCTOR MODEL
TO Q FACTOR AND POWER LOSS OF COIL

This chapter describes how the lossy inductor model derived in chapter 2 can be applied to the modeling of Q factor and of power losses of an inductor.

3.1 Application of Model to Q of Coil

The quality factor Q of an inductor is defined as the ratio of energy stored to energy dissipated per cycle, as shown in Eq.(1-2), repeated here as Eq.(3-1):

$$Q = \frac{\omega L}{R_w + R_{ac}} \qquad (3-1)$$

A representative curve of the Q factor of an inductor may be shown as in Fig. 3-1.

When Eq.(3-1) is rewritten by substituting Eq.(2-5) for (3-1) in the denominator, the result shows that

$$Q = \frac{2\pi f L}{r_0 + r_1 f + r_2 f^2} \qquad (3-2)$$

Assuming the effective L is invariant with frequency, at low frequency end, the $r_2 f^2$ and the $r_1 f$ terms are negligible comparing with r_0, the asymptote for Q at low-frequency is
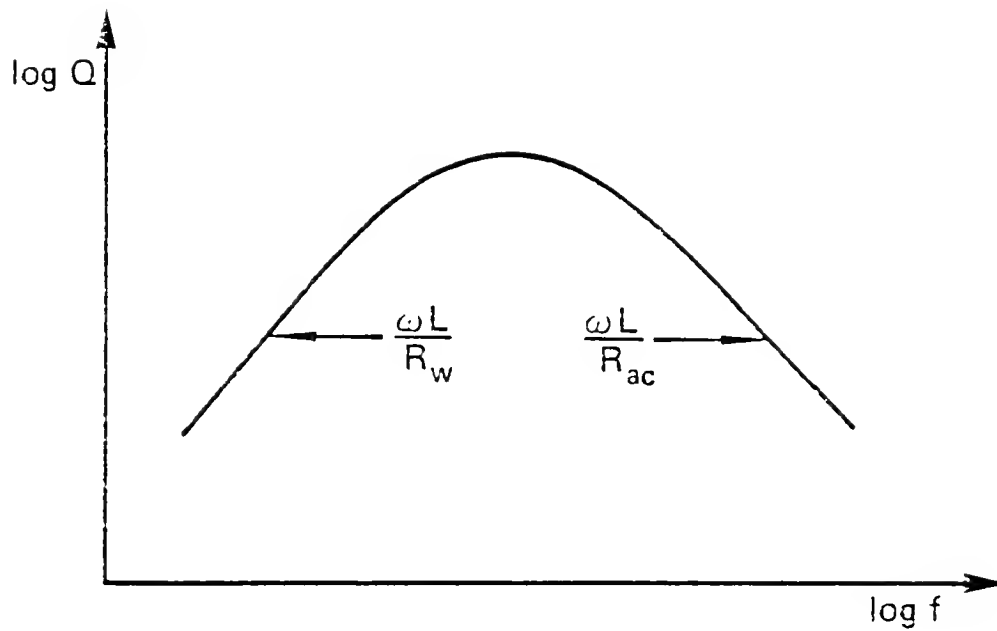
Fig. 3-1   A representative Q-factor for an inductor
plotted against frequency.

$$Q = \frac{2\pi f L}{r_0} \qquad (3-3)$$

Thus, Q increases as f increases.

At the high frequency end, both the terms r_0 and $r_1 f$ are smaller than $r_2 f^2$, thus

$$Q = \frac{2\pi f L}{r_2 f^2} \qquad (3-4)$$

This analysis supports the concave-down trend of Fig. 3-1. The maximum Q occurs at the frequency where $dQ/df = 0$, which is readily shown to satisfy the condition $r_0 = r_2 f^2$, namely

$$f = \sqrt{\frac{r_0}{r_2}} \qquad (3-5)$$

The Q factor at this frequency is

$$Q_{max} = \frac{2\pi L}{2\sqrt{r_0 r_2} + r_1}. \qquad (3-6)$$

A more general form of Eqs. (3-5) and (3-6) may be obtained by allowing variations of B_m according to Eqs. (2-3), (2-5) and (2-6). The results are

$$f = \sqrt{\frac{r_0}{(r_{20} + r_{21} B_m)}} \qquad (3-7)$$

The maximum Q of the inductor is then

$$Q_{max} = \frac{2\pi f L_0 (1 + b B_m)}{2\sqrt{r_0 (r_{20} + r_{21} B_m)} + (r_{10} + r_{11} B_m)} \qquad (3-8)$$

The frequencies at which Q has half value of Q_{max} are the frequencies that satisfy the following equation:

$$\frac{1}{2}(r_0+r_1 f+r_2 f^2) = 2\sqrt{r_2 r_0}+r_1 \qquad (3-9)$$

which are shown to be

$$f = \frac{-r_1 \pm \sqrt{r_1^2 - 4r_2(r_0 - 4\sqrt{r_2 r_0} - 2r_1)}}{2r_2} \qquad (3-10)$$

The "bandwidth" (the width of the Q curve with $Q > 1/2\ Q_{max}$) of the Q figure is then

$$\triangle f = \frac{\sqrt{r_1^2 - 4r_2(r_0 - 4\sqrt{r_2 r_0} - 2r_1)}}{r_2} \qquad (3-11)$$

This equation shows that the larger the r_2, the narrower the "bandwidth."

Figure 3-2 shows values of Q of Metglas core measured as a function of frequency, and calculated points for Q_{max}, using Eq.(3-8). The solid lines represent the calculated value of Q using Eq.(3-2). The good agreement between the measured Q and the calculated Q supports the consistency of the model and of the data analysis.

3.2   Power Dissipation Using the Model

We described in chapter 2 that a lossy inductor can be represented as a pure inductor in series with a resistance(series model). This model, however, can be
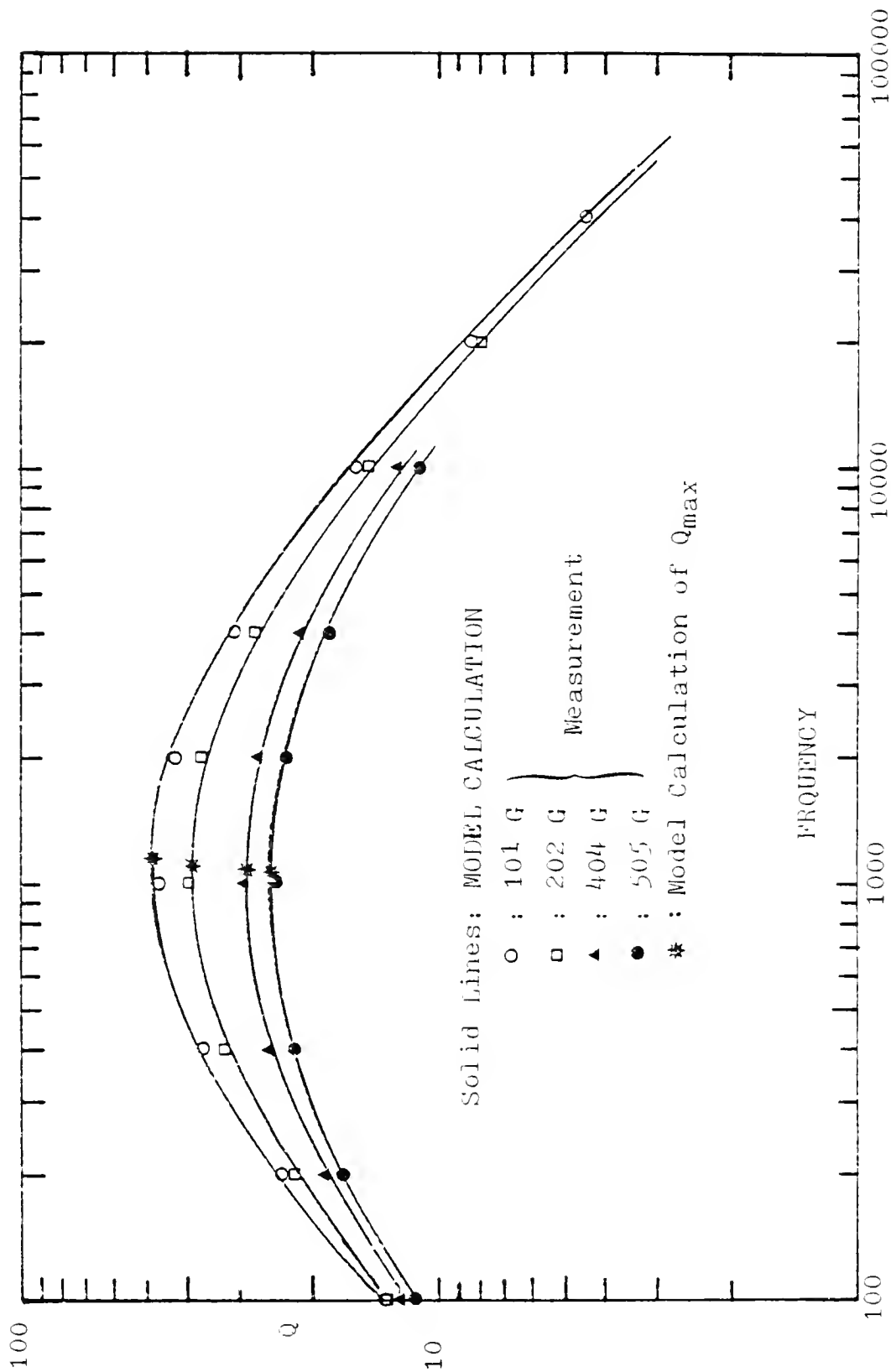
Fig. 3-2 Measured Q vs frequency for inductor on Metglas core at various B_m.

transformed into a parallel model which is an inductor L_p in parallel with a resistance R_p, as shown in Fig. 3-3. The relation between this two models is

$$R_p = R_s(1+Q^2) \qquad (3-12)$$

$$L_p = L_s(1+\frac{1}{Q^2}) \qquad (3-13)$$

with the Q value

$$Q = \frac{\omega L_s}{R_s} = \frac{R_p}{\omega L_p} \qquad (3-14)$$

For the series model, the power losses of the inductor is

$$P = I_{rms}^2 R_s \qquad (3-15)$$

where I is the rms value of current flow in the inductor. For the parallel model,

$$P = \frac{V_{rms}^2}{R_p} \qquad (3-16)$$

where V_{rms} is the voltage (rms value) across the inductor. Since $R_p = R_s(1+Q^2)$, and for a sinusoidal voltage, B_m relates to V_{rms} according to Eq.(1-5), thus

$$P = \frac{(4.44)^2}{10^{16}} \times \frac{A^2 N^2 B_m^2}{R_s(1+Q^2)} \qquad (3-17)$$

For a high Q inductor, $Q \gg 1$, thus
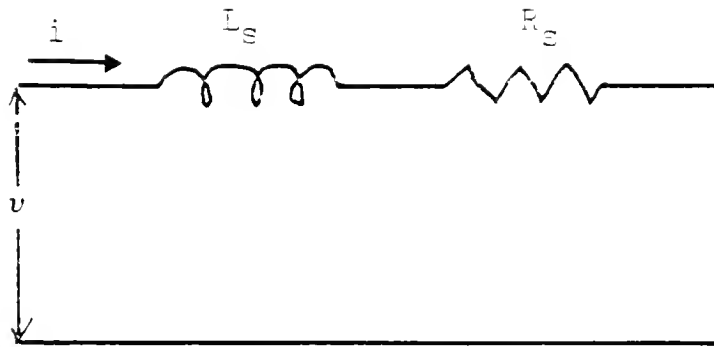
(a)

(b)

Fig. 3-3 Inductor Models (a) series model
                          (b) Parallel model.

$$P = 1.97 \times 10^{-15}\frac{f^2 B_m^2 R_s A^2 N^2}{(\omega L)^2} =$$

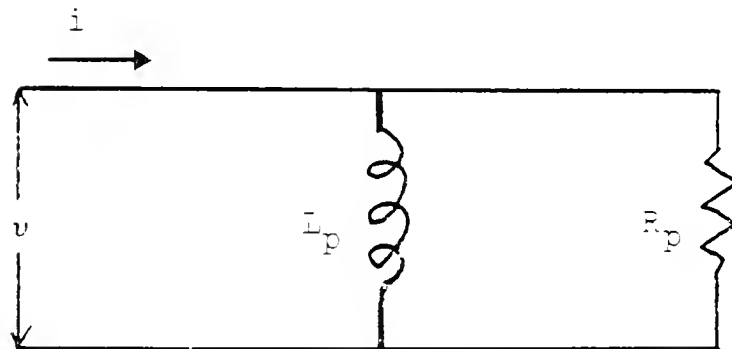$$\frac{1.97\times10^{-15}}{4\pi^2} \times \frac{A^2 N^2 B_m^2 (r_0 + (r_{10} + r_{11} B_m)f + (r_{20} + r_{21} B_m)f^2)}{L_0^2 (1 + b B_m)^2} \quad (3-18)$$

Equation (3-18) shows that power loss is a complicated function of frequency and B_m. This equation, however, can be simplified under some circumstances. For example, if f^2 loss is dominant, Eq.(3-17) in logarithmic form becomes

$$\log P = c_0 + \log\frac{B_m^2}{(r_{20} + r_{21} B_m)} - 2\log Q. \quad (3-19)$$

where c_0 is a lumped constant that includes geometry A and number of turns N. In the following equations, all the contants c_i's are lumped constant.

Equation (3-19) shows that at a specified B_m, $\log P = c_1 - 2 \log Q$. For a typical inductor where Q is a monotonically decreasing function of frequency at high frequency end, as shown in Fig. 3-1, the functional dependence of Q on f may be written as

$$\log Q = c_2 - d_1 \log f \quad (3-20)$$

thus,

$$\log P = c_3 + 2d_1 \log f, \quad P = c_4 f^{2d_1} = c_4 f^d \quad (3-21)$$

On the other hand, if f loss term is dominant, Q is nearly a constant, then at a specified B_m,

$$\log P = c_5 + \log f, \qquad (3-22)$$

which is a typical result of hysteresis loss. Similarly, at a specified frequency, Eq. (3-18) can be simplified as

$$P = \frac{1.97 \times 10^{-15}}{L_0^2} \times \frac{B_m^2 (R_0 + R_1 B_m)}{(1+bB_m)^2} \qquad (3-23)$$

where R_0 is the sum of $r_0, r_{10}f$ and $r_{20}f^2$, and R_1 is the sum of $r_{11}f$ and $r_{21}B_m$. Thus,

$$\log P = c_6 + 2\log B_m + 2\log(R_0 + R_1 B_m) - 2\log(1+bB_m) \qquad (3-24)$$

In certain B_m range, and if the last term is neglected, the superposition of the second and the third terms in log P-log B_m plot shows that P may take the form

$$P = c_7 B_m^{\beta} \qquad (3-25)$$

with $\beta \geq 2$.

In summary, the analysis with our model shows that power loss of an inductor depends on the frequency and B_m in such a way that power loss is proportional to the αth order of f and βth order of B_m. The value of α depends on the relative magnitude of the three components of loss. If f loss is dominant, α is close to 1, if f^2 loss dominate, α is close to 2. The value of β value depends on the range of B_m of the inductor in application, it is not a constant.

3.3   Measurements and Calculations

The ferrite core, the Metglas core, and the MPP core are selected to verify our analysis.

Measurements of L_s , ESR and Q in series mode and L_p, R_p in parallel mode were made using HP 4274A LCR meter at various B_m and at various frequencies ranges; data are formulated into Eq.(3-18) to calculate power losses of the inductor; Figure 3-4 shows the results of power loss versus frequency at three B_m values with Metglas as an example; solid lines are those calculated from Eq.(3-18). Figure 3-5 shows the example of P versus B_m at three frequencies for ferrite. Figure 3-6 shows the example of P vs B_m at f=1k for Metglas. Model calculation and experiment result are in very good agreement. For the three materials, in our data range, power losses are fairly well described by Eq.(3-21) and Eq.(3-25), and the parameters ⍺ and β are listed in Table 3-1. Data regions are also indicated for each core in the table.

3.4   Conclusion

Power losses of inductors wound on ferrite, Metglas and MPP core materials have been studied using an equivalent electrical circuit model. Important elements of the circuit like pure inductance and ESR, which were modeled in a mathematical form in chapter 2, were manipulated into the form of Q factor and power loss to describe their general features as a function of B_m and frequency. A mathematical
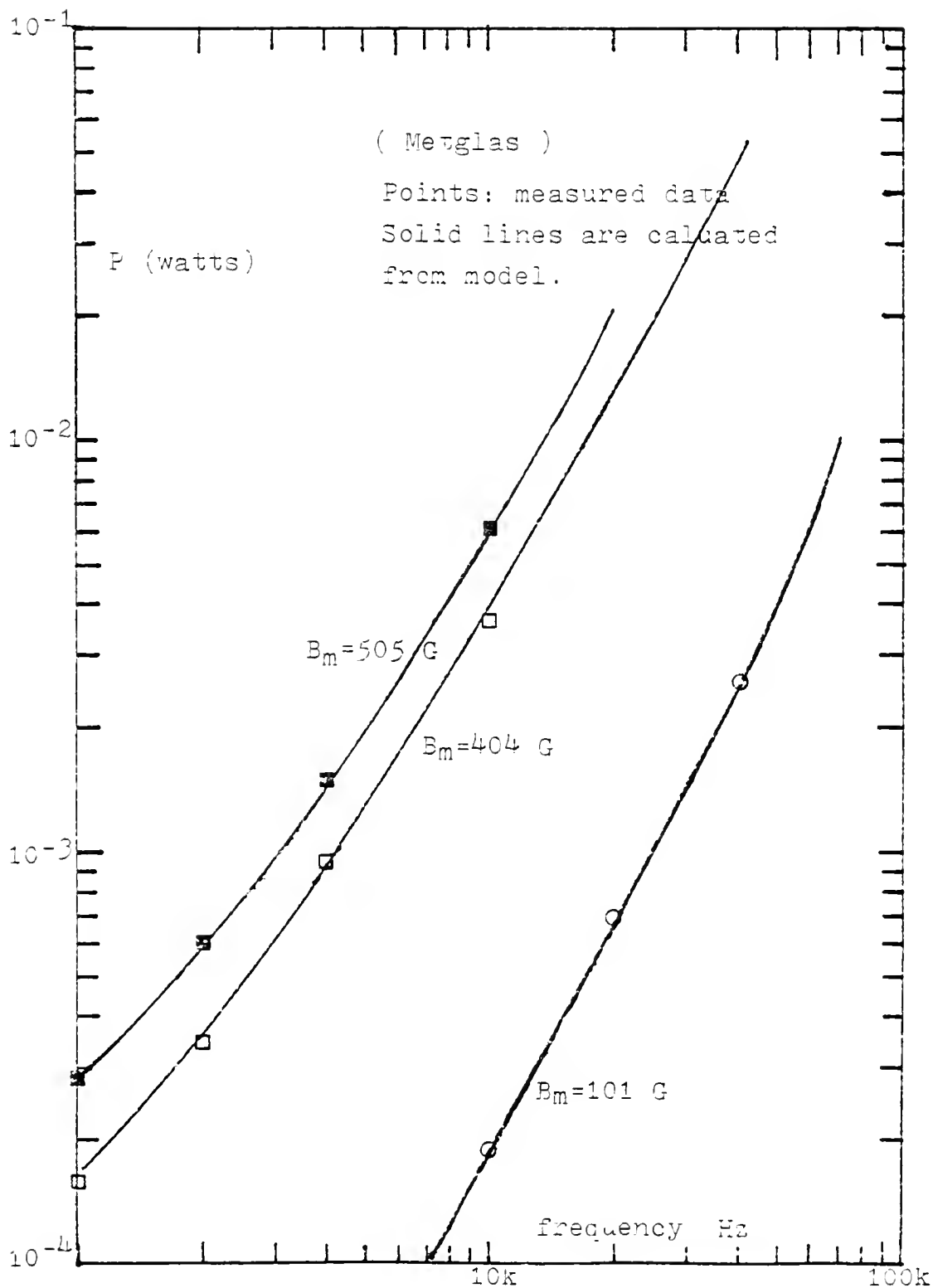
Fig. 3-4   Power loss as a function of frequency at various
B_m. Solid lines are calculated from model. (Metglas)
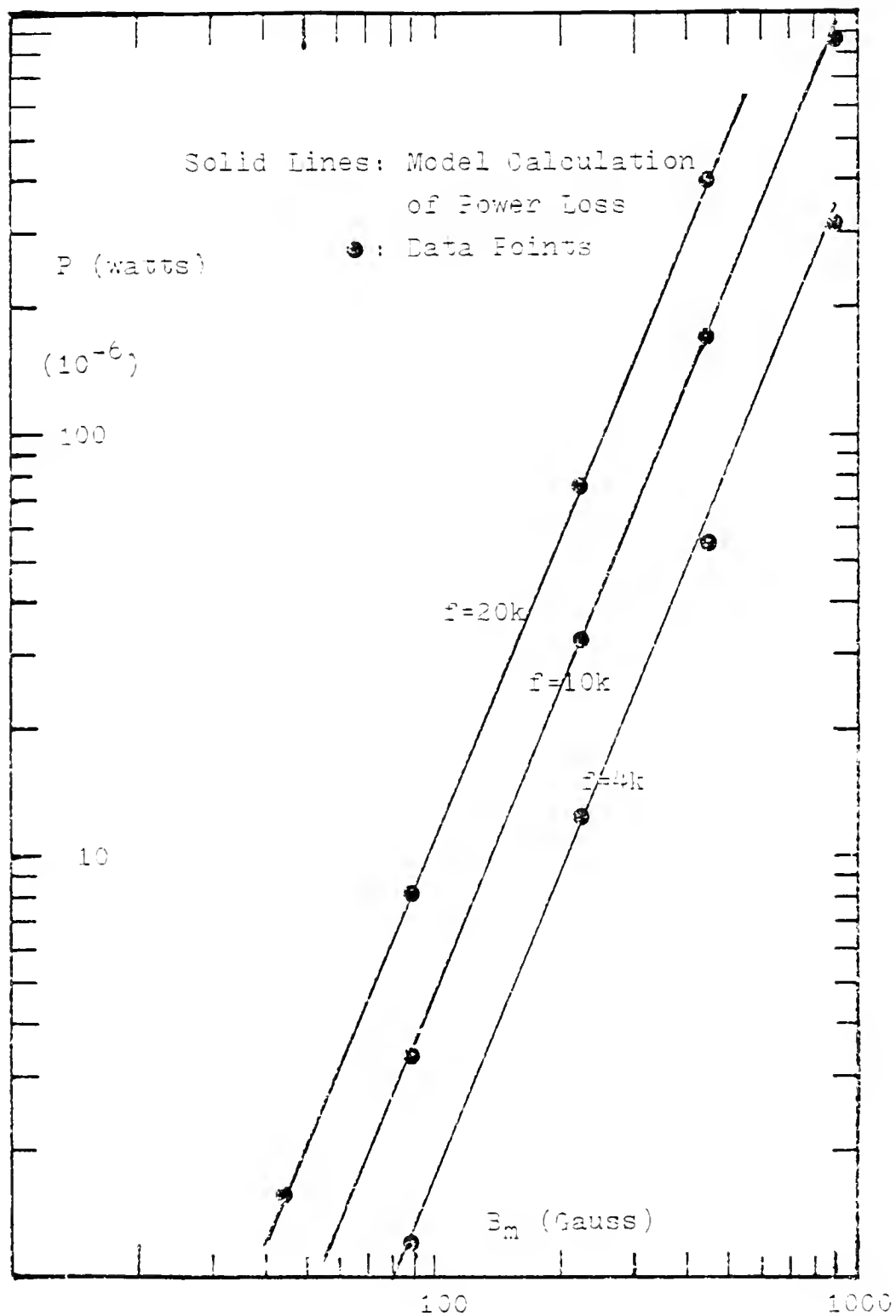
Fig. 3-5 Power loss vs B_m at various frequency. (ferrite)
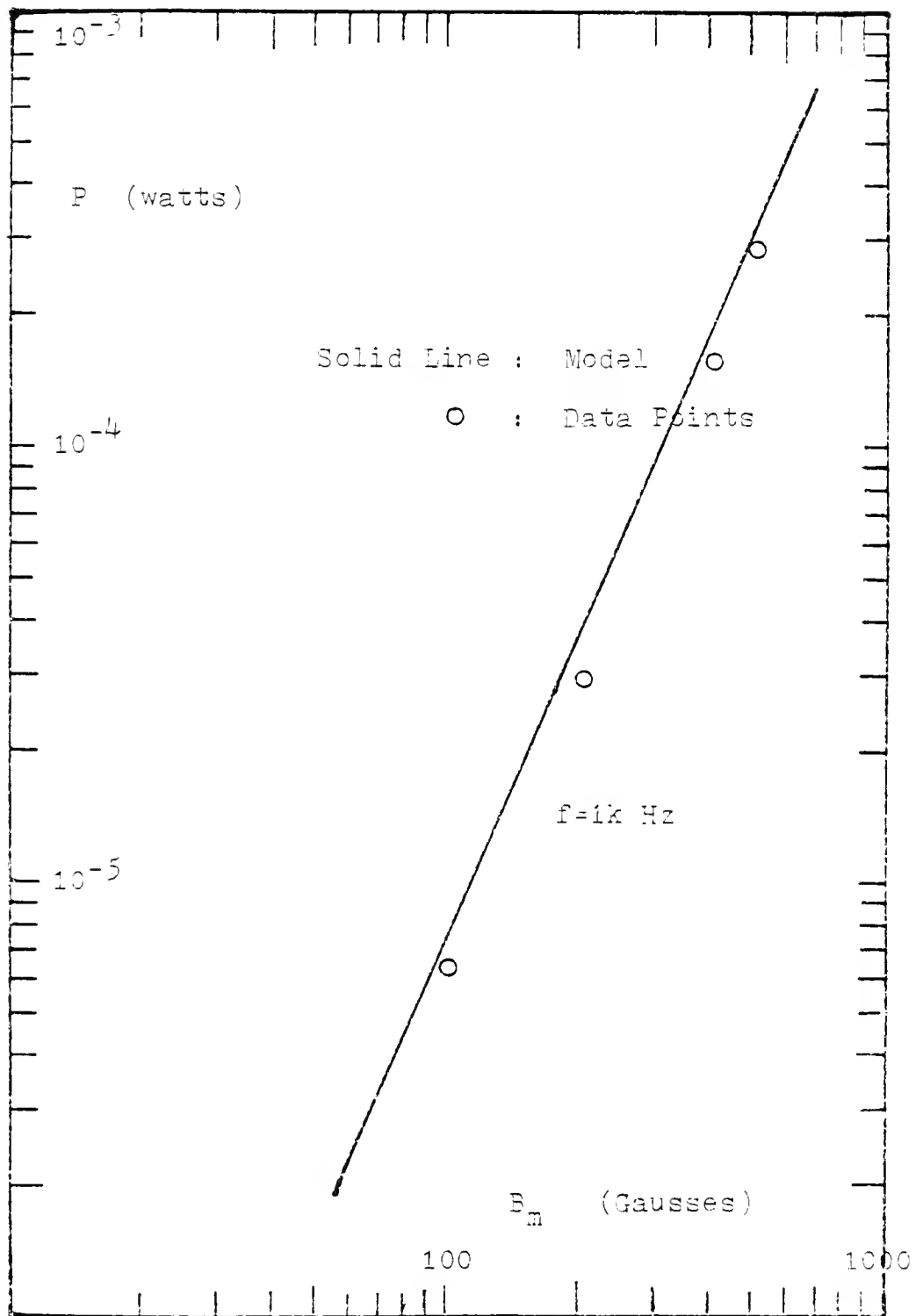
Fig. 3-6 Power loss as a function of B_m at f=1000 Hz. (Metglas)

Table 3-1. Power Loss Parameters of Three Materials.

Material	α	β	Data Region
Ferrite	1.08	2.39	$4k \leq f \leq 40k$, $B_m \leq 500$
Metglas	1.70	2.0	$4k \leq f \leq 40k$, $B_m \leq 600$
MPP	1.79	2.05	$4k \leq f \leq 40k$, $B_m \leq 50$

expression for Q of a coil has been derived. The frequency at which Q has a maximum, and the maximum Q value of the inductor can be calculated from our model. Power loss of an inductor as a function of frequency and B_m are derived; power losses were found to vary with frequency in the form of Eq.(3-21) and with B_m in the form of Eq.(3-25) of our model. Parameters of ᾱ and β of the three cores are listed in Table 3-1.

CHAPTER 4
NORMAL INDUCTANCE MEASUREMENTS

This chapter reports measurements of normal inductance for six inductors wound on the following materials in toroidal form: a ferrite (Ferroxcube, 3E2A), an amorphous alloy (Metglas®, 2605SC with high frequency anneal), a permalloy 4 mil tape wound core (core #6), and three special anneal 1 mil tape wound permalloy cores with different kinds of heat treatments. The data of this chapter are interpreted in chapters 7 and 8.

4.1   Introduction

Normal inductance, often referred to simply as inductance, is measured when the specimen is in the a-c magnetic state.

Normal inductance is related to amplitude permeability, μ_a, by Eq.(1-7), where μ_a is defined by the slope of a line drawn in Fig. 1-1 from the origin to a point defined by the total B/H.

By means of hysteresis loop, one also can define a large number of permeabilities (O166). The initial permeability

$$\mu_i = \lim_{H \to 0} \frac{B}{H} \tag{4-1}$$

This is the permeability at the origin of the curve at the first magnetization. The amplitude permeability

$$\mu_a = \frac{B}{H} \qquad (4-2)$$

This is the permeability for a stated value of the field strength (or induction) when the field strength varies periodically with time.

Many amplitude permeabilities are defined due to the fact that B-H relation of a magnetic material is nonlinear during the a-c cycle (i.e., hysteresis effect). Thus when deal with permeability, one must state which curve form for the independent variable is chosen (e.g.if H is sinusoidal then B is not sinusoidal). Furthermore, we can select the relevant B and H or the separate B_m and H_m, e.g. $\mu_{ap} = (B_m/H_m)$ is the peak-to peak amplitude permeability often named normal permeability when it is derived from the magnetization curve.

The definitions of each of the different amplitude permeabilities can be seen from the book by Olsen [O166]. It should noted that at a specified signal level (B_m or H_m), and when the signal level is low, the differencies among the various amplitude permeabilities can be ignored.

The inductance of an inductor wound on magnetic core is found to depend on the level of testing signal, and is of interest here.

The detailed physical and chemical properties of the ferrite and Metglas cores and core #6 have been described in chapter 1. The properties of the three special anneal, 1 mil

tape-wound permalloy cores (core #1, core#8 and core #14) are described as follows: all the materials were HYMU 80. Core #14 was annealed to maximize the initial permeability by adjusting the order/disorder in the alloy so that anisotropy constant k_1 = 0. Core #1 was heat treated to provide more disorder and more vacancies in the crystal structure. Core #8 was heat treated in an axial magnetic field to introduce a uniaxial anisotropy in the axial direction, perpendicular to the direction of magnetization, in order to reduce remanent magnetization for inductor applications. All the cores are toroidal with mean path length of 8.98 cm. The effective cross section area for each core is based on its core weight.

The dimensions of all the above mentioned six cores are listed in Table 4-1.

4.2 Measurements and Results

Measurements of normal inductance and Q factor were made using an HP 4274-A digital LCR meter. Before the measurements, materials were demagnetized by applying an alternating field with an amplitude high enough to cause the inductance to approach saturation, then slowly reducing the amplitude to zero.

The signal level of measurement was adjusted by controlling the current (in rms value) through the coil, and the peak field strength H_m was calculated according to Eq.(1-5).

Table 4-1. Dimensions of Seven Cores Used In This Study.

Material	Ferrite	Metglas®	Core #6	MPP	Core #1	Core #8	Core #14
O. D. (cm)	1.27	5.08	2.85	4.07	3.175	3.175	3.175
I. D. (cm)	0.71	3.81	1.95	2.33	2.54	2.54	2.54
Path Length (cm)	2.95	13.98	7.54	9.84	8.98	8.98	8.98
Core Area (cm^2)	0.128	0.557	0.822	1.072	0.150	0.152	0.135
Core Height (cm)	0.478	1.27	2.03	1.537	0.635	0.635	0.635

Measured normal inductance is plotted against current I_{rms} and H_m as shown in Figs. 4-1 to 4-6, for the six materials. The number of turns of winding on each core is given in the legend.

In each case, the curve rises from a point on the L-axis above the origin (the initial inductance is non-zero) to a maximum (the maximum inductance) and falls off rapidly and then more slowly as I_{rms} increases.

When the curves of L versus H_m are examined carefully, many interesting features may be observed: The figures suggest that there are three regions of operation: a low field region in which L increases linearly with H_m with slope a_1 (except at very low fields), (a_1 is defined as $(1/L_0)dL/dH$, L_0 is initial inductance), a medium H_m region where L increases linearly with another slope a_2 (defined as $(1/L_2)dL/dH$, where L_2 is the intercept at H=0 of second linear regression line), and a high field region where L decreases from its maximun value at H_{mm}. Thus, in the first region

$$L = L_0(1+a_1H_m) \qquad (4-3)$$

and in the second region

$$L = L_2(1+a_2H_m) \qquad (4-4)$$

At the end of second region and before the high field region, the inductance increases at a slower rate and then reaches a maximum. Different materials have different values of a_1 and a_2. The separation point of first and
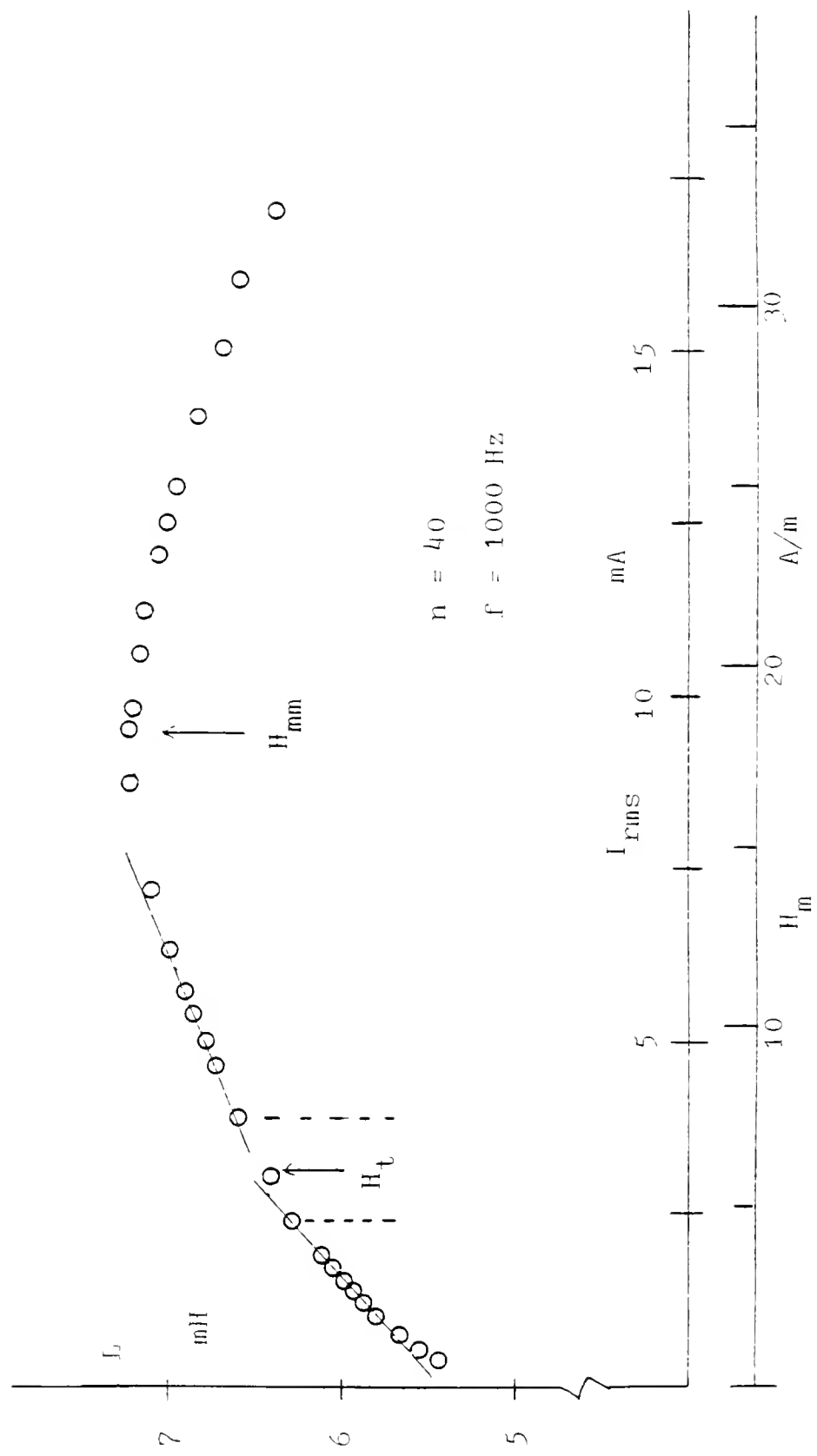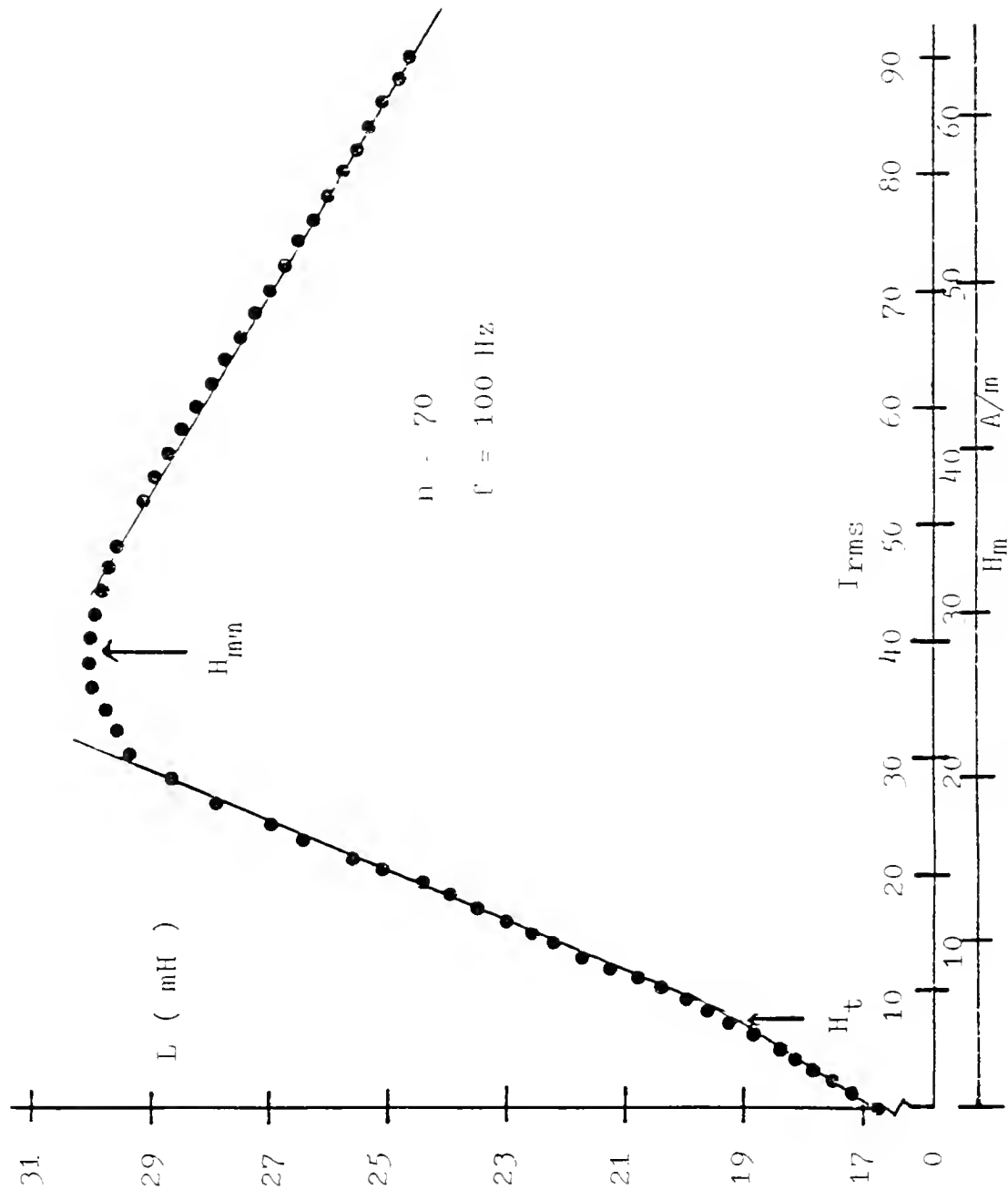
Fig. 4-1 Normal inductance of ferrite.
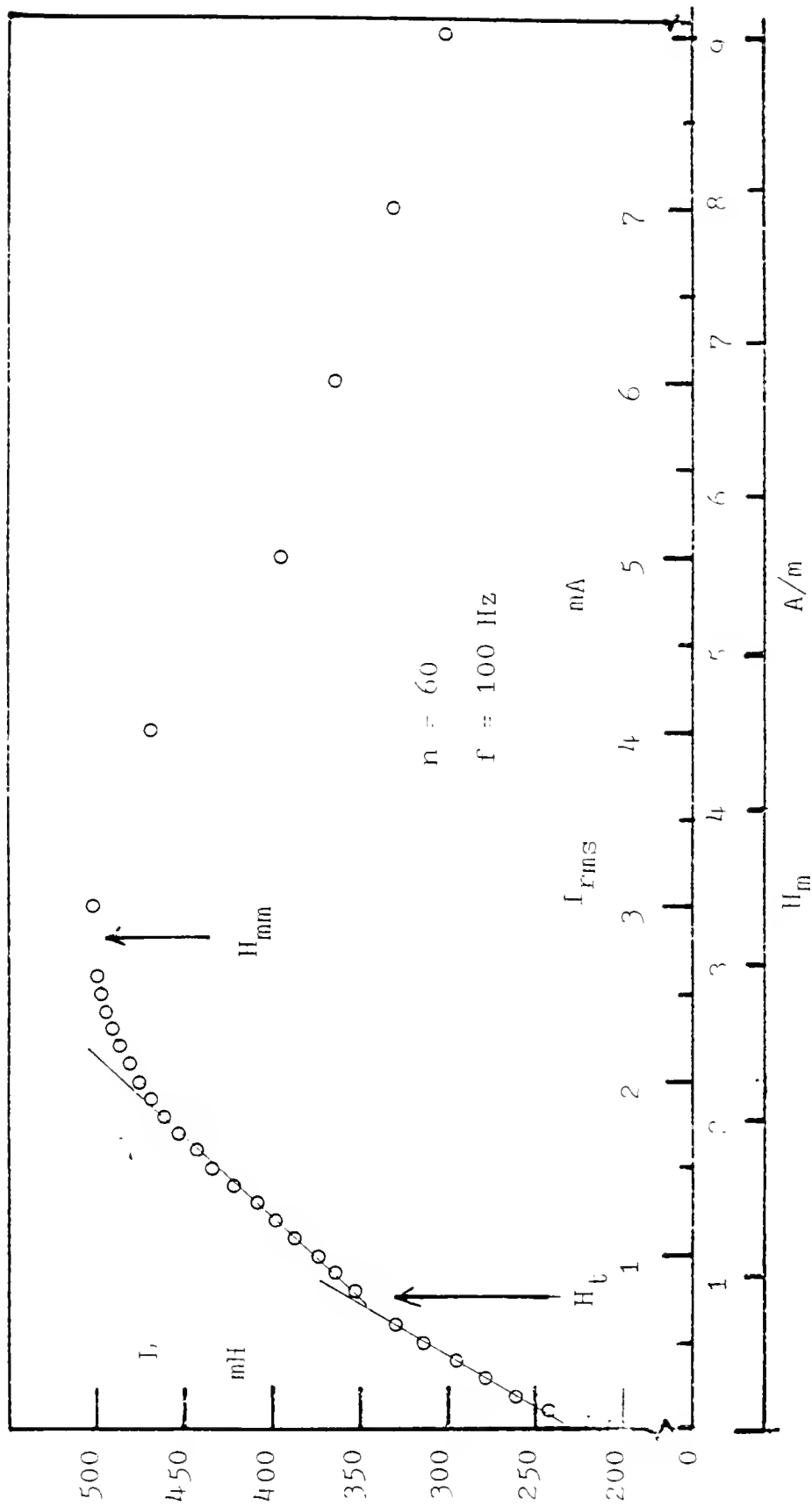
Fig. 4-2 Normal inductance of Metglas.

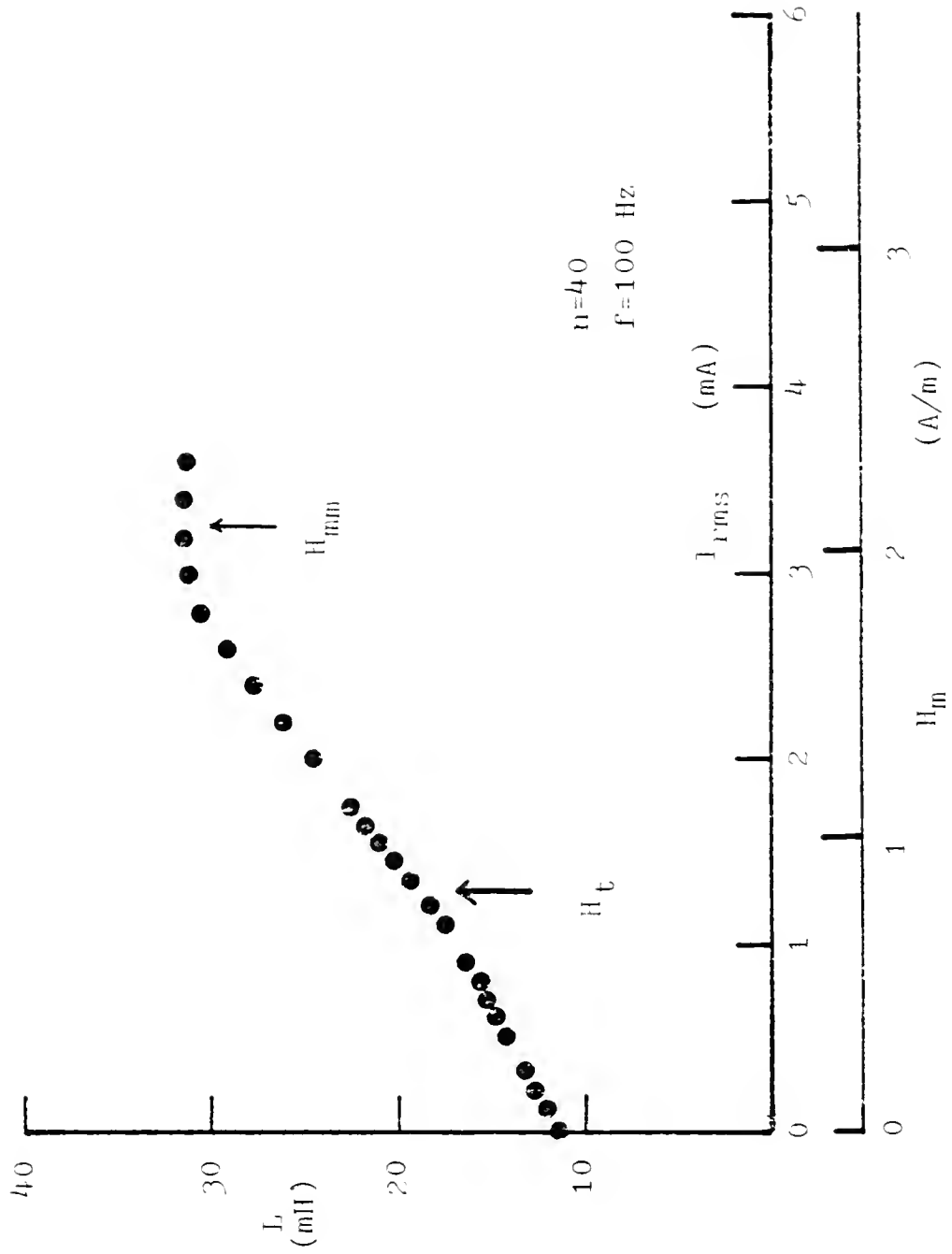Fig. 4-3 Normal inductance of core #6.
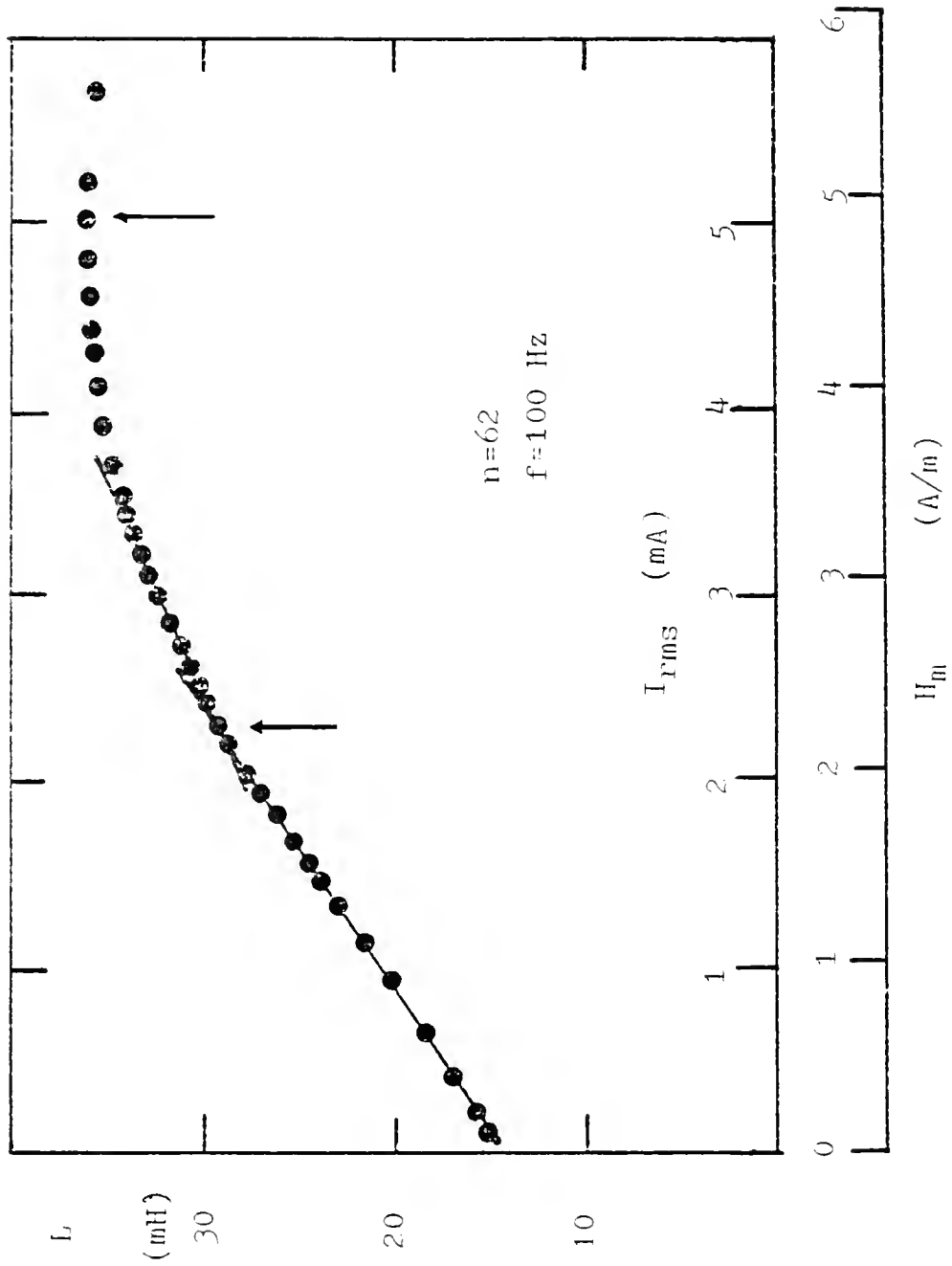
Fig. 4-4 Normal inductance of core #1.

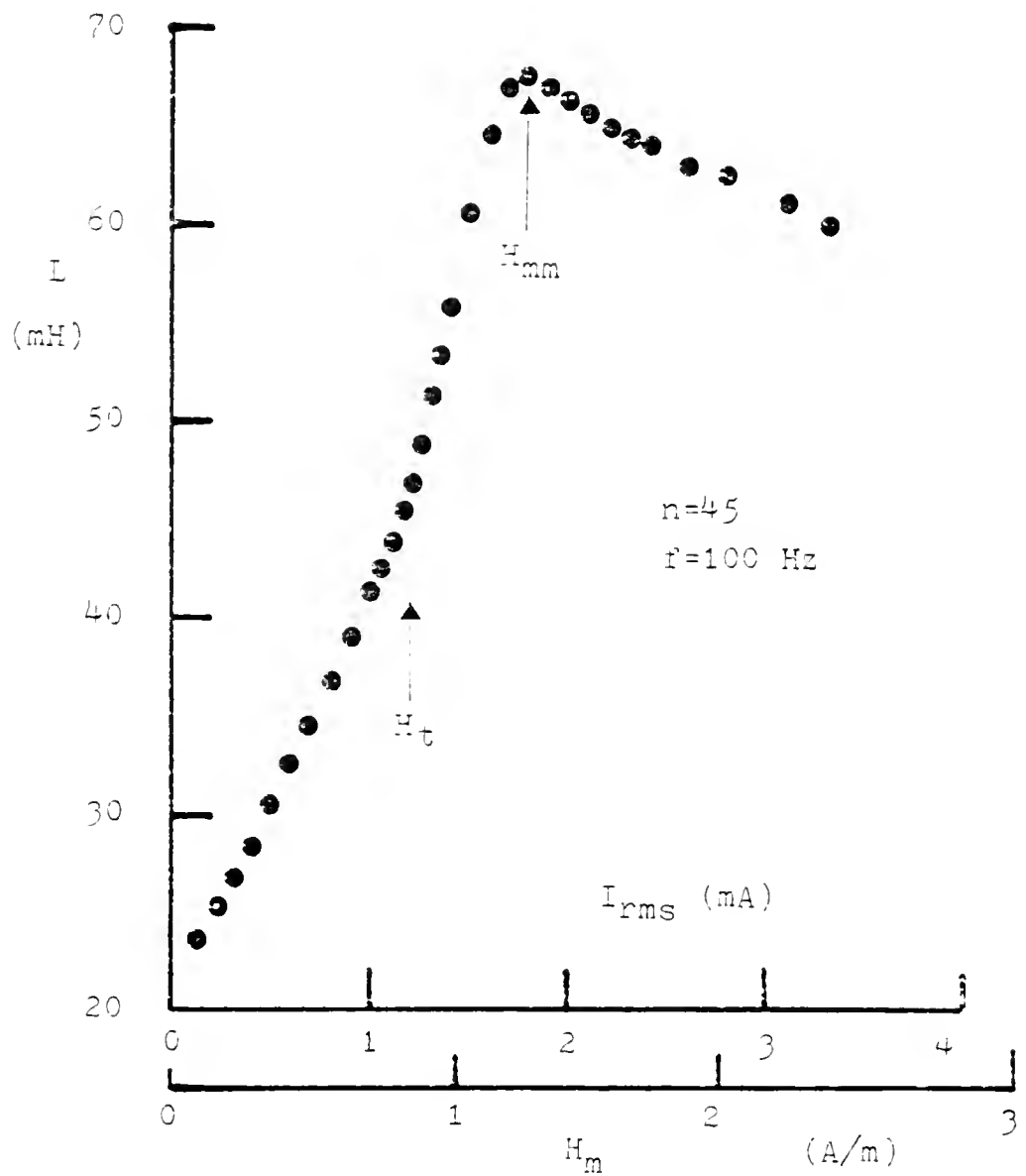Fig. 4-5 Normal inductance of core #8.

Fig. 4-6 Normal inductance of core #14.

second region is indicated as H_t, found from the intersection of the two linear regression lines.

The measured Q factor at f= 1 kHz is plotted as log(Q) versus H_m scale for the ferrite and Metglas in Fig. 4-7 and Fig. 4-8; the field H_t is indicated in these figures. It is interesting to note that the slope of Log(Q) as a function of H_m changes around H_t.

It is worthwhile to mention that the normal inductance measurements of the three 1 mil tape wound cores with different kinds of heat treatment have different features: as shown in Figs. 4-4, 4-5, and 4-6. Each core shows two region of linearly increasing permeability as a function of field strength. For core #1, a_1 is smaller than a_2, the critical field H_t is 0.88 A/m. For core #8 with special anneal, a_1 is larger than a_2, the critical fields H_t is 2.2 A/m. For core #14, a_1 is smaller than a_2, and the critical fields H_t is 0.78 A/m. Core #1 has the highest initial permeability, and core #8 has the lowest initial permeability of the three. The values can be found from Table 4-2.

4.3 Summary

This chapter investigated the normal inductance of inductors wound on toroidal cores of six different magnetic marerials: a ferrite, an amorphous alloy, a permalloy 4 mil tape wound core, and three permalloy 1 mil tape wound cores with different heat treatments.
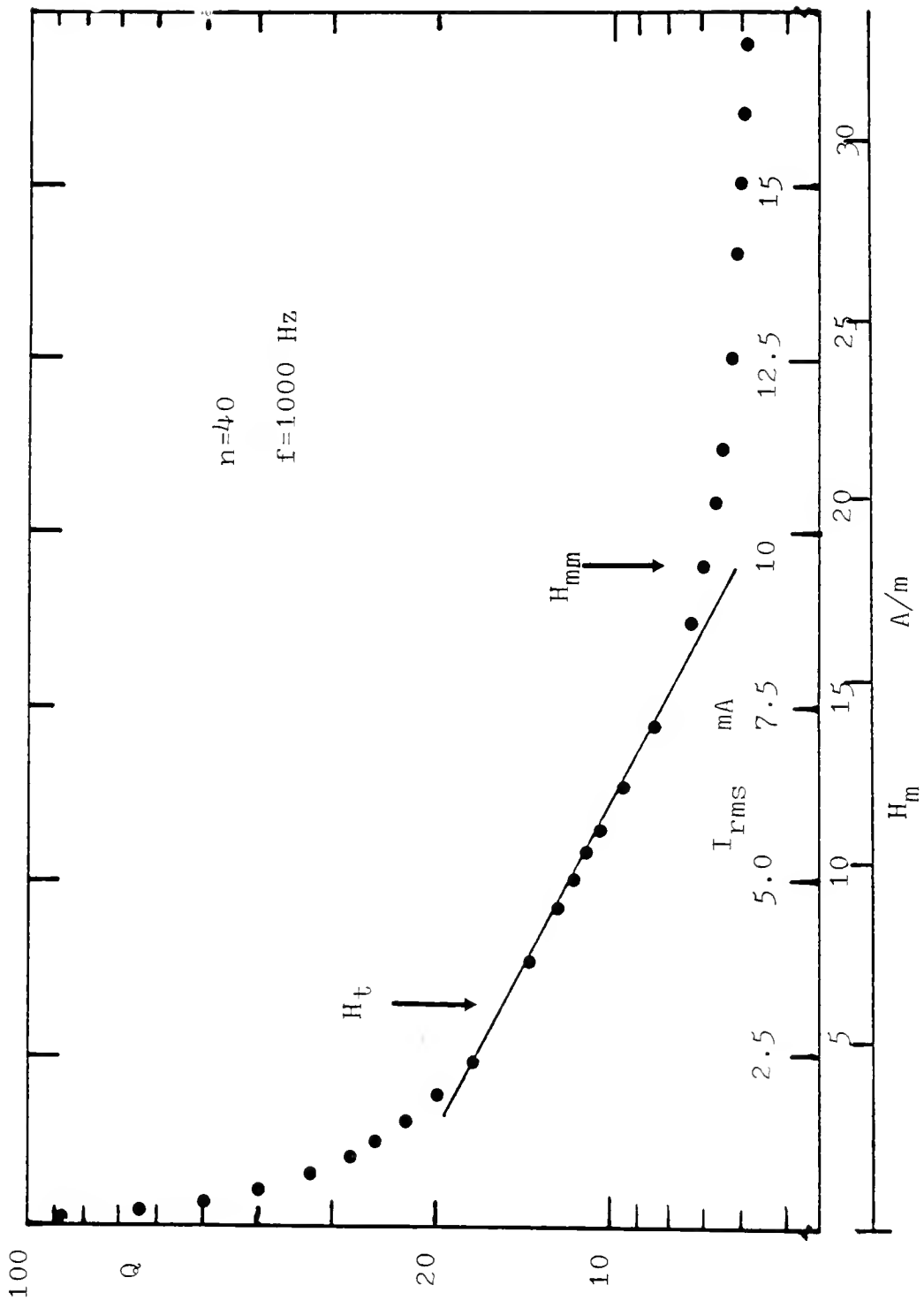
Fig. 4--7 Quality factor of ferrite core as a function of peak field strength.
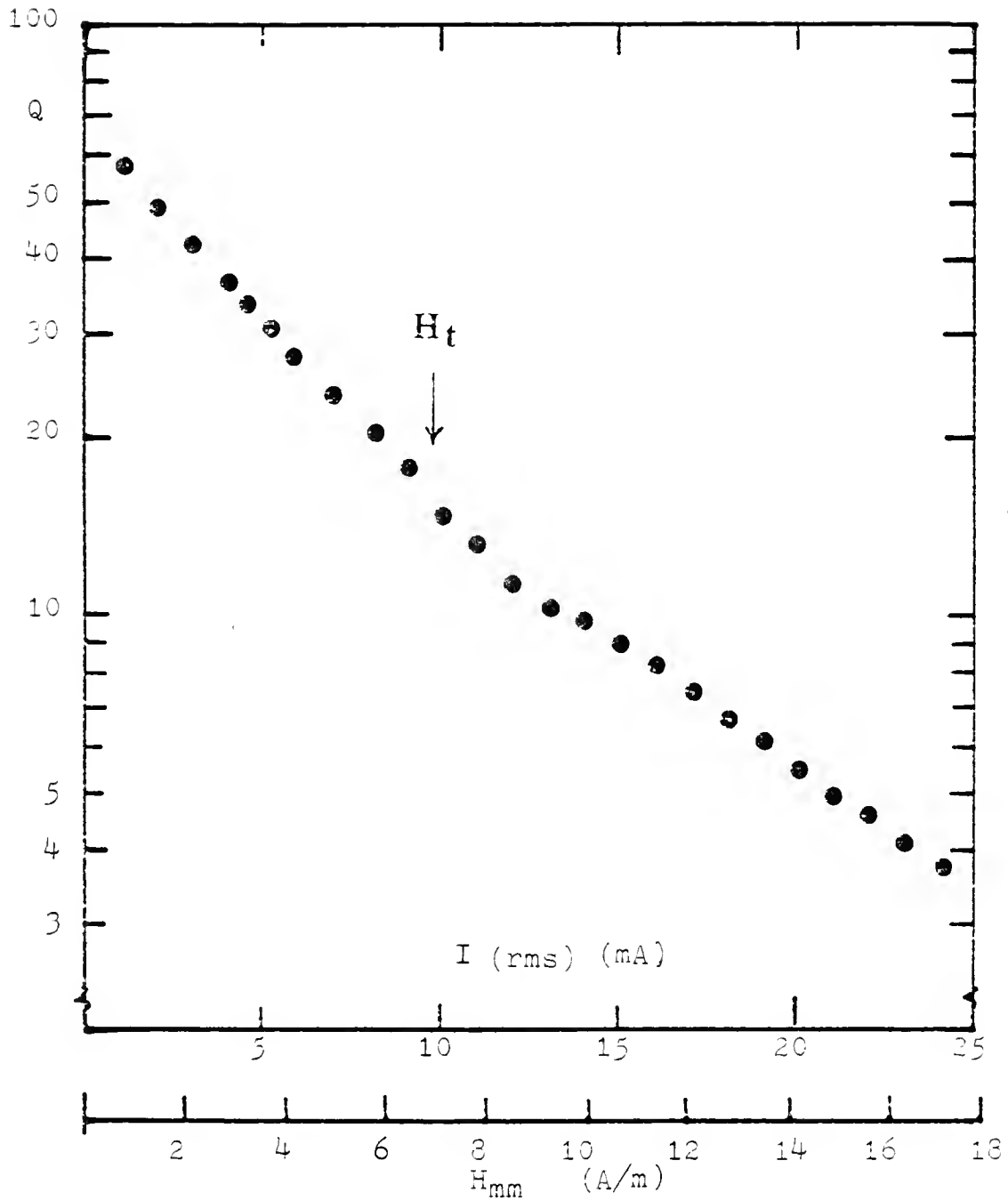
Fig. 4-8 Q factor as a function of H_m of Metglas at
f = 1000 Hz.

Table 4-2 Parameters of six Core Materials.

Parameter	Core Material					
	Ferrite	Metglas	Core #6	Core #1	Core #8	Core#14
a_1 $(A/m)^{-1}$	3.44×10^{-2}	2.3×10^{-2}	7.84×10^{-1}	7.64×10^{-1}	2.76×10^{-1}	1.31
a_2 $(A/m)^{-1}$	1.43×10^{-2}	6.52×10^{-2}	3.94×10^{-1}	1.29	1.36×10^{-1}	–
H_t (A/m)	6.04	5.3	1.07	0.88	2.1	0.78
H_{mm} (A/m)	18.2	26.9	3.15	2.2	4.9	1.28
μ_i (μ_0)	5.90×10^3	6.52×10^3	4.36×10^4	3.42×10^4	2.98×10^4	6.14×10^4
μ_m (μ_0)	8.25×10^3	1.24×10^4	1.05×10^5	9.83×10^4	5.6×10^4	1.76×10^5

Measurements of normal inductance, L, as a function of peak field strength, H_m, show two regions of nonlinearity with different slopes, a_1 and a_2, in which permeability increases as the field strength H_m increases. For ferrite and core #6, a_1 is greater than a_2, while for Metglas, a_2 is greater than a_1. For magnetically annealled core #8, the value a_1 is greater than a_2, opposite is found for core #1 and core #14 without magnetic annealing.

The important parameters of normal inductance measurements made on the six cores are listed in Table 4-2 for each. These include initial permeability, μ_i, maximum permeability, μ_m, the field H_t where permeability change its slope of increasing with field strength, slopes a_1 and a_2, and the field H_{mm} where permeability has its maximum value, μ_m.

The similar trends of normal inductance, observed for cores of such varying physical and chemical properties, raises the question whether these properties may be general for inductive materials without airgaps.

The results of normal inductance are compared with the results of incremental inductance in chapter 7, and a plausible physical interpretation is given in chapter 8.

CHAPTER 5
INCREMENTAL INDUCTANCE MEASUREMENTS

This chapter gives results of measurements of incremental inductance of the same six inductors as selected in chapter 4. Analysis of these data is in chapters seven and nine.

5.1 Incremental Inductance Measurement

Incremental inductance is understood to mean the inductance when a d-c bias current acting on a specimen is maintained constant and an additional a-c current is alternated cyclically between two limiting values. Correspondingly, the incremental permeability is obtained when we deal with a combination of a static and an alternating field

$$\mu_{inc} = \frac{\triangle B}{\triangle H} \, . \qquad (5-1)$$

In general, the amplitude of field excursions is without restriction. When the a-c signal is small, the measured inductance is referred to as reversible inductance, and the corresponding permeability is reversible permeability, which is is probably applicable to the following results, but this dissertation will use the more general terms incremental inductance and incremental permeability in order to avoid

overuse of the letter r subscript that might be confused with relative permeability.

Measurements have been made of core incremental inductance as a function of direct current applied to a second winding of the core. The direct current was controlled by a transistor constant current circuit, as shown in Fig. 5-1, in order not to affect the inductance measurement at the primary winding. The small a-c excitation level can be adjusted by keeping I_{rms} or V_{rms} at a specified value according to Eq.(1-4) and Eq.(1-5). Results of the incremental inductance, L_{inc}, as a function of d-c bias for the six cores are shown in Figs. 5-2 through 5-7.

For each core, a graph of L_{inc} versus H_{dc} can be divided into three regions of operation: a low field region where the inductance is nearly a constant; a medium field region where L_{inc} decreases with increasing H_{dc}; and a high H_{dc} region, where L_{inc} decreases at a slower rate. The inductance in the first region is referred to as L_I. Transition regions in the figures will be explained in chapter seven.

In the first region, μ_{inc} was found to be identical to the initial permeability, μ_i of the material. In the second region, L_{inc} was found to decrease linearly with slope g as H_{dc} increases, where g is defined as $(1/L_d)dL_{inc}/dH_{dc}$, where L_d is the intercept at $I_{dc}=0$ of the linear regression line, shown only in Fig. 5-2. The value H_d is the critical field that separate the first and the second region. The value of
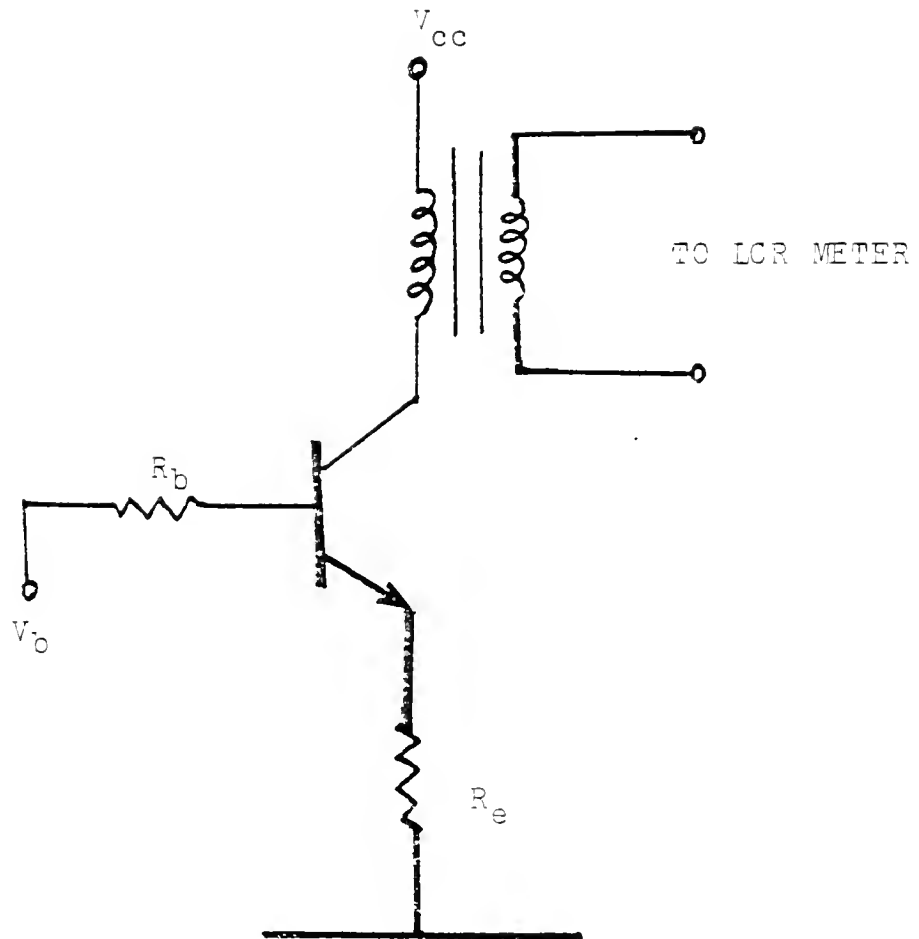
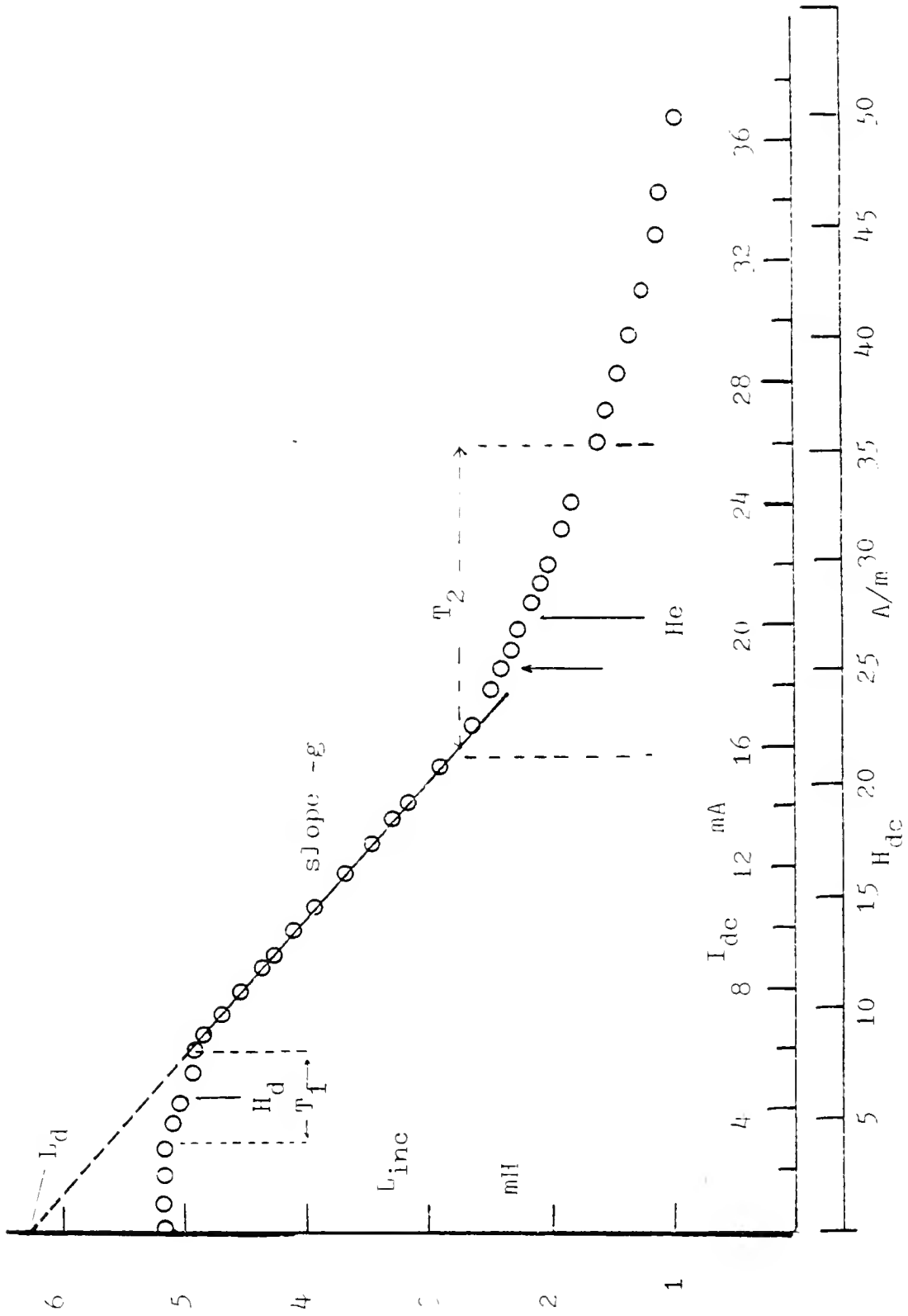Fig. 5-1 Circuit for measurement of incremental inductance.

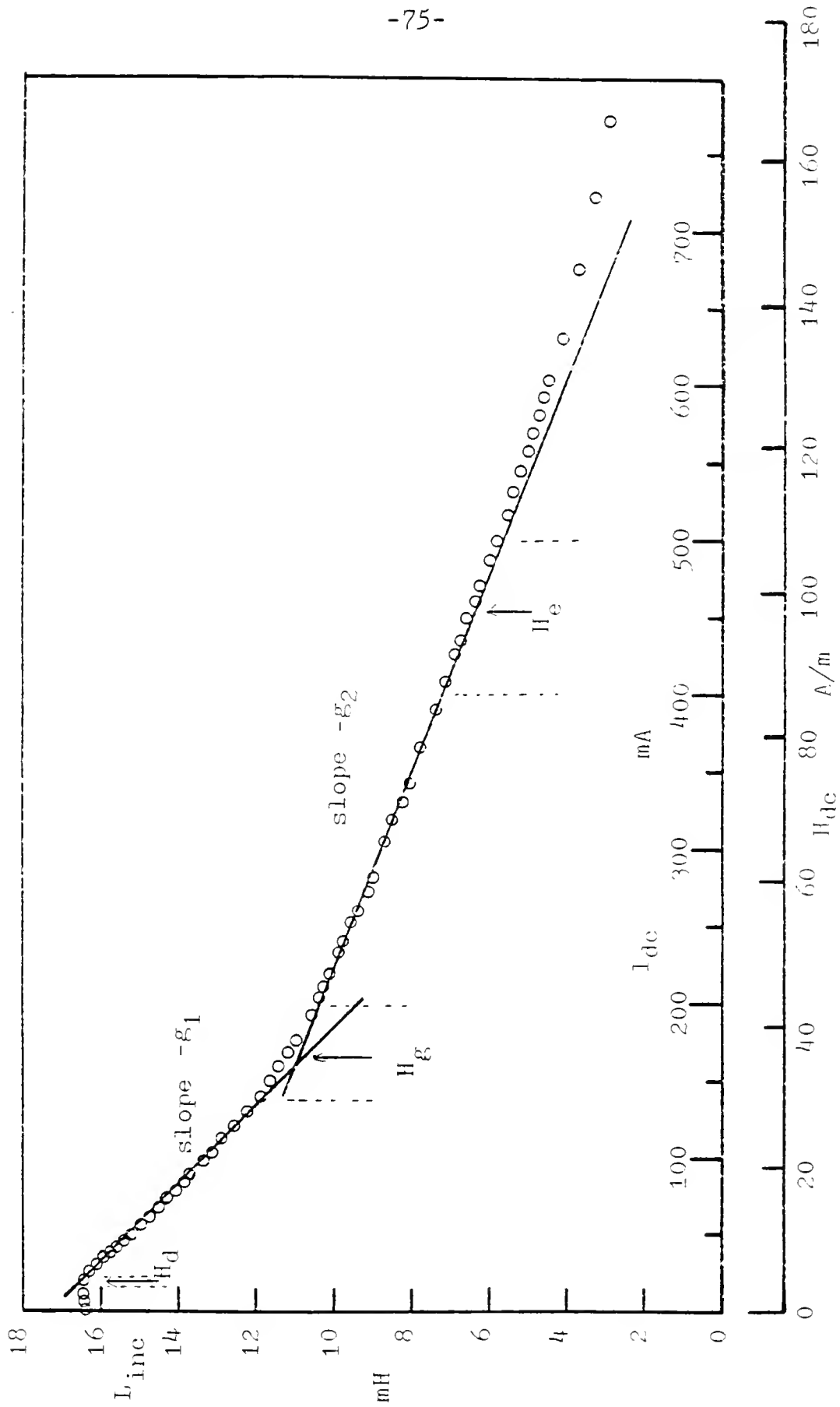Fig. 5-2 Incremental inductance of ferrite. $(n_{ac}=n_{dc}=40)$

Fig. 5-3   Incremental inductance of Metglas.   (n_{ac} = 70, n_{dc} = 30)
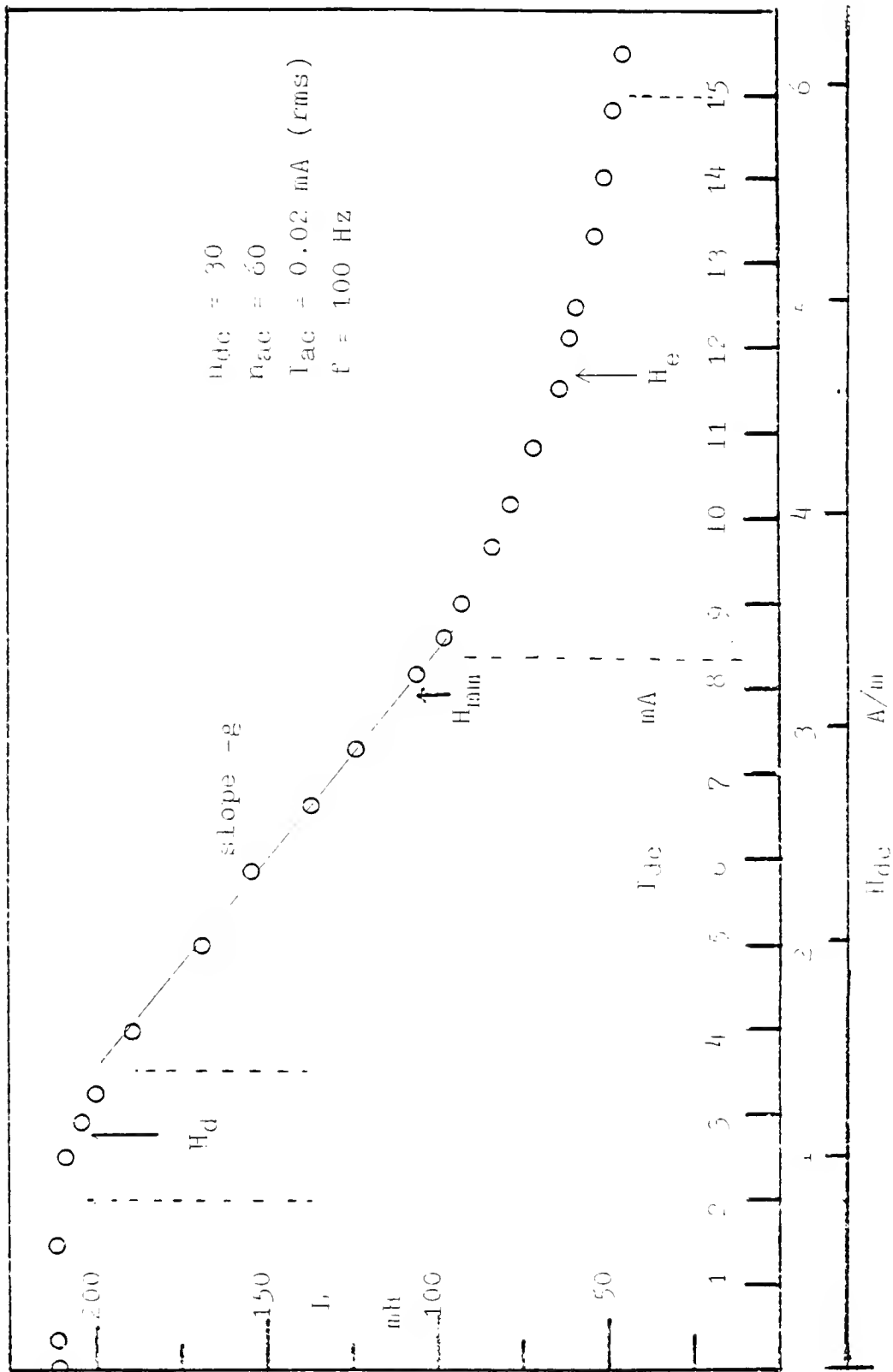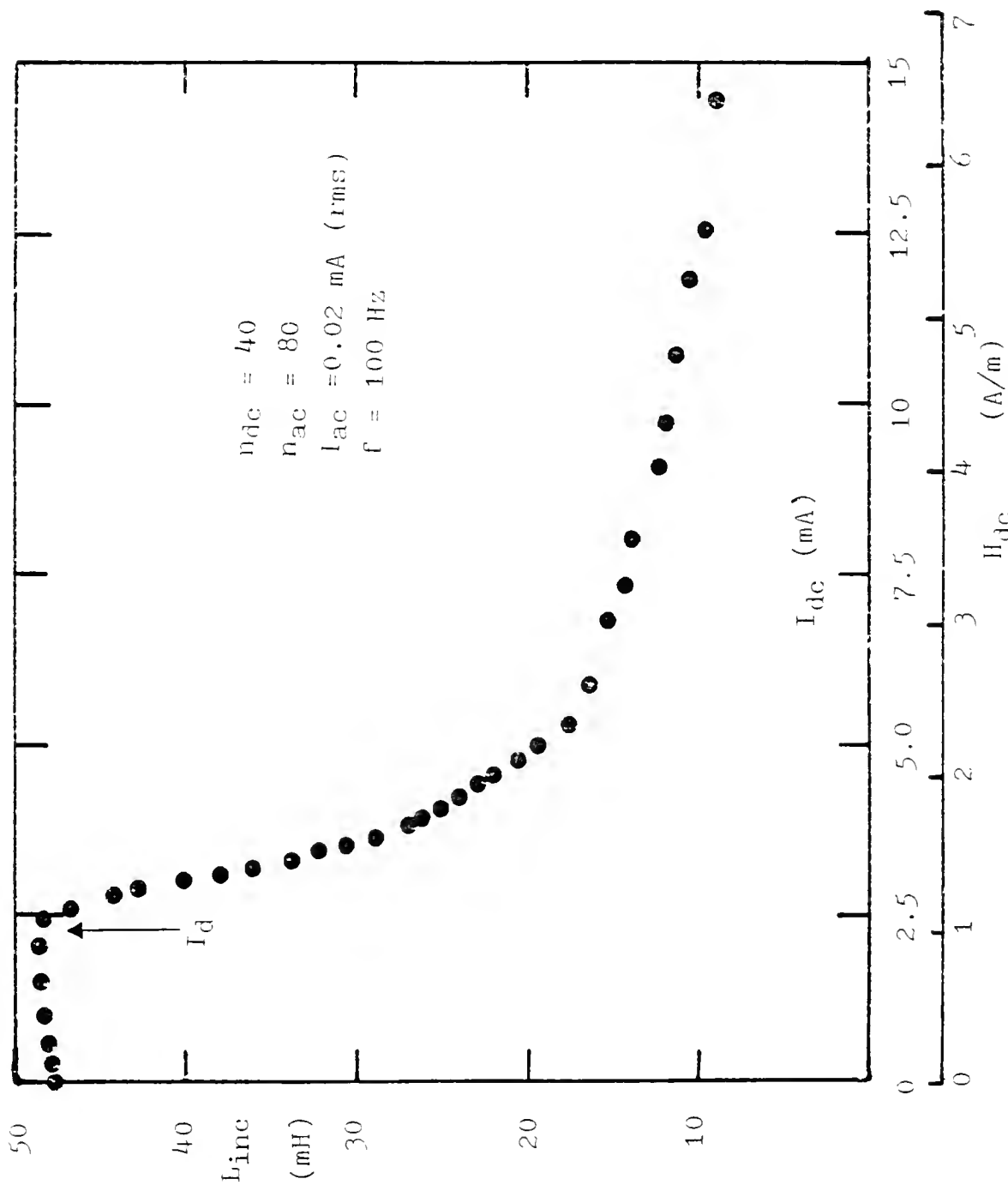
Fig. 5-4 Incremental inductance of core #6.

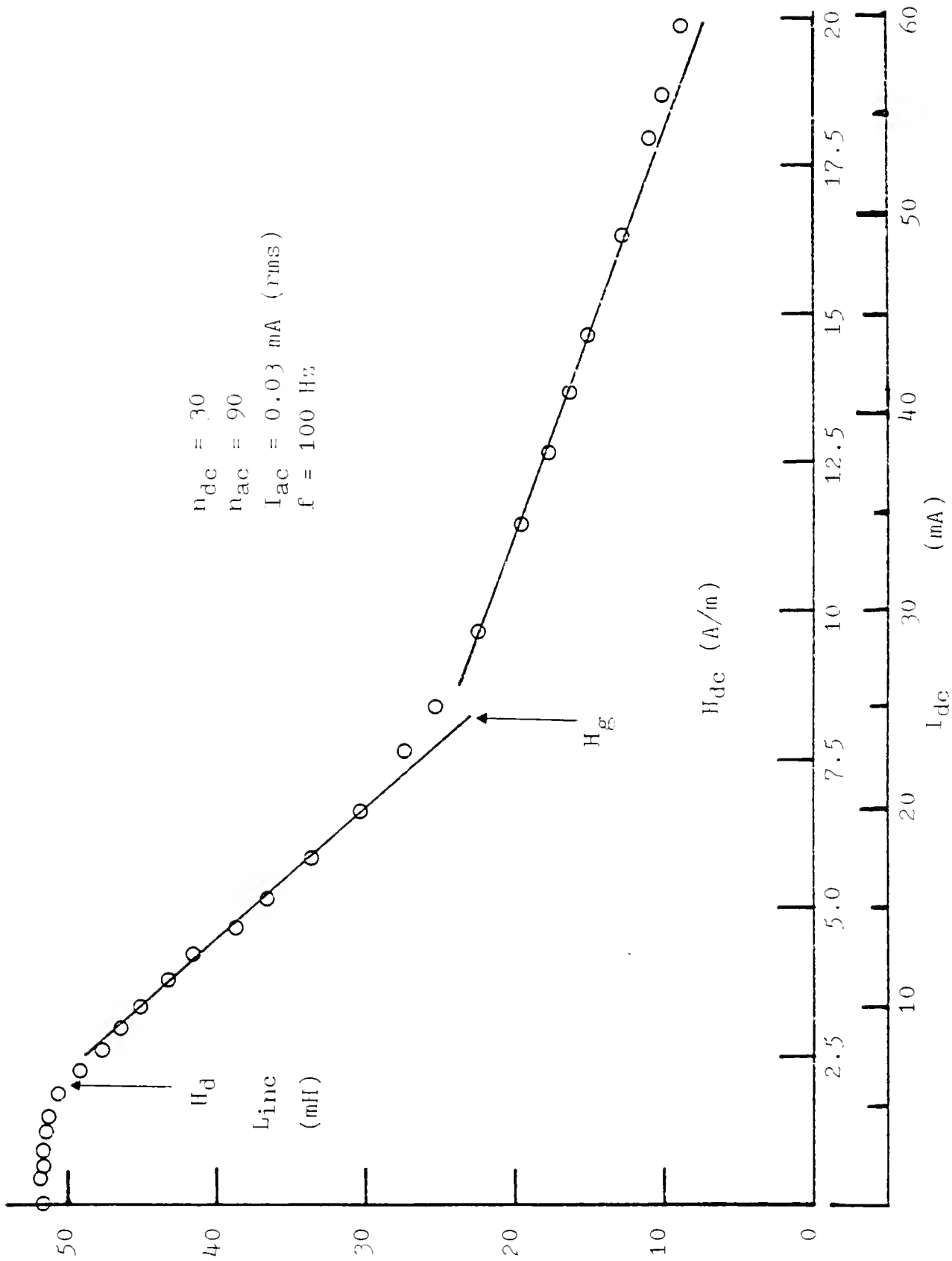Fig. 5-5 Incremental inductance of core #1.

Fig. 5-6 Incremental inductance of core #8.
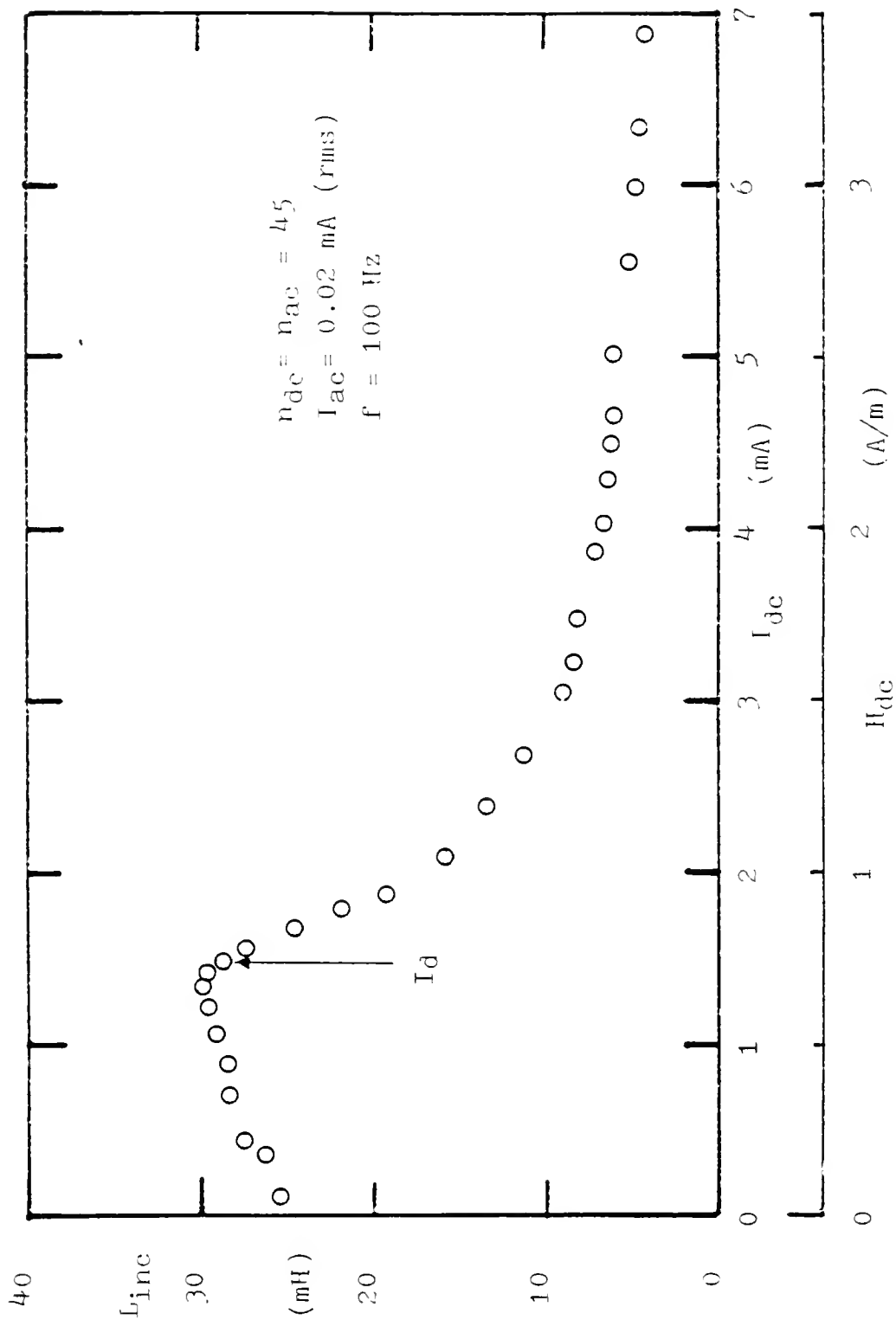
Fig. 5-7 Incremental inductance of core #14.

H_d is found from the intersection of two linear regression lines. Beyond the second region, for Metglas and core #8, there is an extra region where incremental inductance decreases linearly with another slope. For this reason, the decreasing slopes for these two regions are indicated as g_1, g_2 separately and the demarcation point of these two linear decreasing regions is indicated as H_g, shown in Figs. 5-3 and 5-6.

When the incremental inductance, L_{inc}, is plotted as $Log(L_{inc})$ versus $Log(I_{dc})$, as shown in Figs. 5-8 through 5-13, the inductance in the third region is found to decrease in proportion to the -kth power of I_{dc} (or of H_{dc}, since H_{dc} is proportional to I_{dc}). Each different material was found to have a different k value. The separation point between this region and the linear decreasing region is indicated as H_e. (this point is calculated by averaging the field at which the linear decreasing region ends and the field where the third region begins).

The demarcation of these three regions as a function of field strength depends on the type of material been considered. Demarcation points between one region and another are not sharp. The values of H_d, g (g_1 and g_2 for Metglas and core #8), k, H_d and H_e of incremental inductance are listed in Table 5-1 for each of the six materials. The critical field H_d will be studied in chapter 7, a plausible physical model of incremental inductance is given in chapter 9.
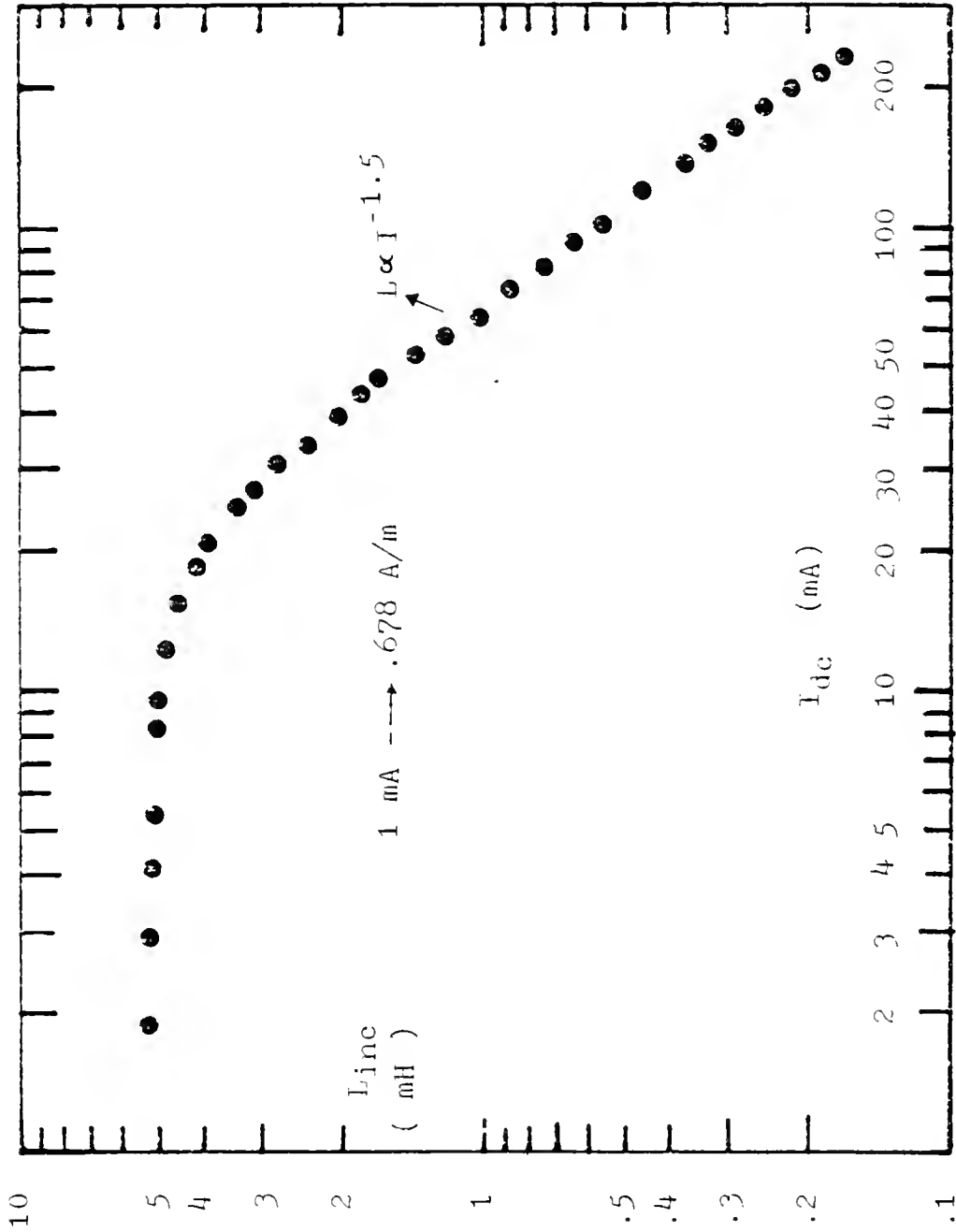
Fig. 5-8 Incremental inductance of ferrite core on log-log scale.
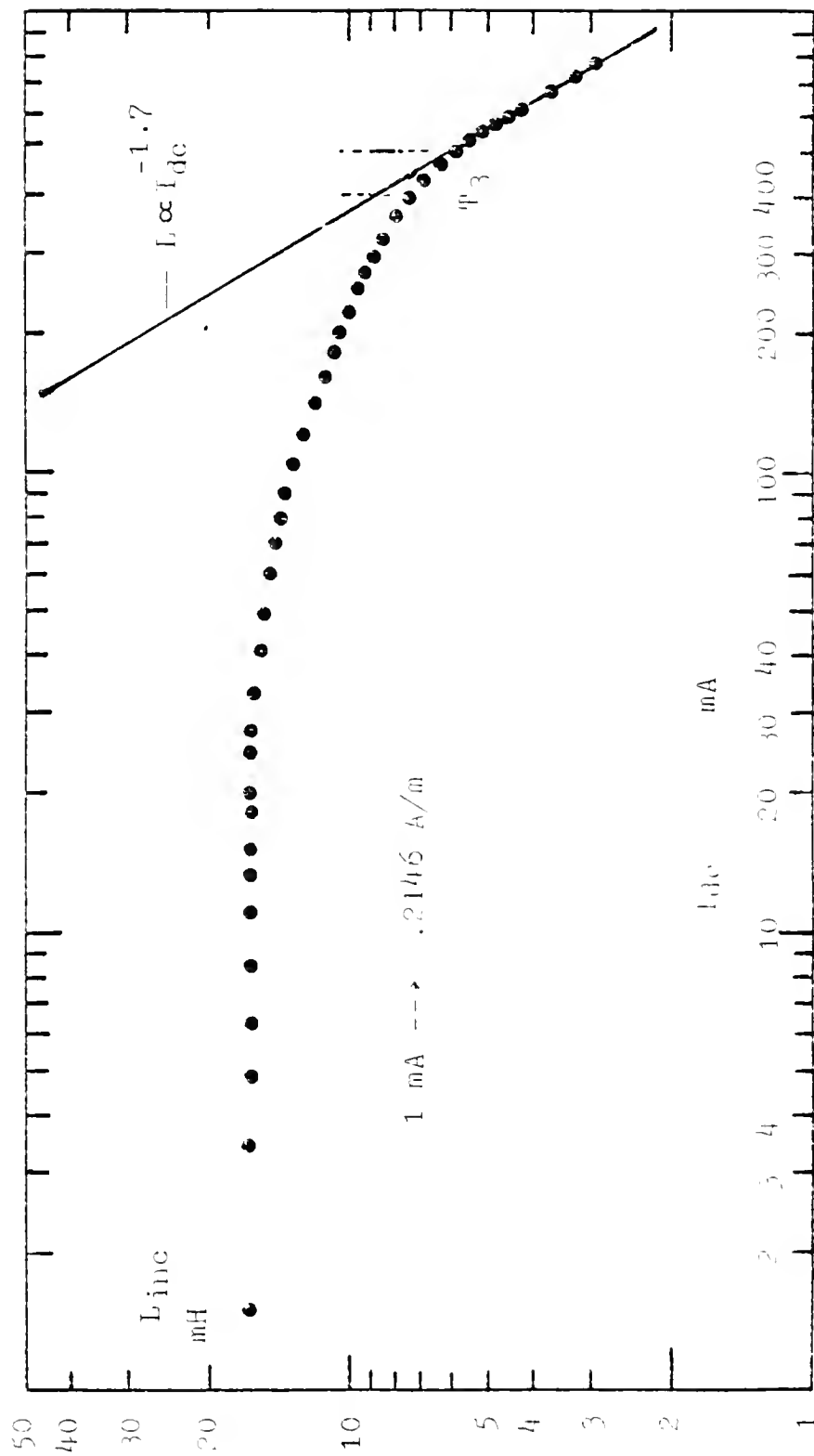
Fig. 5-9 Incremental inductance of Metglas core on log-log scale.
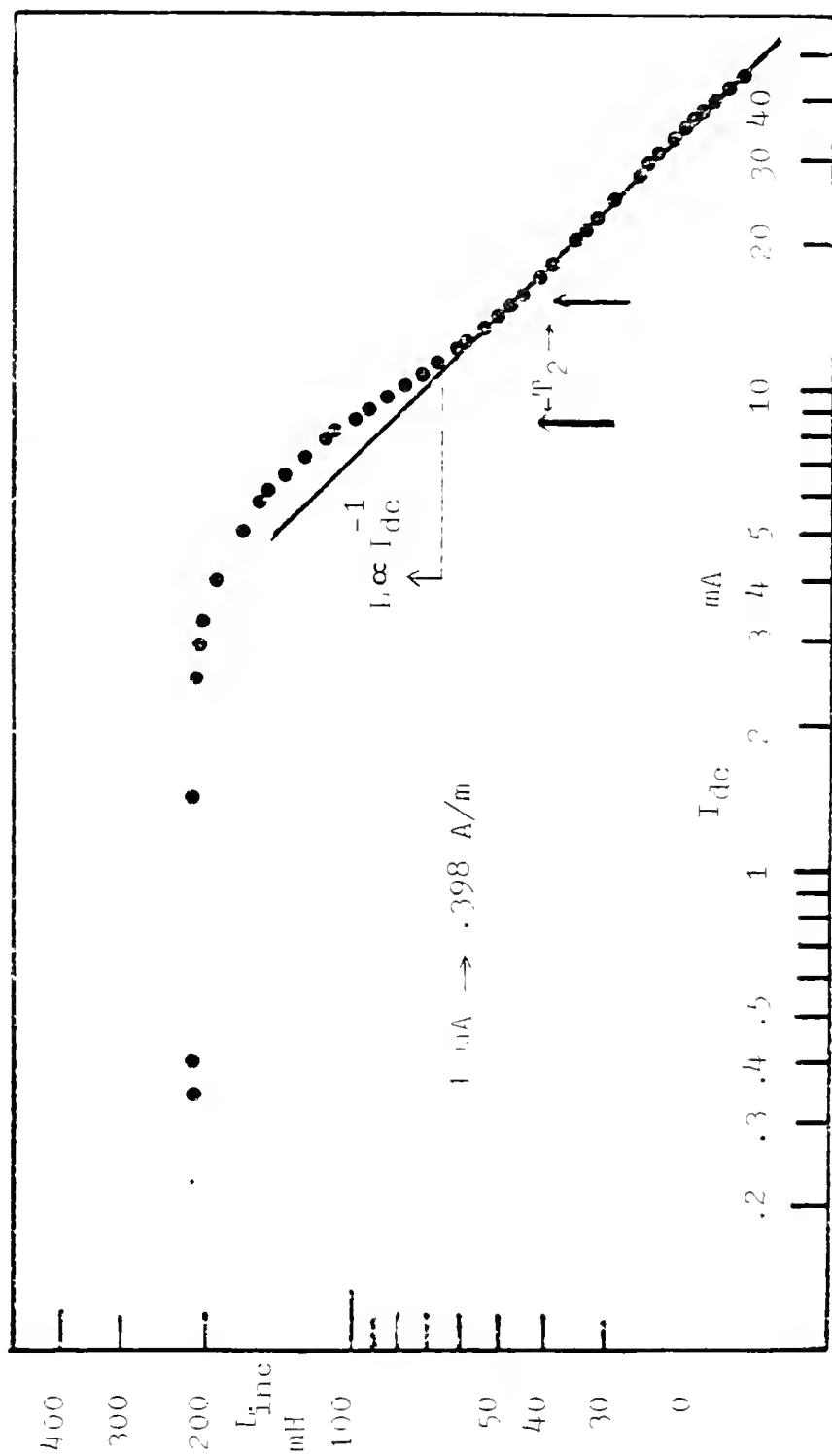
Fig. 5-10   Incremental inductance of core #6 on log-log scale.
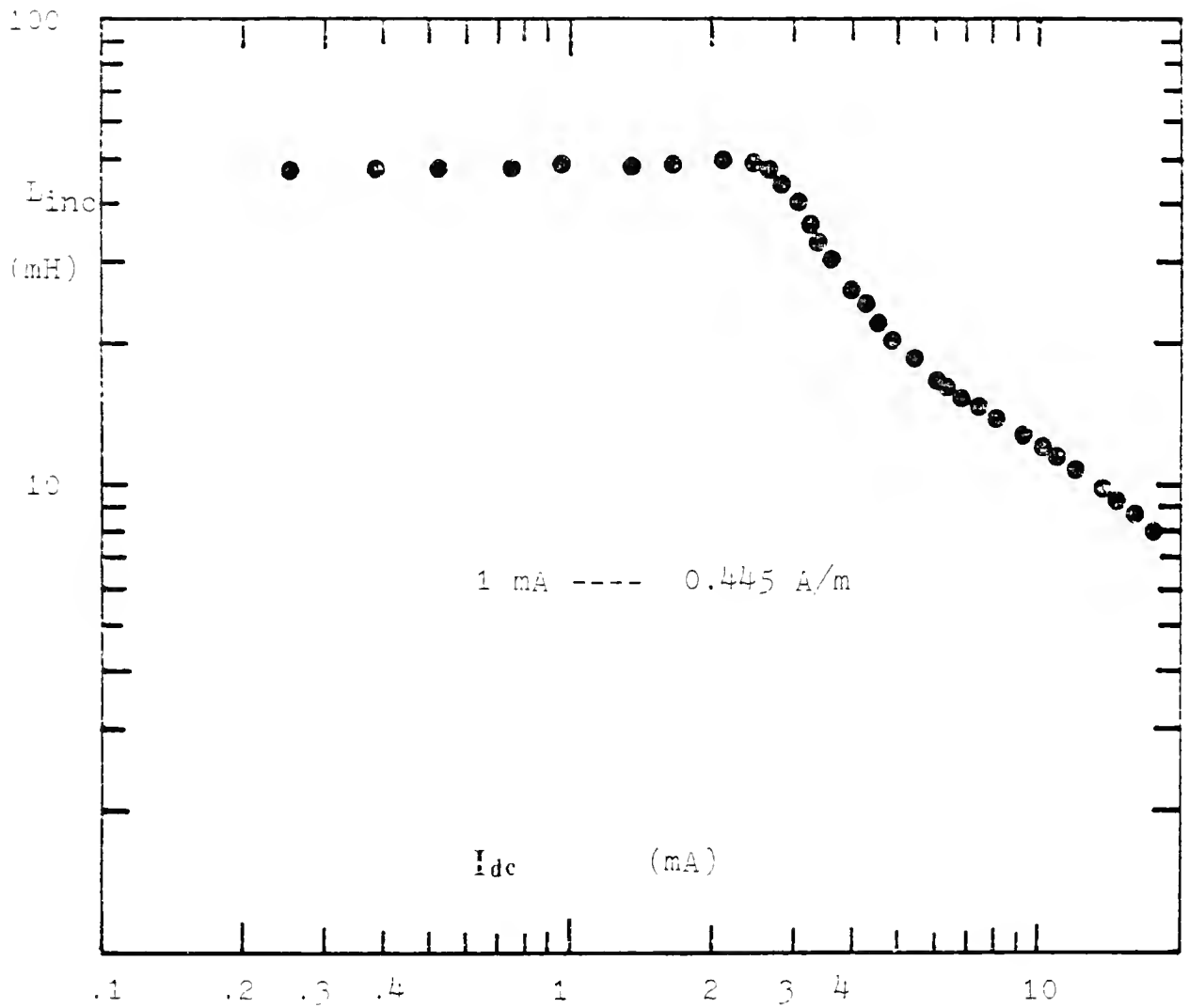
Fig. 5-11   Incremental inductance of core #1 on log-log
            scale.
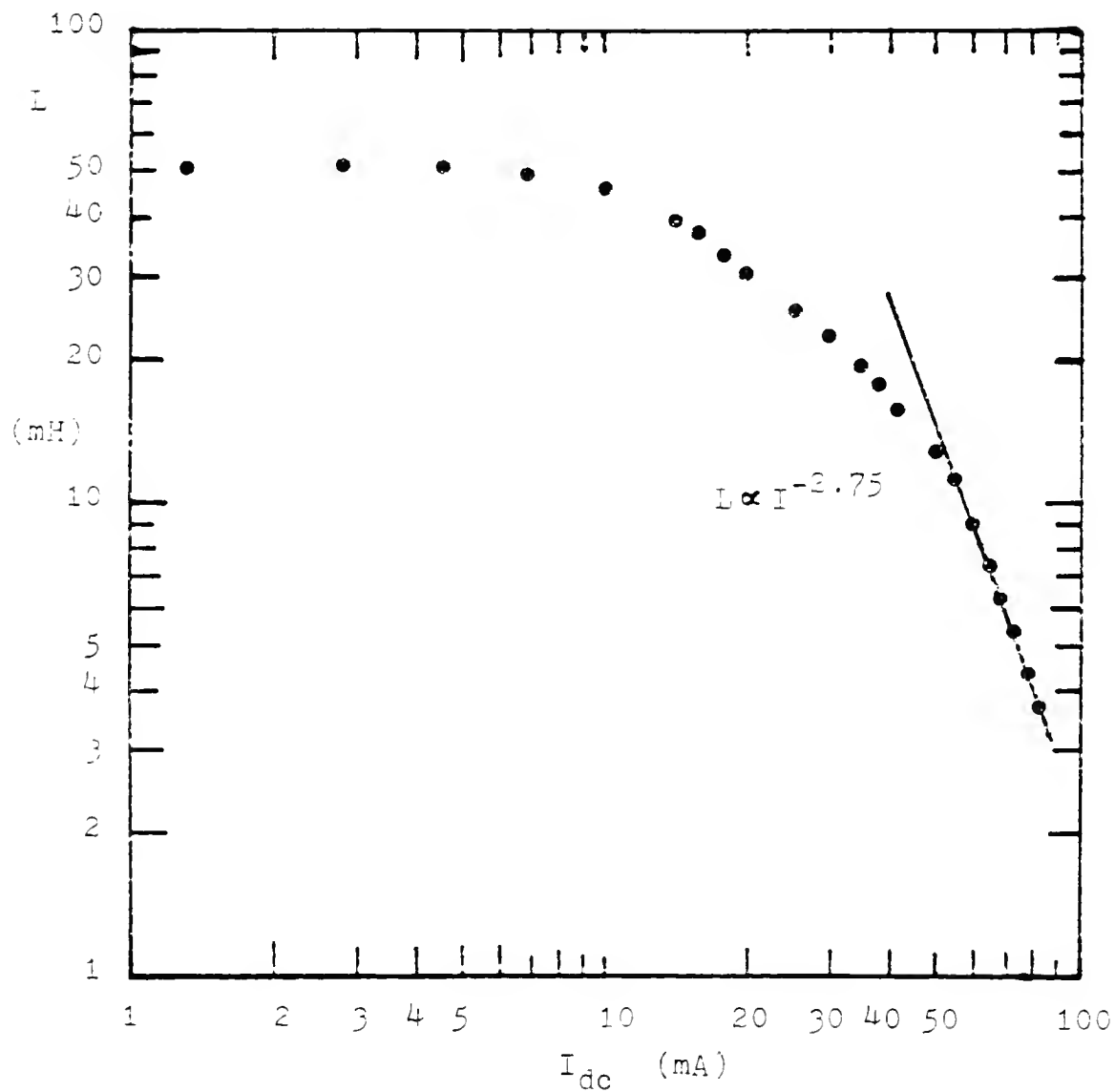
Fig. 5-12   Incremental inductance of core #8 on log-log
            scale.
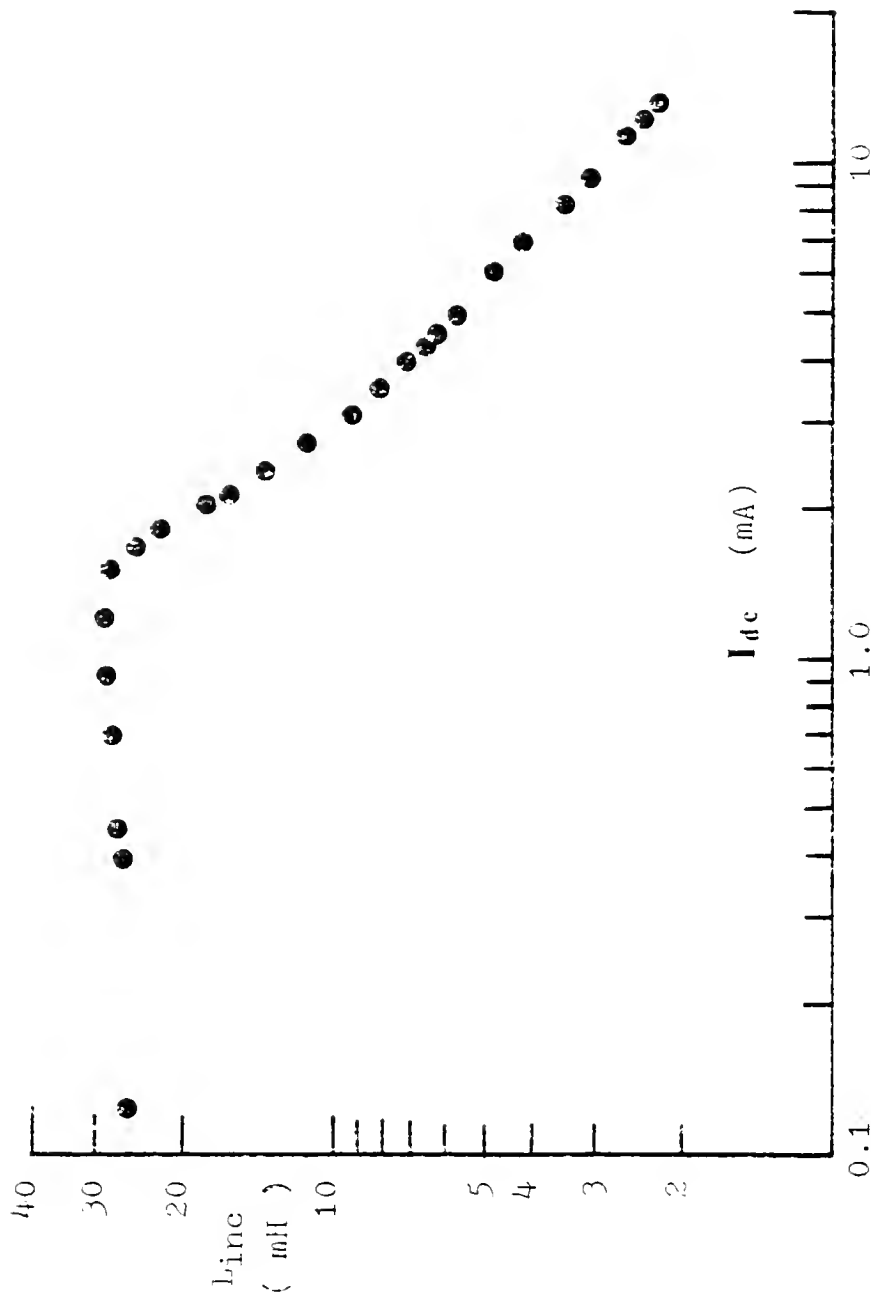
Fig. 5-13 Incremental inductance of core #14 on log-log scale.

Table 5-1　Parameters of Six Core Materials.

Parameter	Core Material					
	Ferrite	Metglas	Core #6	Core #1	Core #8	Core #14
H_d (A/m)	5.95	5.15,34(H_{d2})	1.2	0.89	2.0,7.5(H_{d2})	0.75
H_e (A/m)	27.5	97.5	4.65	2.67	17	1.5
g(m/A)	2.66×10^{-2}	$1.1 \times 10^{-2}(g_1)$ $5.23 \times 10^{-3}(g_2)$	1.81×10^{-1}	0.435	$7.17 \times 10^{-2}(g_1)$ $3.95 \times 10^{-2}(g_2)$	0.76
k	1.5	1.7	1.0	0.8	2.75	1.0

It is interesting to compare among the results of the three 1 mil permalloy cores. The plot of incremental inductance of core #8 (Fig.5-6) shows two regions of linearly decreasing incremental inductance, while for core #1 (Fig.5-5) and core #14 (Fig.5-7) show only one region of linear decrease. The critical field H_d of the three cores are different: for core #1, it is 0.89; for core #8, it is 2.0 and for core #14, it is 0.75 , all in units of A/m. The k value for core #8 is 2.75, while for core #1 it is 0.8, and for core #14, it is close to 1. The characteristic of the core is different for cores with different heat treatments. This observation is recommended for future study.

5.2 Summary

This chapter investigates the incremental inductance of inductors wound on toroidal cores of six materials.

It is convenient to divide the incremental inductance measurements into three regions of performance for each core: a low field region with a nearly constant incremental permeability, a medium field region in which incremental permeability decreases linearly with increasing field in a manner which depends on the material, and a high field region in which incremental permeability further decreases proportional to the (-kth) power of H_{dc}. Each different material has different k value. Between the second region and the third region, for Metglas and core #8, an extra

region was found where incremental inductance decreases linearly with different slope as H_{dc} increases.

The important parameters of incremental inductance made on six cores are listed in Table 5-1 for each, these include the critical field H_d, decreasing slope g, and k.

The first region and the second region of incremental inductance are of particular interest to this investigation and will be examined more closely in chapter 7. They will be correlated to power loss measurements at small field and at small induction as a function of d-c bias in chapter 9. A plausible physical process is also proposed to explain the incremental inductance in chapter 9.

CHAPTER 6
HYSTERESIS LOOP OBSERVATIONS

In this chapter, measurements are reported of the B-H loops of six magnetic materials. The six are the same as previously selected for normal inductance and incremental inductance measurements.

6.1 Introduction

The most outstanding characterisic of a magnetic material is its hysteresis loop, also called the B-H curve.

To explain the observation of a hysteresis loop, consider a toroidal core with two windings. In one of the windings the magnetizing current flows which creates the magnetic field H. The other winding is connected to a measuring instrument from which the resulting flux density may be read. Figure 6-1 shows a typical measuring circuit: The voltage across x-x is proportional to the magnetizing current, ($V_x = i_1 r$), and v_3 which is intended to be proportional to $\int V_2 \, dt$ ($=NB_m A$), is used to calculate the resulting induction, B, caused by the magnetic field strength, H. By connecting the x-x ends to the horizontal input and y-y ends to the vertical input of the oscilloscope, the B-H relation can be observed.
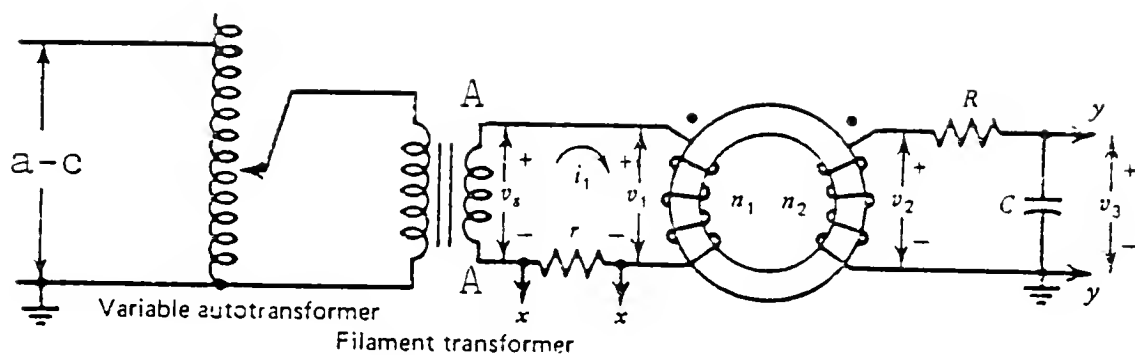
Fig. 6-1 Circuit for measuring the hysteresis loop of small toroidal cores. The hysteresis loop may also be measured without the transformers by connecting a signal generator at points A.

6.2 B-H Loops

A representative series of normal hysteresis loops is shown in Fig. 6-2a, with ferrite as an example. All the loops are symmetrical about the origin.

The value of H for which B=0 is called the coercive force H_c, and is often used as a measure of quality of the material. The value of induction for H=0 is the residual induction B_r. When the field strength has been sufficient to magnetize the material practically to saturation, the coercive force and residual induction become the "coercivity" and "retentivity". The values of H and B at the tips of a loop are usually called H_m and B_m. For an ideal "inductive" material, both H_c and B_r are zero.

When the field strength H_m is very small, the inner loop of Fig. 6-2a shows that the B-H relation has very small hysteresis. If define the slope of the line that connect the points (B_m, H_m) and the origin (0, 0) as t, the value t was found to increase as H_m increases, and the B-H loop opens up slowly as H_m increases.

When the field is increased above a certain value, which was found to be close to H_t of normal inductance, the loop begins to open up very fast. The loop is lens-shaped with its sides parabolic. The lens becomes thicker as the field strength increases. The B-H loops begin to deviate from a lens-shape and show bent- down tips in the first and third quadrants as the field increases beyond a field which was found to close to H_{mm} of normal inductance.
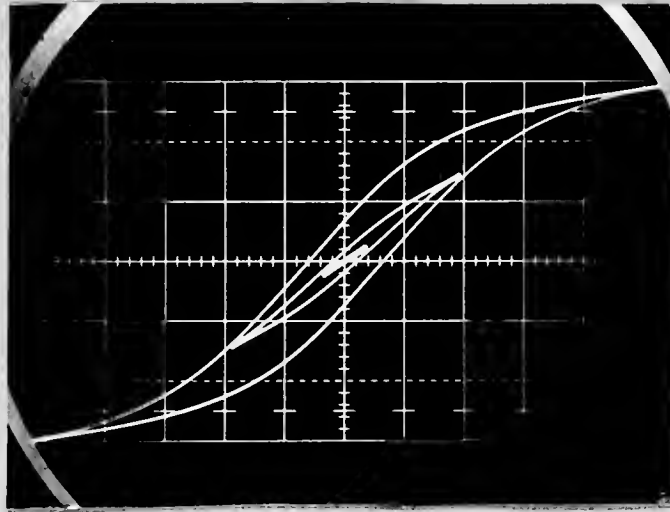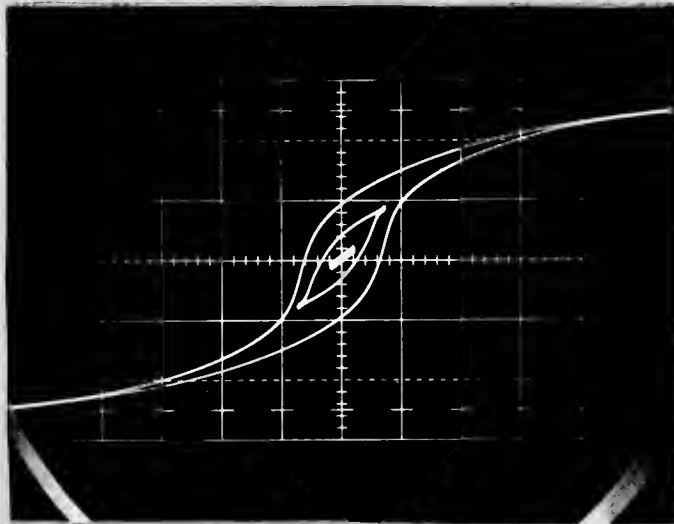
Fig. 6-2 B-H loops of (a) ferrite, f=1000 Hz,
        X=8.44 (A/m)/div., Y=.115 T/div.
        (b) Metglas, f=200 Hz, X=36.4 (A/m)/div.
        Y=.57T/div.

When H_m is increased further the horizontal width of the loop tends to become nearly the same at every value of B_m, and at the same time the loop becomes somewhat S-shaped; when H_m is still greater, the branches of the loop converge to a tail, and the shape of the loop changes only by the addition of "tails" in the first and third quadrants. The B-H loops of the other five materials are shown in Fig.6-2b through Fig.6-4. All of them show the same trend. However, each material shows its own characteristics.

The curve that connects all the tips of the loops of the family is referred to as the normal magnetization curve. Figs. 6-5 through 6-6 show examples of the curves for ferrite, Metglas, core #6 and core #8, others are not shown here.

The magnetization curves at high fields (Fig. 6-7) can be modeled with the Frolich-Kennelly equation [Bo51, p.476],

$$\frac{1}{\mu} = a + b\ H_m, \quad \mu = \frac{B_m}{H_m} \tag{6-1}$$

i.e., the reciprocal of amplitude permeability varies linearly with H_m. Assuming this relation is still valid at very high fields for the material, the saturation induction is

$$B_s = \lim_{H \to \infty} \mu H_m = \lim_{H \to \infty} \frac{H_m}{a + b H_m} = \frac{1}{b} \tag{6-2}$$
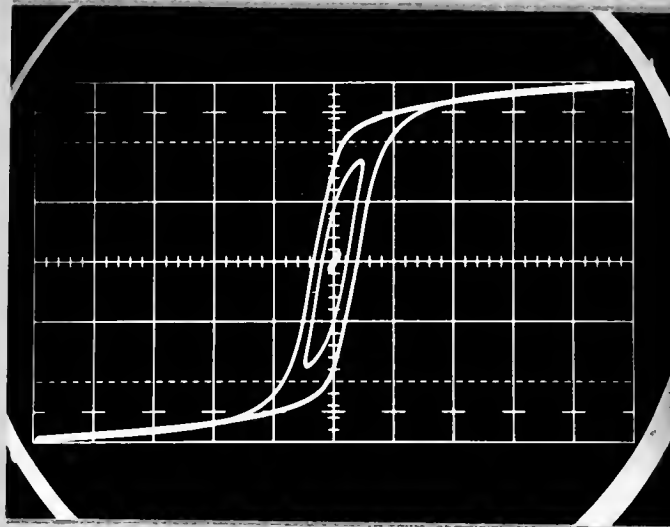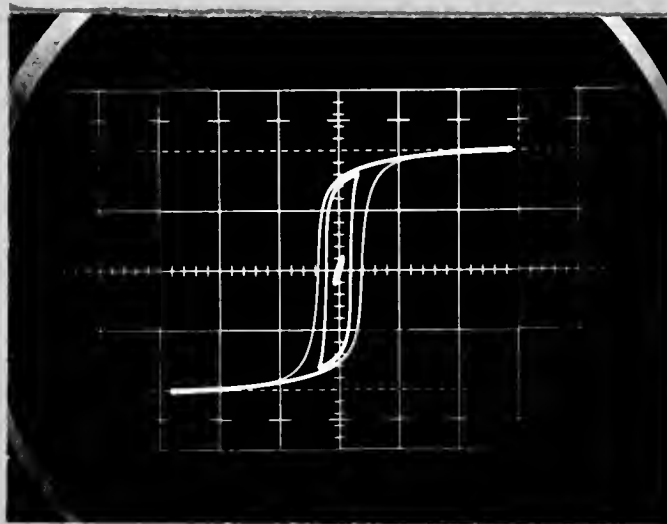
Fig. 6-3 B-H loops of (a) core #6, f=60 Hz,
          X=6.44 (A/m)/div., Y=.254 T/div.
          (b) core #1, f=400 Hz, X=13.5 (A/m)/div.
          Y=.288 T/div.
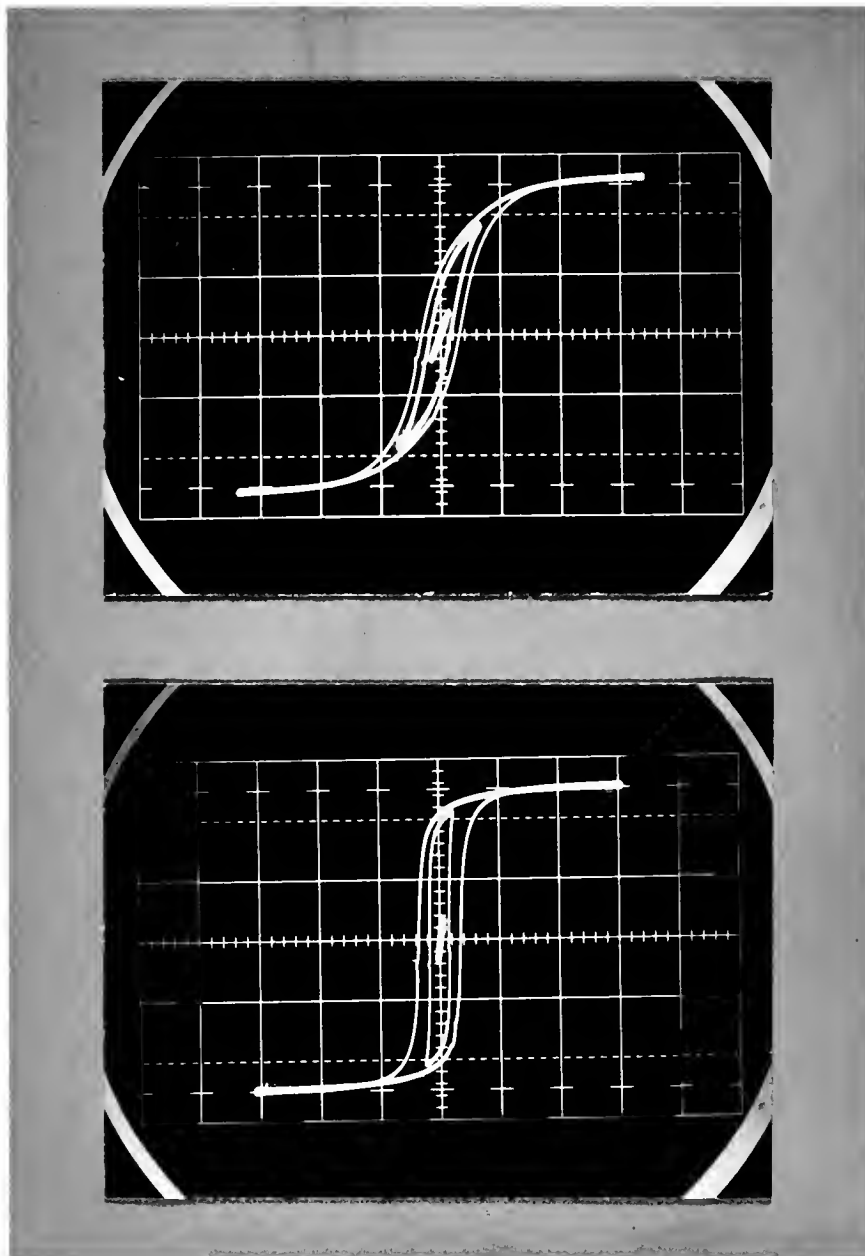
(a)

(b)

Fig. 6-4   B-H loops of (a) core #8, f=400,
           X=13.5 (A/m)/div., Y=.237 T/div.
           (b) core #14, f=400 Hz, X=11.8 (A/m)/div.
              Y=.288 T/div.
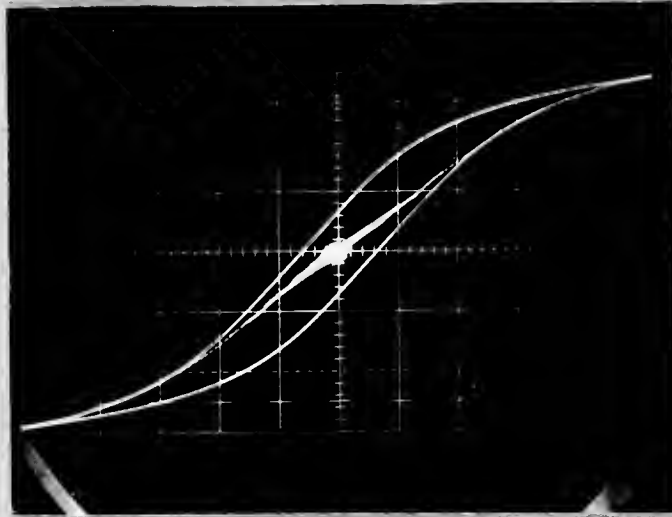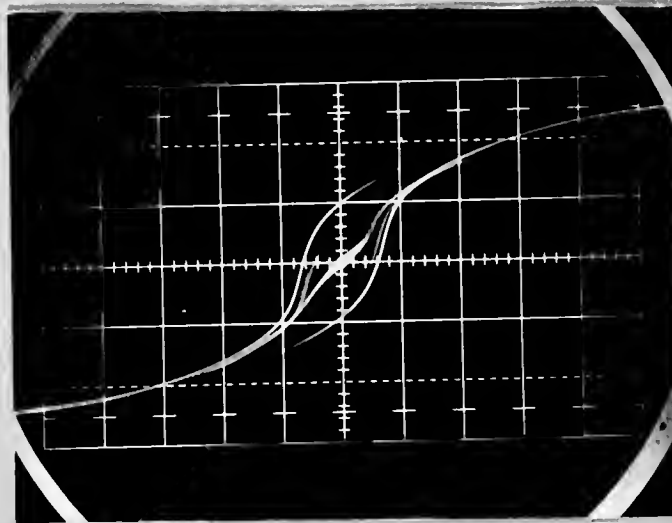
Fig. 6-5   Magnetization curve and major loop of
(a) ferrite, f= 1000 Hz, X=8.44 (A/m)/div.
Y=.115 T/div.   (b) Metglas, f=200 Hz,
X=36.4 (A/m)/div., Y=.57 T/div.
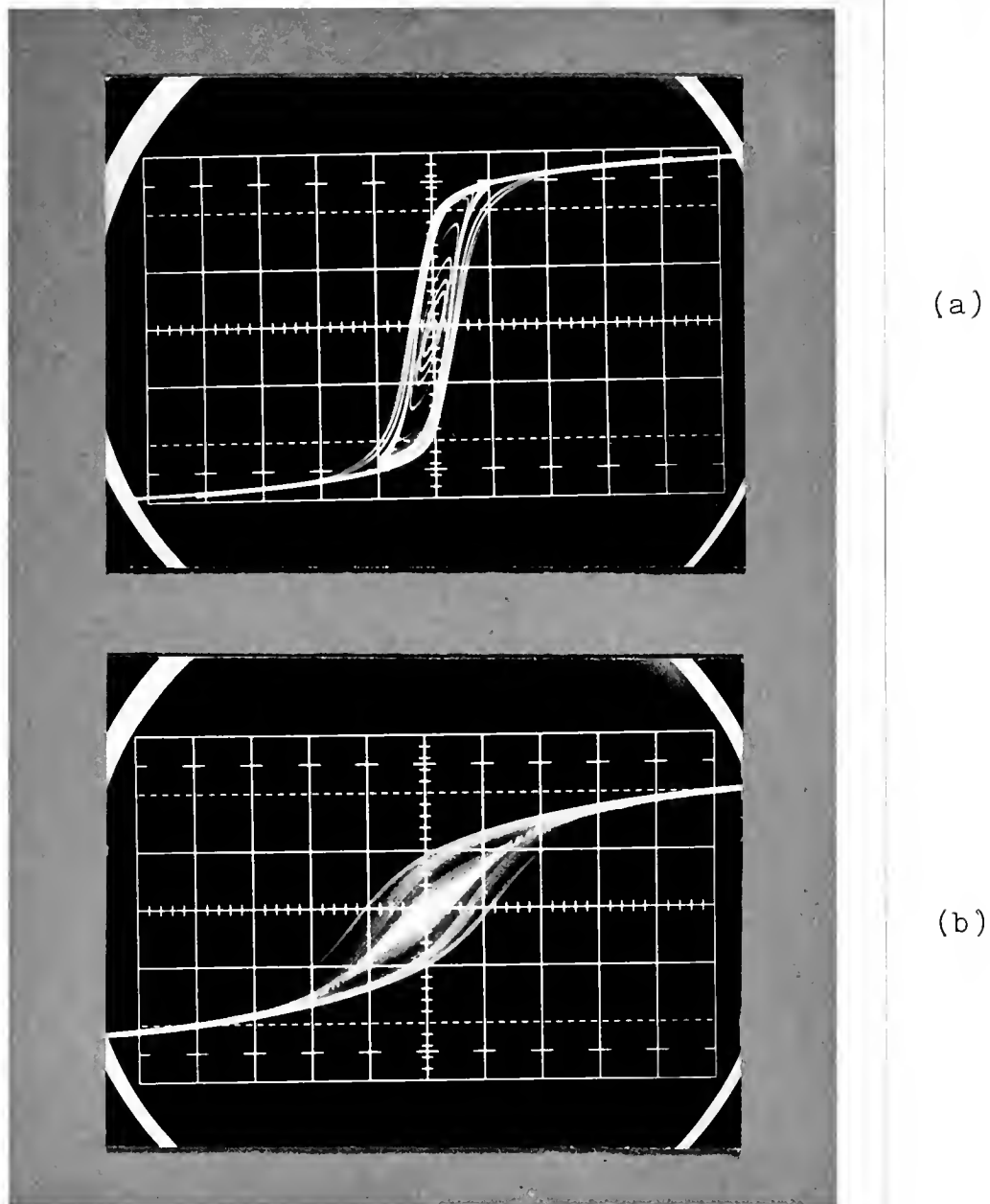
Fig. 6-6   Magnetization curve and major loop of (a) core
#6, f=60 Hz, X=6.44 (A/m)/div., Y=.258 T/div.
(b) core #8, f=200 Hz, X=3.81 (A/m)/div.,
Y=.315 T/div.

(a)
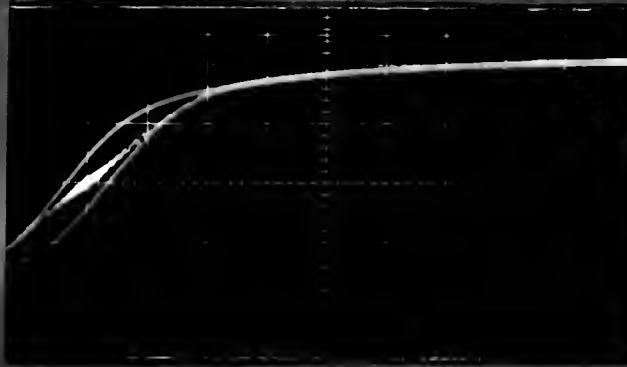
X 15.6, Y= .18, f= 2000.

(b)
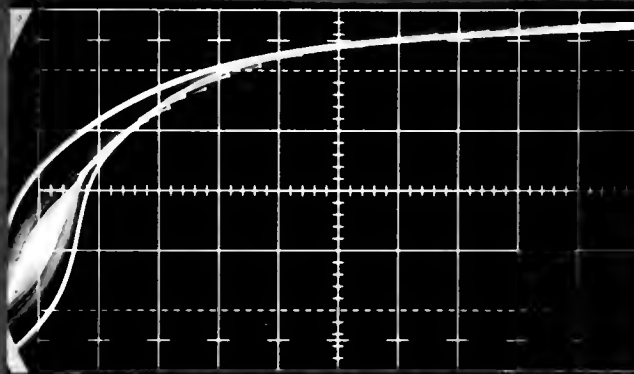
X= 10.45, Y= .356, f= 100.

(c)
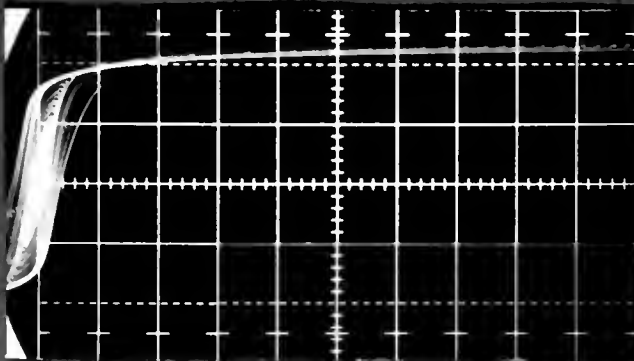
X= 48.2 Y= .39 f= 100.

Fig. 6-7   Magnetization curve at high fields. X in units of
           (A/m)/div., Y in units of T/div., f in units of Hz.
           The curve can be modeled by the equation
           $B/H = 1/(a+bH)$.
           (a) ferrite, a=39.3, b=2.378, $B_s=1/b=0.42$ T.
           (b) Metglas, a=34, b=.643, $B_s=1/b=1.56$ T.
           (c) core #6, a=3.65, b=1.18, $B_s=1/b=0.85$ T.

The calculations show that B_s = 0.42, 1.56, 0.85 Teslas for ferrite, Metglas and core #6 respectively. Comparing with catalog values 0.42 (ferrite), 1.61 (Metglas), and 0.7 (core #6) Teslas, we found close agreement. The three 1 mil tape wound permalloy cores have not been studied with this equation.

The B-H loops of the three special anneal permalloy cores, as have been shown in Figs. 6-3b, 6-4a, and 6-4b, show that magnetic annealing has a dramatic effect on B-H relations: the sides of loop of core #8 (Fig.6-4a) are sheared-over when comparing to those cores without magnetic anneal: core #1 and core #14 (Figs.6-3b, 6-4b). The sides of B-H loops of core #1 and core #14 are almost vertical.

The important experimentally-determined parameters of B-H loops of each of the six cores are listed in Table 6-1, these include H_c and residual inductance B_r at a specified B_m, the difference B_m-B_r, and the ratio B_r/B_m. For each core the specified B_m is less than saturation.

6.3 Summary

This chapter gives results of measurements of B-H relations of six inductor core materials.

Each material shows that in low fields, there is a region where B-H loop has slope t with small hysteresis, and t was found to increase as H_m increases, B-H loops open up gradually but slowly as H_m increases. When H_m is increased beyond H_t of normal inductance, B-H loops of all the cores

Table 6-1. Parameters of Hysteresis Loop For Six Cores.

Material	parameters					
	B_m(T)	B_r(T)	B_m-B_r(T)	B_r/B_m	H_c(A/m)	f(Hz)
Ferrite	0.333	0.08	0.253	0.241	5.06	1k
Metglas	1.431	0.532	0.899	0.372	21.8	200
Core #6	0.761	0.431	0.33	0.567	2.38	60
Core #1	0.708	0.538	0.17	0.756	5.0	400
Core #8	0.709	0.30	0.409	0.423	4.11	400
Core #14	0.72	0.593	0.127	0.824	4.25	400

begin to open up very fast and become lens-shaped. The region where B-H shows small hysteresis and the region where B-H shows lens-shaped loop are of particular interest and will be studied more in chapter 7 and chapter 8.

When H_m is high, B-H loop becomes S-shaped. Three materials (Ferrite, Metglas and Core #6) are selected to study the magnetization at high H_m (shown as the tail of the S loop). All of the three were found to fit the Frolich-Kennelly relation and will be discussed in chapter 8.

,

CHAPTER 7
DISCUSSION AND CORRELATION BETWEEN THE MEASUREMENTS

In the previous three chapters, the measurements of normal inductance, incremental inductance and B-H loops were made for each core as a function of field strength H. Thus, if the core material has the properties that vary with applied field strength, there may be some relationships among the measured results. This chapter examines these relationships and gives their interpretation.

7.1 Correlation Among The Measurements:

For each material, the observed value of H_t of normal inductance was found to be close to the value of H_d of incremental inductance, as can be seen from Table 7-1. The B-H loops show small hysteresis effect in the region where the applied field H_m is smaller than H_t. Above H_t, the B-H loops open up very fast as H_m increases. The relationships among the experimental results can be shown schematically as in Fig. 7-1.

The measured values of incremental permeability at low fields agree with the initial permeability. The permeability at low fields is equal to the slope of B-H loop at small fields.

Table 7-1   Threshold fields, transition ratios
            and geometric ratio for three cores

Material	Ferrite	Metglas	Core #6	Core #8
H_t (A/m)	6	5.3	1.1	2.1
I_{t2}/I_{t1}	1.8	1.31	1.5	1.15
H_d (A/m)	5.95	5.15	1.2	2.0
I_{d2}/I_{d1}	1.9	1.3	1.55	1.3
r_2/r_1	1.79	1.33	1.5	1.25
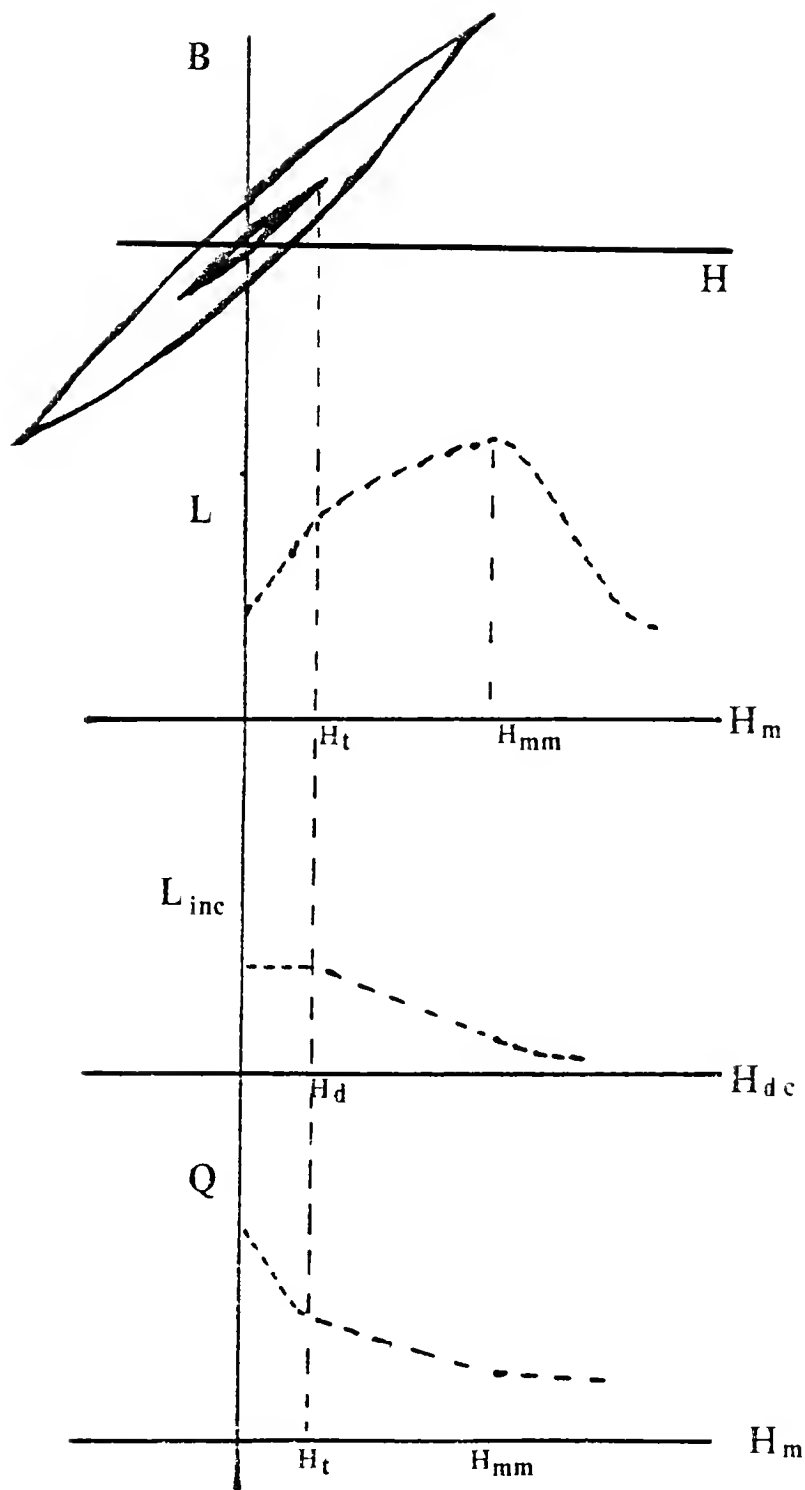
Fig. 7-1 Schematical comparision of the measurements of hysteresis loops, normal inductance, incremental inductance, and Q factor as a function of field strength.

We have found that around H_t of normal inductance, and around H_d of incremental inductance, the transition from one region to another is not sharp. In fact, the broader the transition region has been observed, the higher the ratio of dimensions r_2/r_1, where r_2 is the outer radius and r_1 is the inner radius of the toroidal core. Figure 7-2 and 7-3 are shown from detailed measurements of normal inductance of core #6 and Metglas cores. The slope changes gradually from a_1 to a_2 around the field H_t.

Figures 7-4 and 7-5 show the detailed variation of incremental inductance of #6 and ferrite. The transition ratios, I_2/I_1, around H_t and around H_d, and the dimensions ratio r_2/r_1 for ferrite, Metglas and core #6 and core #8 are listed in Table 7-1. An explanation of the data is given by a model below.

7.2 A Model to explain the transition regions

A model is now proposed to explain the transition regions. Assume a core material has the property that it can change reversal processes abruptly at a specific field strength, i.e., at H_r. For an ideal toroidal core that is uniformly wound with N turns, the field due to an applied current I

$$H = \frac{nI}{2\pi r} \qquad (7-1)$$

is inherently nonuniform at the core, tending to magnetize
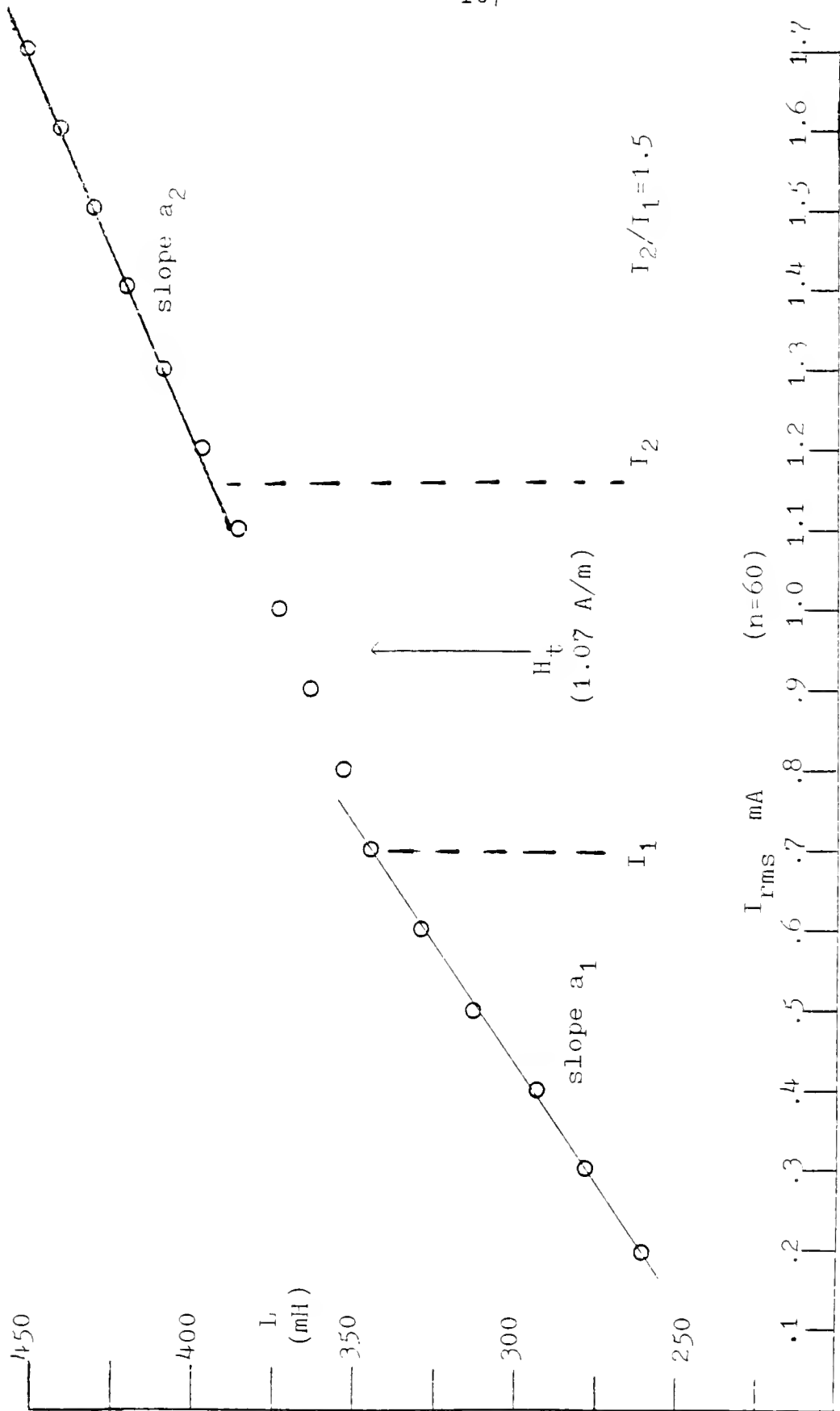
Fig. 7-2 Transition region of normal inductance of core #6.
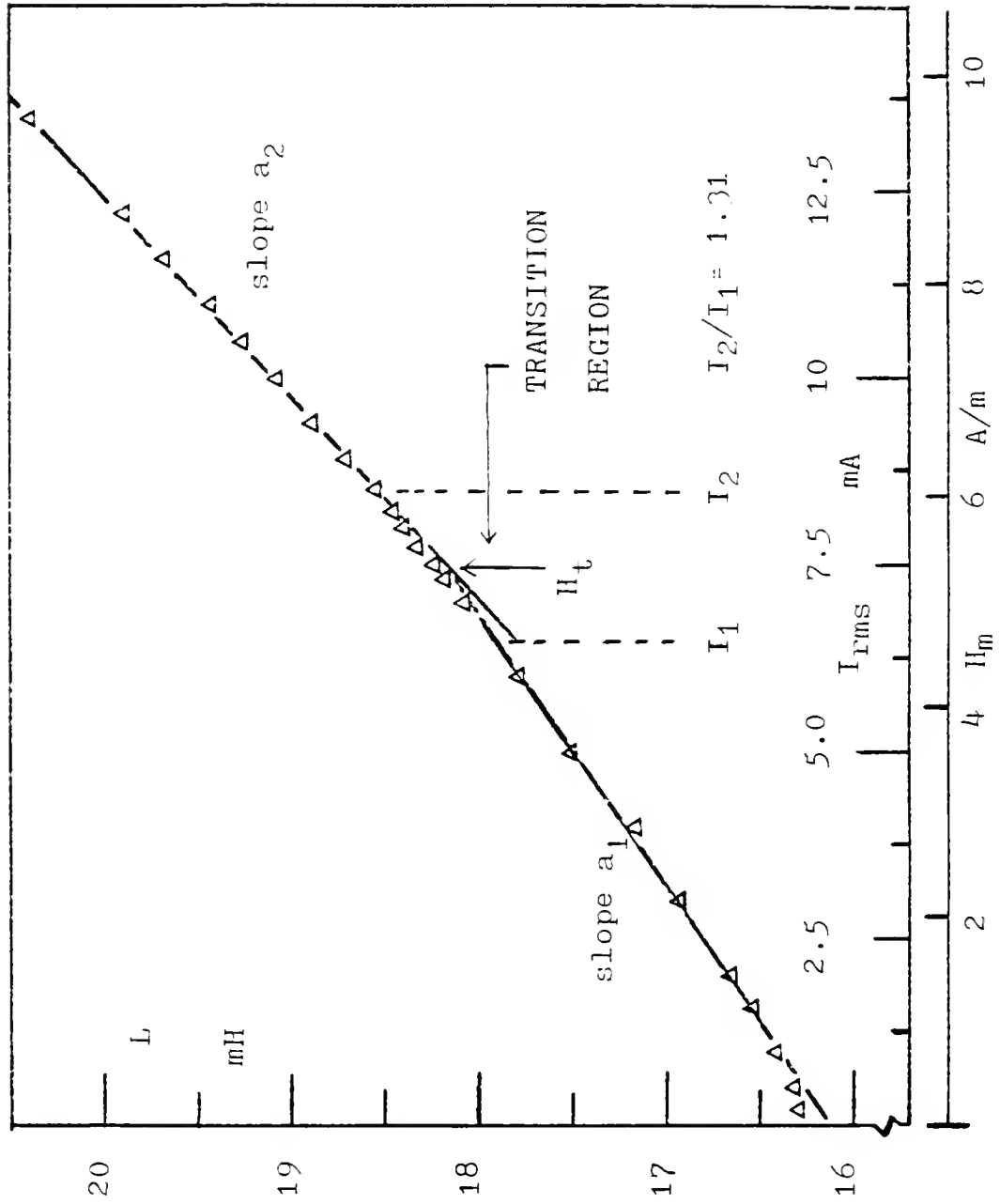
Fig. 7-3 Transition region of Metglas core.
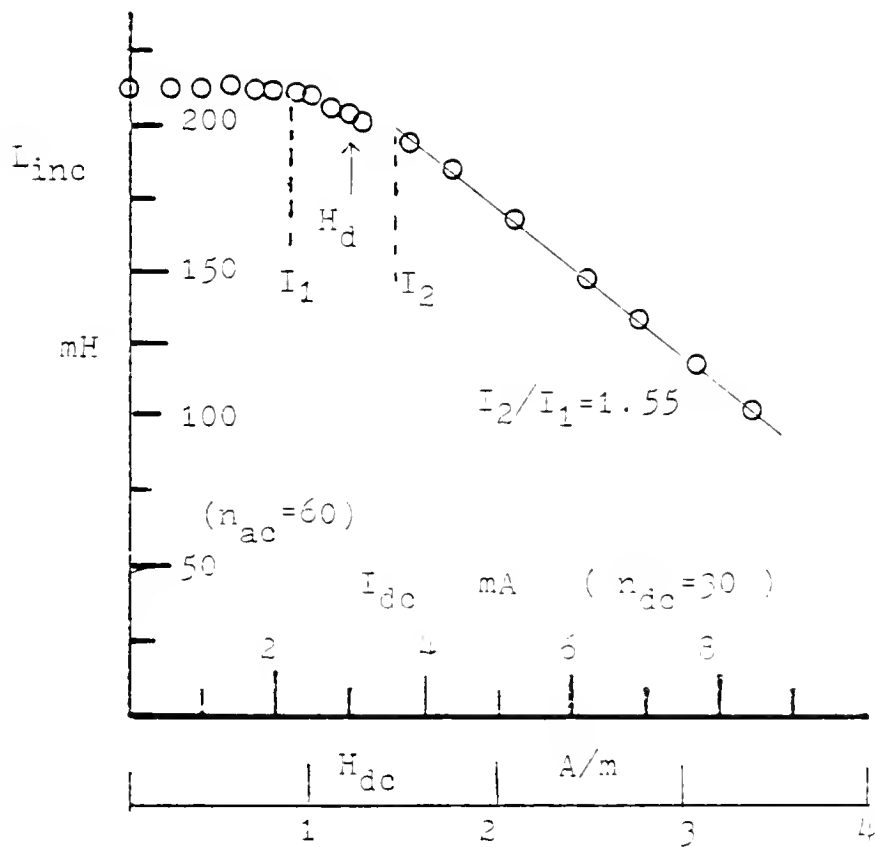
Fig. 7-4   Transition around H_d of core #6.
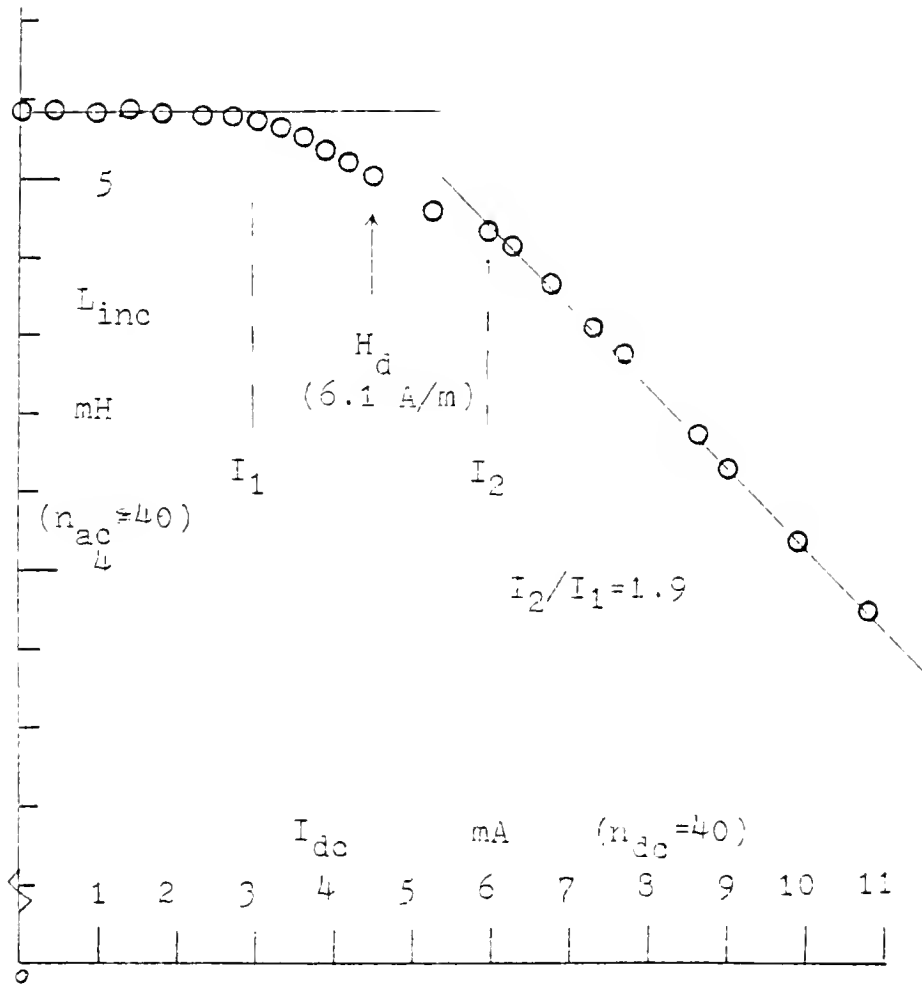
Fig. 7-5   Transition region around H_d of incremental inductance.   (ferrite)

the inside radius more strongly. Figure 7-6 shows an example of field distribution as a function of r. Assume that the current is I_1 such that the field at r_1 is

$$H = \frac{NI_1}{2\pi r_1} = H_r \qquad (7-2)$$

Then the mode of magnetization begins to change at the inner radius. The whole material would have completed the change of reversal mode when the current is increased to a value, say I_2, such that the field at r_2 (outer radius) is H_r. Thus, the ratio of the currents required for the toroidal core to start and to complete the change of reversal mode will be

$$\frac{I_2}{I_1} = \frac{r_2}{r_1} \qquad (7-3)$$

i.e., the current transition ratio is equal to the dimensions ratio. As can be seen from Table 7-1, for each core, the observed transition ratios around the fields H_t and around H_d are almost equal to r_2/r_1 within 10%. In addition, the value of H_t was found to be close to the value of H_d. The agreements support the new concept of a critical field, H_r, at which the magnetization reversal mode may change.

In the low field region of $H_m < H_t$, normal inductance was found to increase as H_m increases, thus the permeability increases with H_m. Since the hysteresis effect was found to
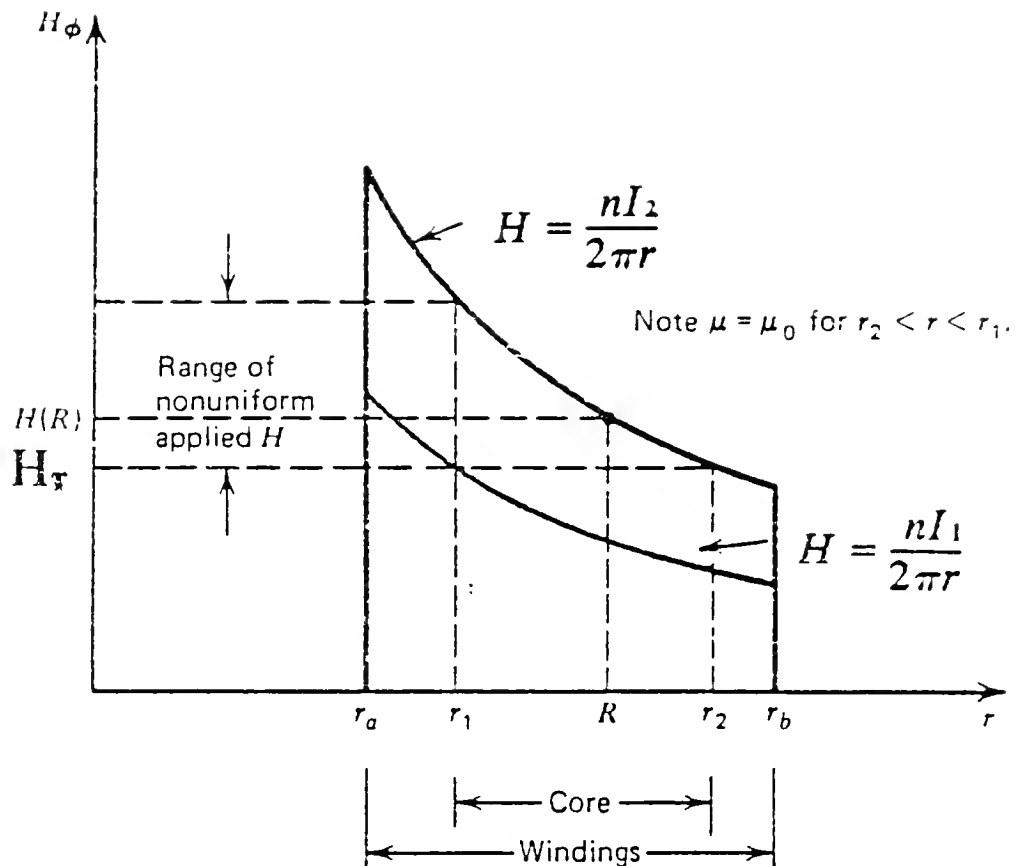
Fig. 7-6 Conceptual plot of H in direction vs radius,
for a current I in an ideal coil around a
toroidal.
The current carrying coil has radii r_a, r_b,
enclosing the magnetic core of radii
r_1 and r_2.

be small in this region of magnetization, The dominant process may be a reversible process.

The mode of reversal in the region of $H_m > H_t$ seems to change, presumably to irreversible domain wall motion. The hysteresis loops open up, the normal inductance was found to increase linearly with increasing H_m with slope a_2 at first, and then increases at a slower rate until it reaches a maximum value. Incremental inductance on the other hand decreases linearly with increasing biasing field.

In the region of $H_m > H_{mm}$, normal inductance was found to decrease with increasing field strength. The question arises whether partial saturation occurs in the core when $H_m > H_{mm}$. With H_{mm} multiplied by the maximum permeability of the material, the resulting induction, B_m, is only about 25% to 50% of B_s i.e,(0.19T for ferrite, 0.42T for Metglas and is 0.42T for core #6). This does not seem large enough to partially saturate the core.

It is interesting to note that incremental inductance further decreases at high fields in proportion to the -kth power of H_{dc}, despite different physical and chemical properties of the materials. However different materials have different values of k.

7.3 Conclusion

The relations among the normal inductance, incremental inductance and B-H loops of each of six magnetic materials have been examined.

The field, H_t, that separates the first and second regions of L is found almost identical to the field, H_d, that separates the first and second regions of incremental inductance, L_{inc}.

An explanation is proposed for the transition regions by assuming that the mode of reversal of each magnetic materials of reversal may change abruptly at a specific field strength. Thus the current transition ratio should be equal to the geometry ratio (outer diameter to inner diameter ratio) of the core. This theory is consistent with normal inductance measurements and incremental inductance measurements, within experimental errors. An validation and/or recognition of magnetic reversal models, for normal inductance and incremental inductance in the regions below and above the critical fields, are the subjects of chapter 8 and chapter 9.

CHAPTER 8
MODELS OF
NORMAL INDUCTANCE

This chapter presents models to explain the normal inductance measurements of chapter 4.

8.1   Introduction

The experimental results of chapter 4 show that in low field region, the normal inductance increases as the amplitude of measuring signal increases. Similar trend has been found on many kinds of ferromagnetic materials in the past [Bo51].

To explain this property of normal inductance, many efforts have been made. These include the model by Rayleigh [Ra87], the model by Preisach [Pr35] and the model by Neel [Ne42]. All of the above models are based on the assumption that permeability is a state value of the material, and this value varies with the amplitude of signal level. Thus the above models can be referred to as domain-state models.

In this chapter, a new inductance model (referred to as "instantaneous" model) is proposed. This model suggests that inductance increase in proportion to the instantaneous current value, I.

It is interesting to note that both the Rayleigh model and the "instantaneous" model predict the distortion of

voltage waveform of an inductor, even if the applied current is an exact sinusoid, as can be seen in the following sections.

For this reason, distortion measurements are made on the cores in this chapter, the experimental results are compared with those calculated by each of the models. Section two presents the models and experimental data. From section three, this chapter offers explanations of normal inductance with physical models adapted from literature but with some modifications.

8.2   Inductance Models and Distortion

8.2.1   "Instantaneous" Model

If normal inductance increases in proportion to the instantaneous current value, I, then $L = L_0 (1+ a|I|)$, where a is the increasing factor of the inductance. If $I=I_m \cos \omega t$, then the instantaneous value of flux linkage is

$$\Lambda = LI = L_0(1+aI_m|\cos \omega t|)I_m\cos \omega t \qquad (8-1)$$

and the voltage across the coil is equal to $d\Lambda/dt$. The Fourier expansion of $|\cos \omega t|$ is

$$|\cos \omega t| = \frac{2}{\pi}[1+ \frac{2}{3} \cos 2\omega t - \frac{2}{15} \cos 4\omega t + \cdots] \qquad (8-2)$$

and note that

$$\cos \alpha \cos \beta = \frac{1}{2} [\cos(\alpha-\beta) + \cos(\alpha+\beta)] \qquad (8-3)$$

Thus Eq.(8-1) becomes

$$\wedge = L_0 I_m [(1 + \frac{8aI_m}{3\pi}) \cos u t + \frac{8aI_m}{15\pi} \cos 3u t + \ldots]. \quad (8-4)$$

Then the inductor voltage would be

$$V_L = \frac{d\wedge}{dt} = -uL_0 I_m [(1 + \frac{8aI_m}{3\pi}) \sin u t + \frac{8aI_m}{5\pi} \sin 3u t + \cdots] \quad (8-5)$$

and the fraction of third harmonic distortion of the voltage waveform is equal to

$$\frac{\dfrac{8aI_m}{5\pi}}{1 + \dfrac{8aI_m}{3\pi}} \quad (8-6)$$

For the ferrite core of this study, with n=30 turns, the value a is close to 35. According to this model, one would expect that the third harmonic distortion is 7.8% at I_m = 5 mA and is 13.8% at 10 mA. For core #8, the value a = 123 at n=40, and the calculated third harmonic distortion is 20.6% at I_m=5 mA, and is 30.6% at 10 mA. As will be seen in section 8.2.3, all of these values are much higher than those measured.

8.2.2   "State" Model

It has been shown by many authors [Ra87, Pe28] that the magnetization along a B-H loop of lens shape can cause a distorted flux waveform even if the applied field is an exact sinusoidal one.

Rayleigh [Ra87] developed the model that the odd harmonic distortions arise when the magnetization is along the so-called "Rayleigh Loop". He has shown that at a particular maximum field strength H_m, the third harmonic distortion

is closely related to the amplitude permeability at that field strength, and is proportional to the permeability increasing factor $\sqrt{}$. Here we adapt his model as follows:

The relation between B and H may be described by the simple loops of Fig. 8-1 over a certain range of magnetizing force, each loop being defined by a particular value of maximum magnetizing force. Each loop may be considered as constituted by two branches which join at the maximum field of the loop.

Rayleigh suggested that the equations for the upper and lower branches of the loop with tips at $H = \pm H_m$ and $B = \pm B_m$ are respectively

$$B = \mu H \pm \frac{\mu - \mu_i}{2H_m}(H_m^2 - H^2) \qquad (8-7)$$

where $\mu = B_m/H_m$. Since $\mu = \mu_i + \sqrt{}\ H_m$, which was found for most magnetic materials, then

$$B = (\mu_i + \sqrt{}H_m)H \pm (\sqrt{}/2)(H_m^2 - H^2) \qquad (8-8)$$

In dealing with alternating fields the expression for B in terms of H may be written so that the time t is the independent variable. If we write

$$H = H_m \cos \omega t, \qquad (8-9)$$

it follows that

$$B = \mu H_m \cos \omega t \pm (\sqrt{}/2)H_m^2 \sin^2 \omega t \qquad (8-10)$$

Expansion of $\pm \sin^2 \omega t$ in Fourier series yields
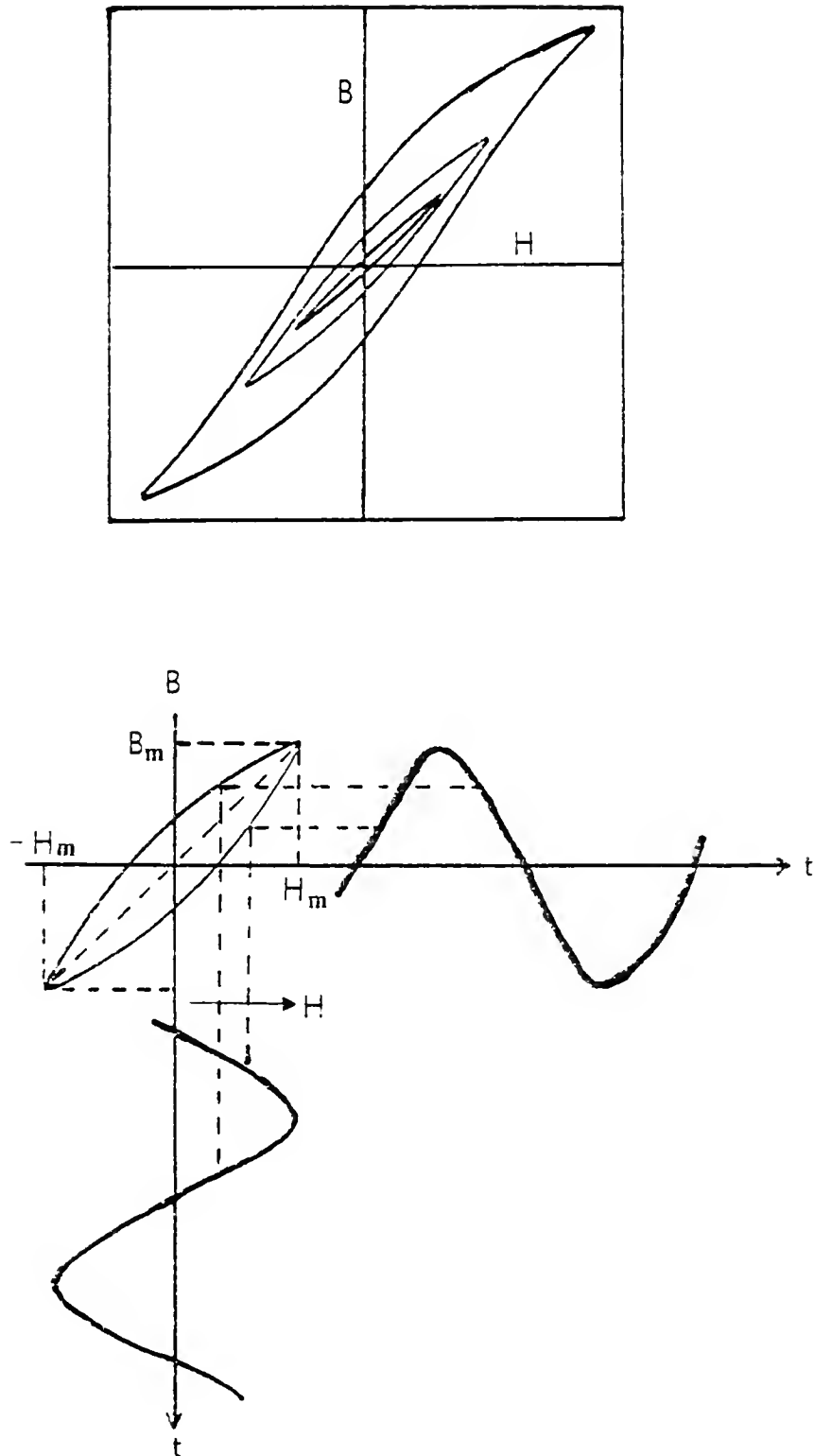
Fig. 8-1 (a) Family of hysteresis loops
          (b) Distortion of the waveform due to the
              magnetization along the Rayleigh loop.

$$B = B_m \cos \omega t + (\gamma/2)H_m [\frac{8}{3\pi}\sin \omega t - \frac{8}{15\pi}\sin 3\omega t - \frac{8}{105\pi}\sin 5\omega t + \cdots] \qquad (8\text{-}11)$$

Thus if the magnetization changes along such a loop, the shape of the waveform is deformed as shown in Fig. 8-1b, even if the waveform of the applied field is an exact sinusoidal one.

The voltage V_L across the inductor is proportional to dB/dt. By neglecting the higher order distortions, it can be written as

$$V_L = V_m \sin(\omega t - \delta) + V_3 \cos(\omega t) + \cdots \qquad (8\text{-}12)$$

Thus, the phase of the fundamental harmonic is delayed by the angle δ, and the third harmonic distortion D_3 appears, where

$$D_3 = \frac{V_3}{V_m} = 3\frac{B_3}{B_m} = \frac{4}{5\pi}\frac{\gamma H_m}{(\mu_0 + \gamma H_m)} \qquad (8\text{-}13)$$

8.2.3. Measurement of Harmonic Distortion

Measurements were made of harmonic distortion of voltage waveform across the coil as a function of current amplitude, I_m, as follows: A magnetization current, I, in the coil, is maintained nearly sinusoidal by applying a voltage source (HP 651B test oscillator) across the ends A of Fig. 8-2, where the voltage waveform distortion at A is kept under 0.2%. The coil is in series with a resistance of value nearly 20 times larger than the impedance of the coil to obtain low distortion current waveforms. Measurements of
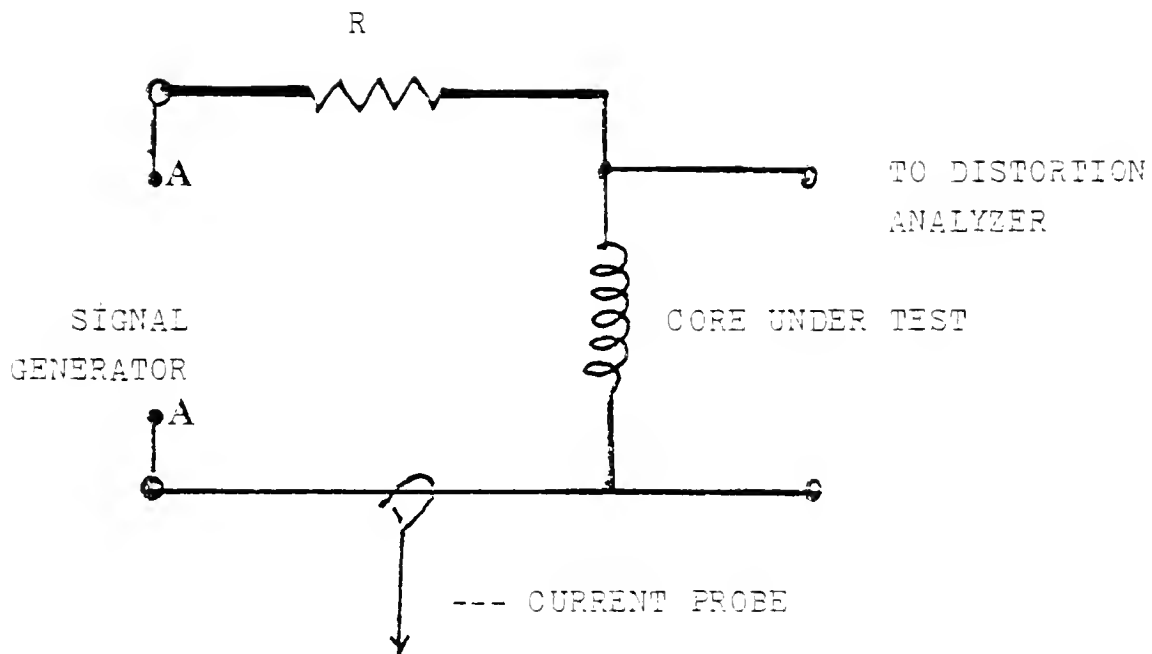
Fig. 8-2   Circuit for measurement of voltage waveform
distortion of the coil.

total harmonic distortion as a function of I_m were made by using an HP 331A distortion analyzer, with the results shown in Figs.8-3 and 8-4, for ferrite core and core #8 as examples. The waveforms were then analyzed with an HP 3582A spectrum analyzer. Most of the distortion of the waveform was found to be composed of third harmonic distortion, shown as data points in Figs.8-3 and 8-4. Dashed lines are those calculated from the "instantaneous" model, and solid lines are calculations based on the Rayleigh model. Measured data are close to the Rayleigh model at low fields. The "instantaneous" model over estimates the distortion.

8-3 A Physical Model of Inductance

Magnetization change of a magnetic material can occur by domain wall motion and/or rotation. In some specimens and in certain ranges of applied field, only one mechanism is operative; in others, both operate. For example, for "hard" magnetic material, rotation may be the dominant process in magnetization, and for soft magnetic material of inductive type, the wall motion may be the important process for magnetization, especially that of 180° wall [Ch64, Cu72, Bo51, Pr58].

Let a field H be applied with an angle θ to the wall and, to the M_s vector in one of the adjacent domains, as shown in Fig. 8-5. The pressure on the wall is $2HM_s\cos\theta$. Suppose that, when H=0, the wall is initially located at a potential energy minimum, like position a of Fig. 8-5, then
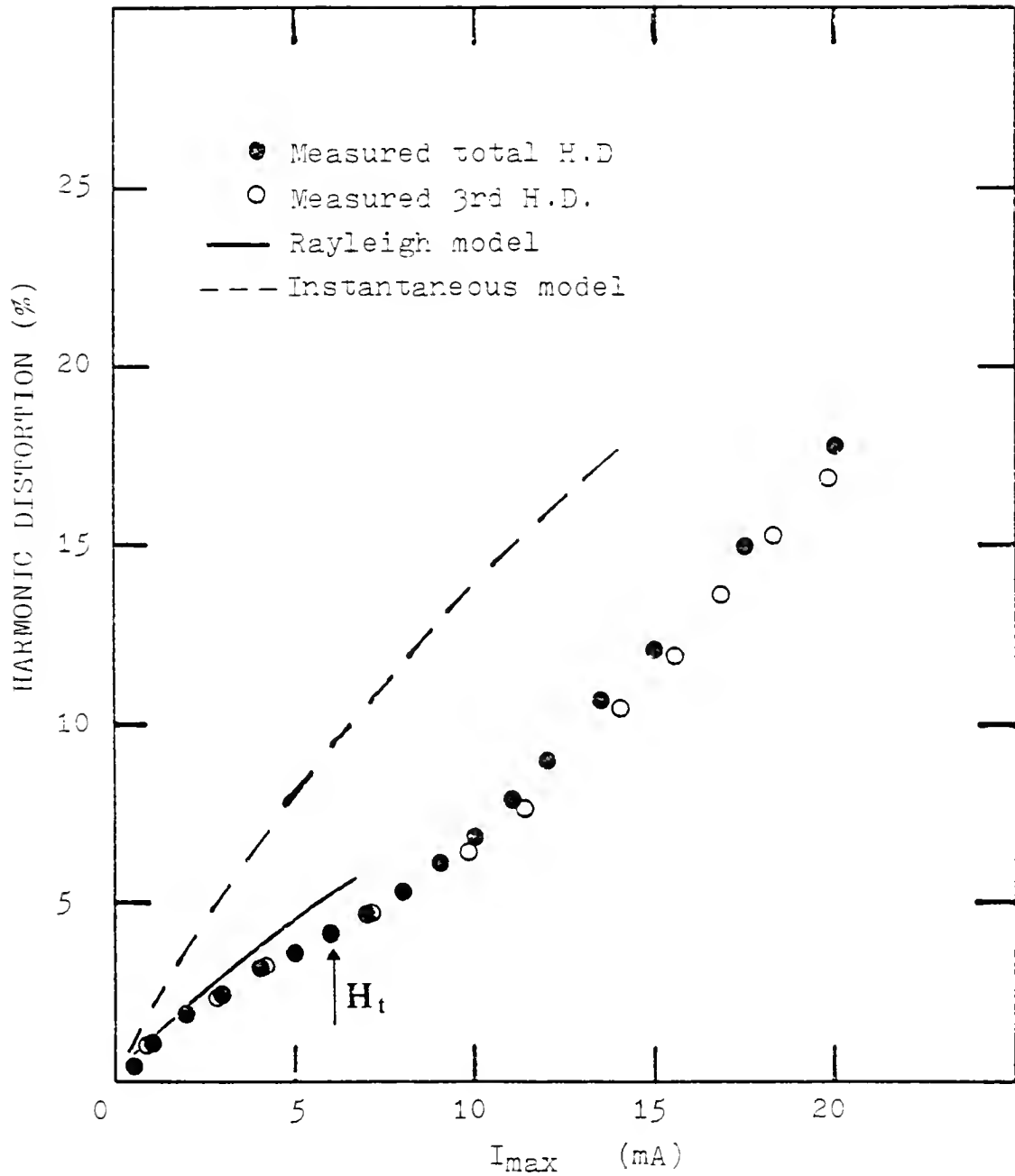
Fig. 8-3   Measured distortion of voltage waveform as a
function of peak field strength.   Also shown
are curves calculated by models.
(ferrite core, f=1000 Hz.)
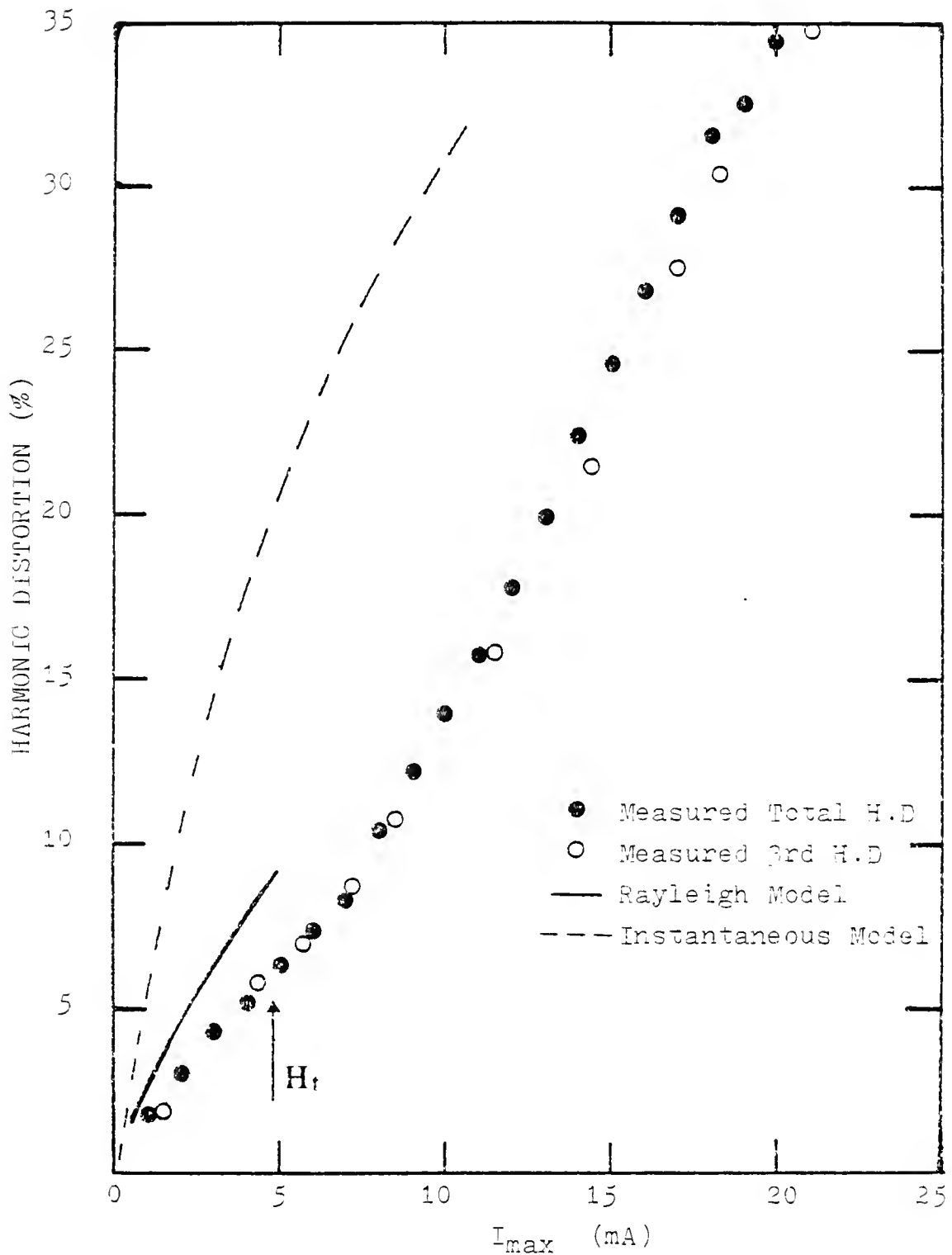
Fig. 8-4   Measured distortion of voltage waveform as a
           function of peak field strength. Also shown
           are curves calculated by models.
           (core #8, f=1000 Hz.)
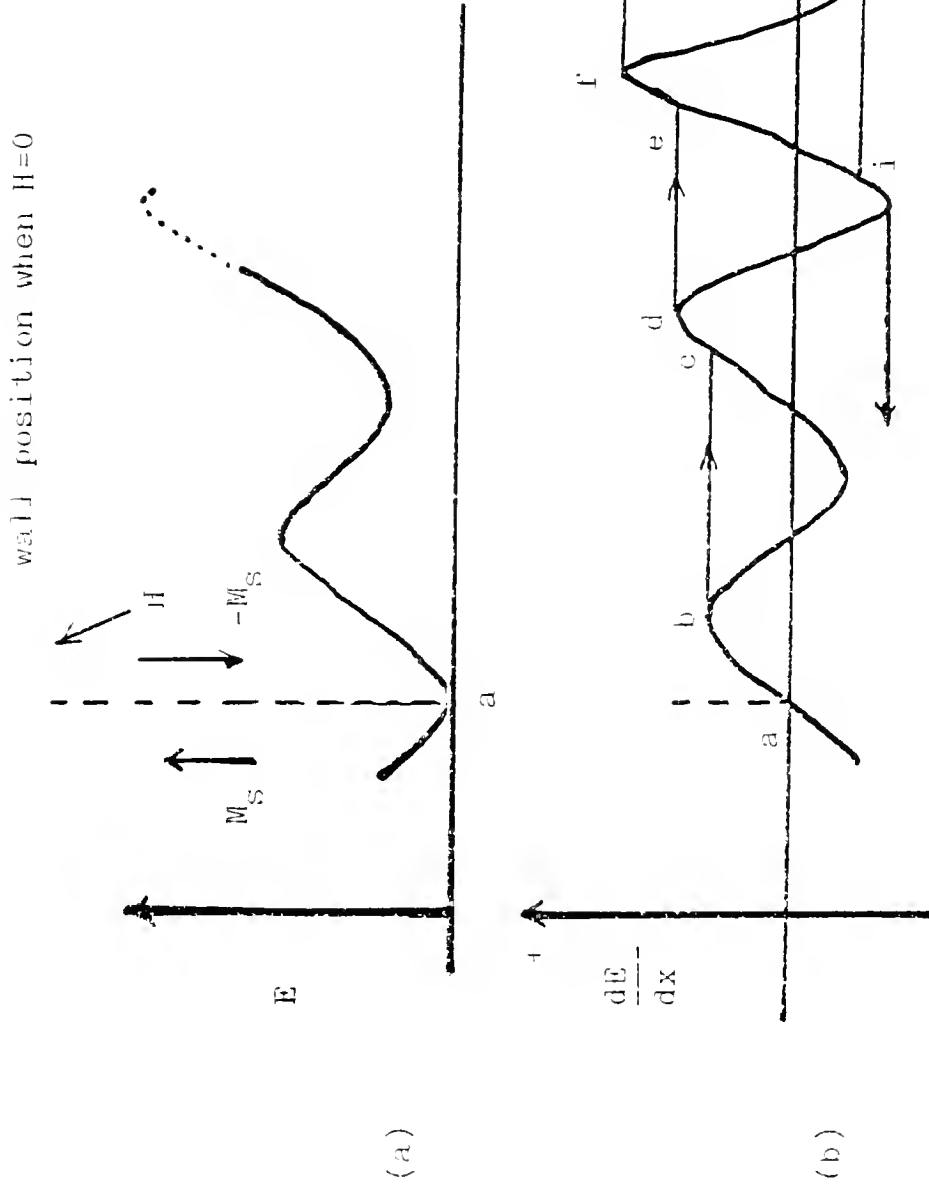
Fig. 8-5 Diagram illustrating reversible and irreversible domain wall movements.

(a)

(b)

the equation of motion of the wall per unit area is

$$m\ddot{x} + \beta\dot{x} + \alpha x = 2M_s H\cos\theta \qquad (8\text{-}14)$$

where x describes the position of the wall. If H is a weak alternating field, the wall might oscillate back and forth about its initial position. In fact, it will behave just like a mass on a spring acted on by an alternating force or like charge in an electric circuit acted on by an alternating emf.

The first term in this equation, the product of the mass per unit area of the wall and its acceleration, represents the inertia of the wall, or the resistance of the spins to suddern rotaton [Ch64,St54,Bo51,Wa80]. The second term represents a resistance to motion which is proportional to velocity and is accordingly called the viscous damping parameter. The third term αx represents a force due to crystal imperfections such as microstress or inclusions, and α is related to the shape of the potential energy minimum in which the wall is located. The value of α determines the field required to move out of the energy minimum.

The contribution of this area of domain wall to the permeability is proportional to x/H, where x is given by the steady-state solution of Eq.(8-14). when a sinusoidal driving field H is assumed. If the usual complex notation $H=H_0 e^{iwt}$ is used for the assumed driving field, the real part of the solution gives the real part μ' of the permeability, i.e., the change in B under the applied field H. The

imaginary part of the solution gives the imaginary part μ'' of the permeability, i.e the energy loss associate with the motion of the wall. Thus we lead to the definition of a complex total permeability $\mu=\mu'-j\mu''$, In an ordinary sample, the permeability will involve a weighted average of x /H, taking account of the dimensions of the domain wall segment, over all such segments in the sample.

Suppose now the applied field is large enough to cause the wall to have extensive wall motion, then equation (8-14) is no longer valid to describe the motion of the wall. In fact, there is no equation to predict the motion of the wall under this case, since discontinuous displacement of domain walls may occur.

To describe the discontinuous displacement, consider the curve in Fig. 8-5, which represents a possible form for the dependence of the internal free energy of the material per unit area of a wall. Using the symbol E for the energy per unit area of the wall (but not necessarily implying that the energy is localized in the wall itself), and assuming that in zero field the wall is in equilibrium at x=a, the condition for equilibrium in a field H is

$$\frac{d}{dx}(E-2HM_s\cos\theta x)=0, \qquad (8-15)$$

or

$$2HM_s\cos\theta = dE/dx. \qquad (8-16)$$

As the field increases, the wall moves reversibly to the

right until dE/dx reaches a maximum at b when the equili-
brium becomes unstable. Once the corresponding value of the
field, namely

$$H_0 \cos\theta = \frac{1}{2M_s}[\frac{dE}{dx}]_{max} \qquad (8-17)$$

is passed, the boundary moves spontaneously (i.e. without
further increases of field) to a new position of equilibrium
at c, the change from b to c corresponding to a Barkhausen
discontinuity [Ba19]. With further increase of field rever-
sible movement is assumed, when the field increases more, a
second discontinuous displacement may occur,(from d to e),
and the third and the fourth etc. The courses of the
changes when the field is decreased will be clear from the
figure. Figure 8-5 also shows how the wall movement contri-
butes to the reversible and irresversible susceptibility
(i.e.,ranges ab, cd, ef etc. corresponding to reversible
susceptibility and ranges bc, de, fg, etc, corresponding to
irreversible susceptiblity) in increasing field. The assump-
tion of not unduly specialized type of dependence of energy
on wall position thus leads to a formal coordination of a
wide variety of effects associated with a single elementary
process, and it is not unreasonable to suppose that the bulk
characteristics of ferromagnetics might arise from the
superposition of a large number of similar processes.

In the following sections, a mathematical equation will
be used to express the above descriptions. Consider in the
material, there are n domains with random distribution of

magnetization direction. Assume that under a-c excitation, the ith domain wall can displace to x_i, where x_i is the net displacement of the wall in the direction x, which is in angle θ to the applied field, then the total flux change under this a-c excitation will be proportional to the sum of all the displacements of the walls

$$\triangle\phi = M_s \sum_{i=1}^{i=n} x_i \qquad (8-18)$$

We assume that there are two categories of domain walls: in one of them, the domain walls are "pinned" and can only displaced to a very short distance, In the other category, the domain walls are free from the pinning center and can move more freely in the medium. thus Eq.(8-18) of $\triangle\phi$ can be rewritten as the sum of the displacements of domain walls in two categories separately.

$$\triangle\phi = M_s (\sum_{i=1}^{i=m} x_i + \sum_{j=m+1}^{j=n} x_j) \qquad (8-19)$$

This expression will be used to explain the experimental results of normal inductance measurements.

8.3.1 A Model For The Inductance Below H_t.

In the region where $H_m < H_t$, the B-H loops was found to have small hysteresis only, dominant process is assumed to be reversible. Question arises as why normal inductance increases as H_m increases. To explain this, a model of

domain wall motion in a stress field, which is adapted from the book by Cullity [Cu72] are extended by assuming that the strengths of the stress fields in the material are arbitrary distributed, in order to explain the increase of permeability with H_m.

Assume that at small applied field, all the domains belong to category 1; i.e, all domain walls are pinned and remain pinned whenever the applied field is small than H_t. (The domain walls, however may bow between pinning sites or displace sinusoidally with small amplitude near the the potential minimum).   Thus domain walls are in positions which minimize the energy of the system.   By "system" we mean the wall itself and/or the adjoining domains.   Thus if it is a 180° wall, either it will tend to bisect an inclusion and impede by the inclusion or be located at the point where the microstress goes through a minimum.   If a small field is then applied, the wall will move, but it moves against a force tending to restore it to its original position. This restoring force if caused by an inclusion, is due mainly to the increase in wall energy and magnetostatic energy resulting from the wall motion.   If caused by microstress, the resulting force is due to an increase in wall and magnetoelastic energy [Cu72].   Those domains pinned by inclusions can contribute a constant value to the total amplitude permeability whenever they are remained pinned [Cu72, Ch64, Bo51].   Consider the domain walls that remain at the points where microstress is minimum (Fig.8-6): The
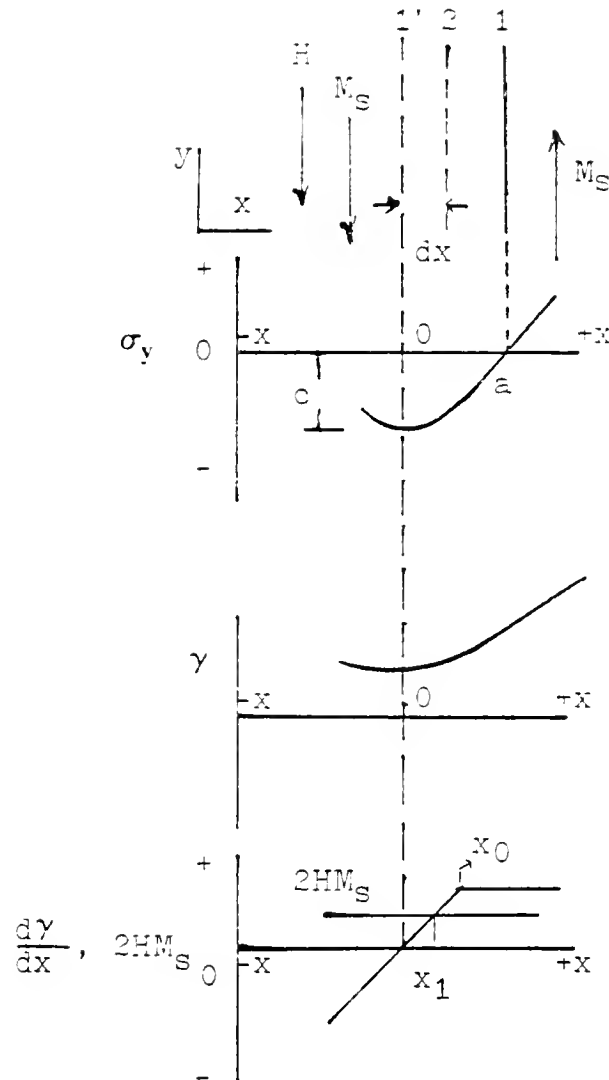
Fig. 8-6 Motion of a 180° wall in a stress field.

magnetostrictive strain in the domains on either side of a 180° wall is the same, because it is independent of the sense of the magnetization. Therefore, when the wall moves, there can be no change in the magnetoelastic energy of the domains, whatever the stress distribution. The only effect of stress is to change the energy of the wall itself. The energy of a domain wall is made up of exchange and aniso-tropy energy, assume that the exchange energy does not change with wall position and can be neglected, then the energy of the domain wall is

$$y = 2 \; k_1 \delta \qquad\qquad (8-20)$$

where δ is the wall thickness and k_1 is the crystal aniso-tropy constant. But if the crystal is under microstress parallel to the wall and to the easy axis, then a term, representing the stress anisotropy k_σ should be added . Thus

$$y = 2\delta \; (k_1 + k_\sigma) \qquad\qquad (8-21)$$

It can be shown that k_σ is proportional to the stress [Cu72]. For a stress in y direction in Fig. 8-6b,

$$k_\sigma = \frac{3}{2}\lambda_y\sigma_y \qquad\qquad (8-22)$$

where λ_y is magnetostriction constant in y direction, and σ_y is the stress in y direction. Now assume that the wall is in position 1, where the stress σ_y is zero and near the point x=a, varies linearly with x:

$$\sigma_y = h(x-a) \tag{8-23}$$

Putting this value into the expression for γ, we have

$$\gamma = 2\delta \left[k_1 + \frac{3}{2}\lambda_y h(x-a) \right] \tag{8-24}$$

since γ increases linearly with x, the wall would move spontaneously to the left of x=a in zero field. The point of zero stress is not a stable one. However, we can show that the wall will be stable in position 1', where the stress is assumed to go through a minimum and which is taken as the origin. Assume that the shape of this minimum near x=0 is parabolic:

$$\sigma_y = -c + kx^2 \tag{8-25}$$

where c and k are constants . Then

$$\gamma = 2\delta \left[k_1 - \frac{3}{2}\lambda_y c + \frac{3}{2}\lambda_y kx^2 \right] \tag{8-26}$$

and γ goes through a minimum at x=0 in Fig. 8-6b. If the field in the direction indicated moves the wall by an amount dx from 1' to 2, the change in potential energy per unit area of wall is

$$dE_p = - H M_s dx \tag{8-27}$$

The equilibrium position of the wall is given by

$$\frac{dE}{dx} = \frac{dE_p}{dx} + \frac{d\gamma}{dx} = -2HM_s + 6\delta\lambda_y kx = 0 \tag{8-28}$$

i.e.,

$$6\delta\lambda_y kx = 2HM_s \tag{8-29}$$

This is the same as Eq.(8-14) without the first two terms in left hand side, and is an equation that describes a system of a simple harmonic oscillator with applied force H without damping and mass. Thus, this process is a very low loss process. The value $d= 6\delta\lambda k$, shows that the restoring force is proportional to k, as well as to wall thickness δ and magnetostriction constant λ_y. This equation also shows that the smaller the k value of Eq.(8-18), the larger the wall movement at a specific field. The small k value correspond to the "shallow" stress minimum and the "lower" the stress gradient at points near minimum. The initial susceptibility due to this kind of process is

$$\chi_i = \frac{2M_s^2 S}{3\delta\lambda_y k} \tag{8-30}$$

where S is the wall area per unit volume.

When the applied field is increased, for the arbitrary stress distribution shown in Fig. 8-6b, the wall may move to the right from position 1'. If the field is large enough, it may reaches the position x_0 where the stress gradient changes at a slow rate or where stress gradient become constant (in the latter case, the wall can move continously to the right without any further increase of field until it encounter a bigger potential barrier.

Now assume that the microstress is arbitrary distributed through out the material, and some stress minimum are

deep with high stress gradient and some are "shallow" with "lower" stress gradient. Thus by applying the field, The number of domain walls that can reach the point x_0 where stress gradient changes is increased (the domain walls that are released from the microstress minimum are assumed not be able to overcome strong "pinning" humps which may be caused by inclusions), the results is the increasing of net flux reversal per unit of field strength, ie, the higher the H_m, the higher the amplitude permeability.

In summary, the motion of domain walls under the influence of an applied magnetic field is impeded by the presence of pinning sites in the solid such as non-magnetic inclusions and volids, dislocations or regions of inhomogeneous micro-stress. Here we concern with the nature of these imperfections and distinguish them into two kinds of pinning sites: The "weak" pinning centers which may be due to micro-stress and the "strong" pinning centers which may be due to inclusions, etc. The increasing of domain walls that are de-pinned from the "weak" pinning sites is responsible for the increasing in permeability in the region below H_t as the amplitude of measuring field increases. The role of domain walls that are pinned in the "strong" pinning sites will be described in the following section.

8.3.2 Inductance in The Region Above the Critical Field.

The following interpretation is adapted from the general literature [Ch64, Cu72, Bo51], except that we emphasis the role of critical field in the model.

Assume that above H_t, the strong-pinned domain walls begin to de-pin from the strong traps, and let the local critical field by which the wall can get over one hump be H_0, which is given by Eq.(8-17). We assume that this pinning strength of the pinning centers are evenly distributed, say, the number of humps, which have a critical field from H_0 to $H_0 + dH_0$, is equal to $f_0 dH_0$, where f_0 is the proporional constant. Then when the field strength increases from H to H+dH, the number of domain walls that change from category 1 to category 2, should be proportional to $f_0 dH$. This means that the higher the amplitude of the applied field, the higher the number of domain walls can overcome energy barriers and become released, i.e., The number of domain walls in category 1 decreases while the number of domain walls in category 2 increases as the field increases.

We now take a look at how the average domain displacement of the walls in category 2 might increase as field increases.

As can be seen from Fig. 8-5, with an increase of the field strength, the point indicated the position of the domain wall rises along the hump and is discontinuously displaced from the maximum to the next hump, say to c. with further increase of H, the point displaces from c to d -> e -> f, thus each stroke of such an irreversible displacement is longer for a stronger magnetic field, for the humps which are lower than those that have already been got over by the wall are not useful in sustaining the wall.

Thus, we can assume that the average of such a stroke of the displacement is proportional to the number of humps having H_0, which is less than the applied field H, i.e,

$$\int_{H_t}^{H} f_0 dH_0 = f_0(H - H_t). \tag{8-31}$$

From the above analysis, we can see that the irreversible magnetization resulting from this process should be proportional to (the number of displaced walls) x (average distance of one stroke of irreversible displacement) and is

$$dM_{irr} = cf_0^2(H - H_t)dH, \tag{8-32}$$

where c is a proportional factor. The irreversal magnetization cause by the change of the field from H_t to H is thus given by

$$M_{irr} = \int dM_{irr} = cf_0^2 \int (H-H_t)dH = \frac{1}{2}cf_0^2(H^2+H_t^2-2HH_t). \tag{8-33}$$

This indicate that permeability increases as H increases and the increasing is due to irreversible magnetization processes.

8.4 The Magnetization at High Fields

We have found in chapter 6 that at high fields, the magnetization curve of the materials conforms more or less to the Frolich-Kennelly relation:

$$\frac{1}{\mu} = a + bH_m \tag{8-34}$$

Since B = μ H, Eq. (8-34) can be rewritten as follows:

$$B = \frac{H}{(a+bH)} = \frac{1}{a/H + b} =$$

$$\frac{1}{b}(1 - \frac{a}{bH} + \frac{1}{2}(\frac{a}{bH})^2) = B_s(1 - \frac{B_1}{H} + \frac{B_2}{H_2}) \qquad (8-35)$$

with B_s = 1/b . This equation is closely related to the equation

$$\frac{M}{\mu_0} = \frac{M_s}{\mu_0}(1 - \frac{A}{H}) \qquad (8-36)$$

used by Weiss [We10] for extrapolation to determine the value of M_s. Equation (8-36) shows that the plotting of $(M/\mu_0)H$ versus H should be a linear relation with slope M_s/μ_0 and intercept M_sA/μ_0. Figures 8-7 and 8-8 show these relations for ferrite, Metglas as examples. The result for core #6 is not shown here. The value of M_s/μ_0 for the three materials are 3.28 x 10^5 ,1.22 x 10^6, 6.74 x 10^6, and A is 12.2, 40.2, 2.83 for ferrite, Metglas, and core #6 separately. The physical meaning of equation (8-36) has been studied by many authors [Ch64, p.274, Bo51, p.484, Cu72, p.347]. The most successful explanation is made by Neel [Ne48]. Neel has shown that Eq.(8-36) is only valid in certain field range. For example, if it is still valid up to saturation, the work of magnetization will be infinity, which is not physical plausible. To explain Eq.(8-36), Neel suggested that the effect of applied field on magnetization may arise from the presence of cavities of non-ferromagnetic inclusions, and the average states of magnetization is
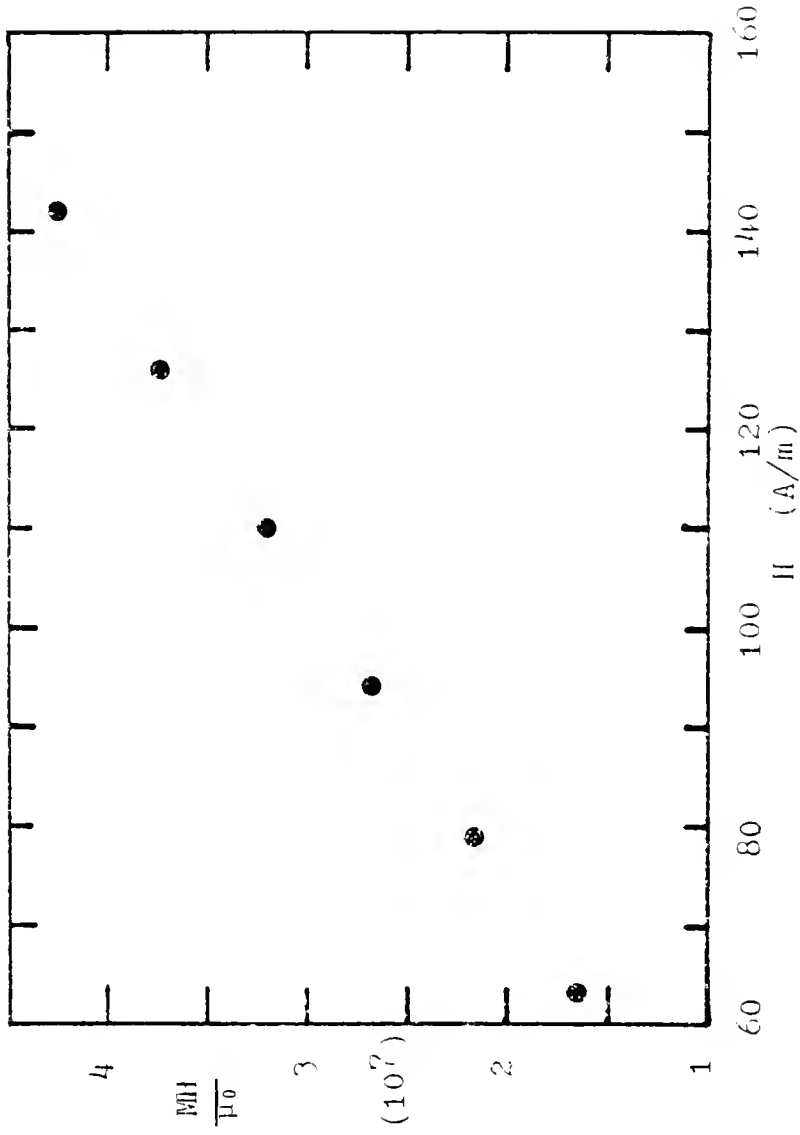
Fig. 8-7 (MH)/μ_0 vs H of ferrite.
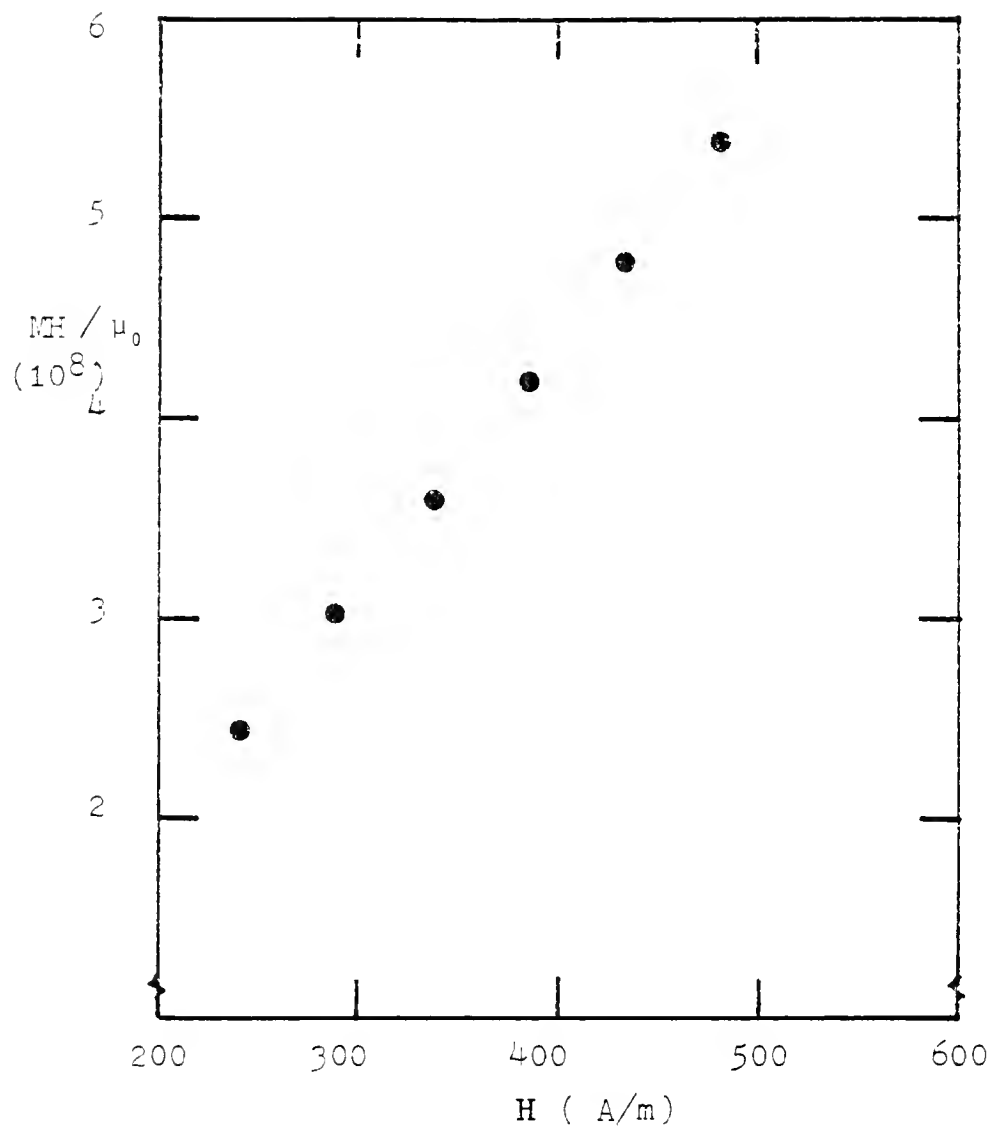
Fig. 8-8   (MH)/μ_0 vs H at high fields. (Metglas)

determined by the applied field and internal fields due to the cavities. His complicated calculation shows proportionality with 1/H in certain field range, and the absolute value of A is derived as a function of amount of cavities or inclusions. At high field range, his limiting form of expression shows the law of approach to saturation is linear with $1/H^2$.

Neel's theory is believed to be a success in explaining the law of approach to saturation. It is interesting to note that Eq.(8-36) described the B-H relation of the three materials quite well. This may be due to the fact that nonmagnetic cavities or inclusions are always present in material no matter what chemical and physical properties of the material are.

8.5 Summary

In summary, this chapter offers explanations for the experimental results on normal inductance of six materials. A new "instantaneous" inductance model is proposed to explain normal inductance and to predict harmonic distortion. Measured distortion was less than is predicted by the model, but was in reasonable agreement with a domain-state interpretation of the Rayleigh model.

The low field inductance is explained as due to the displacement of the domain walls near microstress minima, which may arise from dislocations, and due to displcement of the domain walls that are strongly pinned at traps. The

increasing of permeability with increasing field strength in the low field region below H_t is explained as due to the increase of the number of domain walls that are released from the weak traps of microstress minima. The increasing of the permeability at a different rate with increasing field strength in the second region, where $H_m > H_t$, is explained as due to the increasing of the number of domain walls that are "de-pinned" from the "strong" traps like those of inclusion defects. Once a domain wall is released from the trap, it could have a long jump of irreversible displacement, thus increases the volume of flux reversal per unit of field strength. The combination of increase of released domain wall numbers and increase of average length of displacement of such a domain wall gives rise the increasing of permeability. The above ideas were developed by many authors [Pr35, Ne42, Cu72] and were adapted in this chapter to explain the normal inductance. However, the difference of the nature between "weak" and "strong" pinning sites are emphasized in this chapter. These two kinds of traps are usually lumped as "traps" in the literature. The distinction between the two may help us to understand why there are two regions in which permeability increases with increasing field at two different rates.

CHAPTER 9
A PLAUSIBLE MODEL OF INCREMENTAL INDUCTANCE

In this chapter, a model is proposed to explain the experimental results of incremental inductance measurements.

9.1 Introduction

Our experimental measurements of incremental inductance of magnetic cores revealed that for each material studied, there is a critical field, H_d, below which incremental inductance is nearly a constant (first region), and above which the incremental inductance decreases linearly as the bias field increases (second region). No physical model has been derived to explain these observations.

Bozorth [Bo51] has mentioned that the incremental permeability is a measure of the "firmness" with which the domains are held in position by the biasing field. But quantitative evaluation is hard to do due to the stabilities of various domains differ widely from each other. Watson [Wa81] has shown that experimental data for incremental inductance did not fit a rotational model. The theory of incremental inductance is not yet complete.

In this chapter, a model is proposed to explain incremental inductance. This model suggests that the parameter S, the total area of the domain walls included in

a unit volume, plays an important role to determine the incremental permeability of the material, and this parameter S is assumed to be controlled by the d-c bias, while small a-c field is assumed to cause the domain walls to displace sinusoidally at their equilibrium positions.

Before presenting the model, possible reversal mechanisms that determine the permeability of the material under small a-c excitation are described first since they are related to our model. These reversal mechanisms are adapted from the book by Chikazumi [Ch64].

9.2 Reversal Mechanisms Under Small a-c excitation

The mostly likely mechanisms of reversible magnetization changes under small a-c excitation are reversible rotation magnetization, reversible domain wall motion, and domain wall bowing. The rotation mechanism usually underestimate the initial permeability of the material [Ch64, p.263], and this mechanism is considered to be significant only at high fields, thus this mechanism is neglected at small fields and will not be discussed here.

9.2.1   Reversible Wall Displacement.

In Eq.(8-14), if the frequency is not high, the first and second terms are usually neglected to simplify the analysis of the motion of the wall [Ch64, p.265, Pr58]. Thus the solution of Eq.(8-14) is

$$x = \frac{2M_s \cos\theta}{d} H \qquad (9\text{-}1)$$

As a result of this displacement x of the wall the magnetization in the direction of the magnetic field increases by the amount $2 M_s(\cos\theta)x$, And the total change of magnetization is given by

$$M = \frac{4M_s^2 \cos^2\theta}{d} SH, \qquad (9\text{-}2)$$

where S is the total area of the 180° wall in a unit volume, the susceptibility is ,therefore

$$\chi_i = \frac{4M_s^2 \cos^2\theta}{d} S \qquad (9\text{-}3)$$

For a cubic crystal with either positive or negative K_1, or when the easy axes are distributed isotropically, the average of $\cos^2\theta = 1/3$ [Ch64 p.267] (the 1 mil core with tranverse anneal may have a higher value of this average), thus the initial susceptibility

$$\chi_i = \frac{4M_s^2}{3d} S \qquad (9\text{-}4)$$

THe susceptibility is in proportional to the total area S of the 180° degree domain walls in a unit volume. The susceptibility due to the motion of 90° walls is similar to that of Eq.(9-4), and will not be described here.

A conceivable origin of the fluctuation in the energy of a domain wall as shown in Fig. 8-4 is the internal stress; others are nonmagnetic inclusions, precipitates, and voids [Ch64, p.271, Te69, p.379].

A domain wall displacement model has been used to cal-culate the initial permeability of mild steel or iron and was found in fair agreement with experimental data. [Ch64 p.271].

9.2.2 Domain Wall Bowing

Consider, a 180° wall is fixed at both ends as shown in Fig. 9-1. When the field H is applied in a direction which makes an angle θ with the direction of domain magnetization, the 180° wall tends to move so as to increase the volume of the domain with positive magnetization. If a part of the wall with area S is displaced by the distance s, the work done by the field is given by

$$E = -2M_s H(\cos\theta)Ss \qquad (9-5)$$

Then the force exerted on a unit area of the wall is

$$P = \frac{-1}{S}\frac{\partial E}{\partial s} = 2M_s H\cos\theta \qquad (9-6)$$

Thus the action of a magnetic field is equivalent to an exertion of pressure on the magnetic wall. The wall is bent into a cylindrical form due to the pressure as shown in Fig. 9-1, it radius of curvature, r, is related to the field H by

$$\frac{\gamma}{r} = 2M_s H\cos\theta \qquad (9-7)$$

where γ is the surface energy of the wall. The change in the volume of the domain with the positive magnetization is
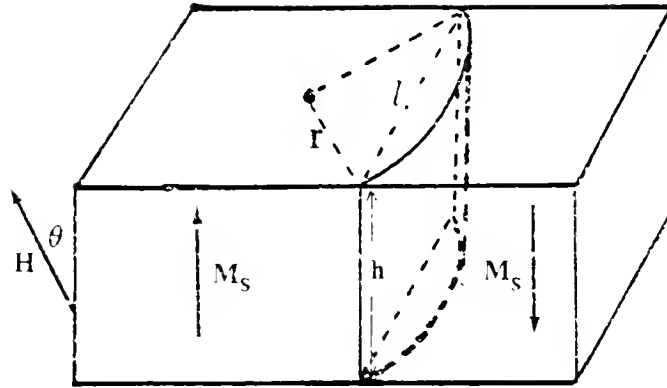
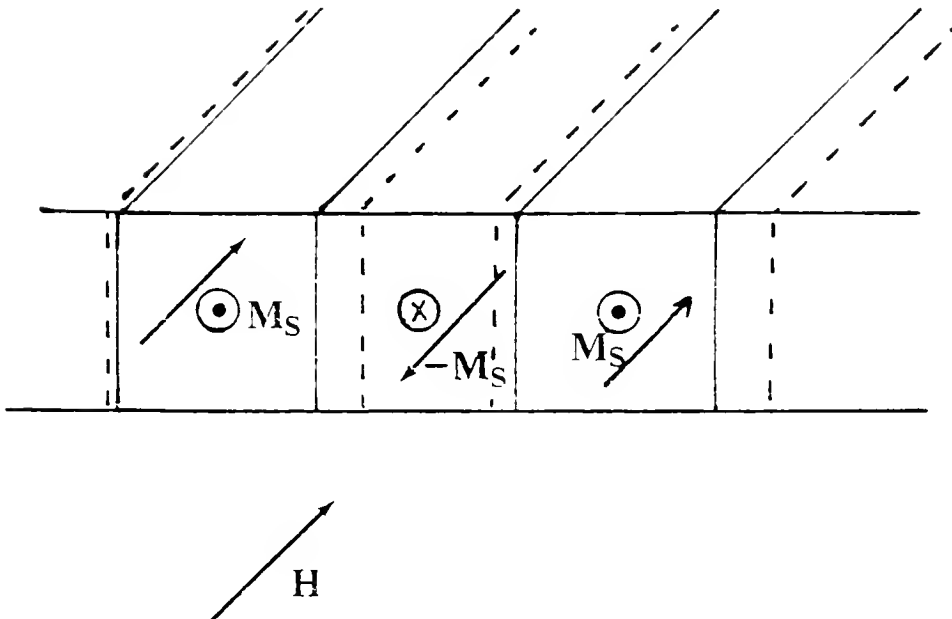Fig. 9-1   A 180° wall bowing under the action of a magnetic field.

Fig. 9-2   Domain wall displacement under d-c bias.

$$\delta V = \frac{2}{3}lhs, \qquad (9-8)$$

where h is the height of the wall, and l the distance between the two constrained portions of the wall. The increase in the magnetization is thus given by

$$M = \frac{4}{3}M_s(\cos\theta)Ss \qquad (9-9)$$

where S is total area of the domain wall included in a unit volume.

By using the geometrical relation,

$$s = \frac{l^2}{8r} \qquad (9-10)$$

then

$$M = \frac{Sl^2M_s^2}{3\gamma}(\cos^2\theta)H \qquad (9-11)$$

The average $\cos^2\theta$ is 1/3 in most cases, the susceptibility becomes

$$\chi = \frac{Sl^2M_s^2}{9\gamma}. \qquad (9-12)$$

Thus the higher the total area of the domain wall included in a unit volume, the higher the susceptibility. A similar results of Eq.(9-12) can be derived for 90° walls and will not be repeated here.

Domain wall bowing model has been used to calculated the initial permeability of pure iron, and was found that

the model gives a fairly large permeability compared to the rotation magnetization [Ch64, p.271].

It should be noted that it is not our major concern to identify any of the above mechanisms to be responsible for the magnetization under small a-c excitation. Our emphasis is on the role of d-c bias on the magnetization with small a-c excitation , which may be responsible for the incremental inductance behavior of the material. A model of incremental inductance with emphasis on the role of d-c bias, is given as follows with 180° walls as an example. This model also can be applied to 90° domain walls.

9.3   The Model

Assume that in the material there exist mainly 180° domain walls forming a bar-shape domain structure and the wall are perpendicular to the surfaces of the sheet and the magnetization of domains is in parallel with the surface (Fig.9-2). When d-c bias $H_{dc} > H_d$ is applied, some domains are displaced to a new equilibrium position. Some domain walls are still pinned, some can be displaced to a long distance, and some only can be displaced to a short distance. A pair of domain walls may vanish if two domains come across each other due to the applied field, H_{dc}. Thus this model argues, the higher the d-c bias, the fewer the number of domain walls per unit volume exist in the material.

According to this model, when H_{dc} is smaller than H_d, most of the domains are pinned, and the parameter S of the material is nearly a constant. And when H_{dc} is higher than

H_d, S begins to decrease. We also make the assumption on the behavior of the domain walls under small a-c excitation as follows: We assume that the behaviour of walls is ideal: the inertia and the relaxation damping of their motion are negligible, and the interactions between domain walls are negligible. We assume the domain walls are tickled sinusoidally at the same frequency of the applied a-c excitation such that the total flux reversal depends on the total number of domain walls participating in reversal: the larger the number of domain wall area per unit volume S in the material, under the same specified level of H_{ac} excitation, the larger the total volume of flux reversal, the result is the larger the value of incremental inductance. These assumptions of a-c excitation are consistent with our description of reversal models in section 9-2. Thus,when H_{dc} is smaller than H_d, the incremental inductance would be a constant, while for H_{dc} larger than H_d, the inductance decreases.

To verify our assumptions, consider the following physical behaviour of the material: In a conducting material containing domains, the eddy currents are localized at the moving walls as can be seen from Fig. 9-3, and the eddy-current density, J, can reach very large values at the walls. At a specified value of B_m of a-c excitation, the average value of $J^2\rho$ over the specimen is then larger than if the eddy currents were evenly distributed throughout. In other words, the larger the domain size, the less number of
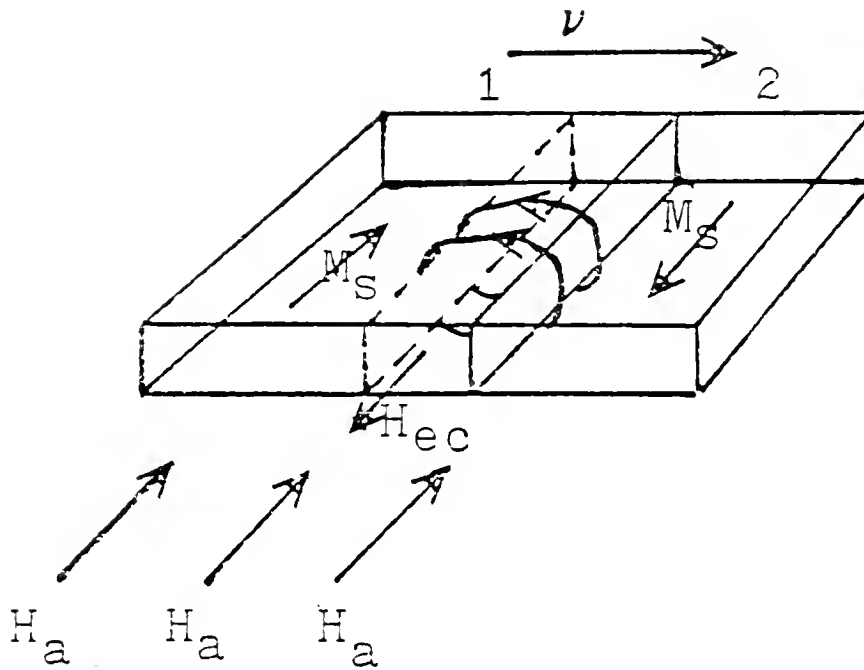
Fig. 9-3   Micro eddy current associated with a moving wall.

the walls and the faster they have to move to accomplish a given constant net flux change ($\triangle\phi$) at a given frequency, the result is a larger eddy current loss. On the other hand, if the small a-c excitation is kept at constant H_m, the less the area of domain walls per unit volume, the less the power loss. The following measurements were made to support the model.

9.4 Measurements to Support Model

Measurements of inductance, eqivalent series resistance R, quality factor Q and the a-c current I(rms) needed to excite the material at a specified B_m, were made on each of the four inductors wound on different magnetic materials as a function of d-c bias. The total power loss P_t of the inductor is calculated according to the following equation:

$$P_t = I^2_{rms} R \qquad (9-13)$$

where I_{rms} is the current(rms) in the inductor and R is the series resistance. The total loss includes eddy current loss, hysteresis loss and copper loss. The copper loss P_c can be estimated by the equation.

$$P_{copper} = I^2_{rms} R_w, \qquad (9-14)$$

where R_w is the resistance of the winding. The hysteresis loss is estimated according to the model by Rayleigh (Ch64, p.297, O166, p.54)

$$P_h = \frac{4}{3}\mu_0 \sqrt{H_m^3} Vf \quad \text{(watts)} \qquad (9\text{-}15)$$

where $\sqrt{}$ is the Rayleigh constant, and V is the total volume of the material in m^3. The eddy current loss P_e is then

$$P_e = P_t - P_c - P_h . \qquad (9\text{-}16)$$

The results are shown in Figs. 9-4 through 9-7 with ferrite Metglas, core #8, and core #6 as examples. All the results show that P_e is nearly a constant when H_{dc} is smaller than the critical field H_d, and is found to increase as H_{dc} is above H_d.

In Fig. 9-4, the power loss of ferrite as a function of d-c bias at constant H_m a-c excitation is also shown. Fig. 9-8 shows the result for core #8. In each case, the power loss decreases as d-c field is above H_d.

9.5 Conclusion

D-c bias on a inductor core reduces the a-c permeability of the material. A model is proposed to explain these observations based on the assumption that d-c field reduce the total area of the domain walls per unit volume of the material, and the superposed small a-c signal tickles the domain walls sinusoidally. It is assumed that the area of domain walls per unit volume of the magnetic material decreases as d-c field increases beyond a critical field. This model is consistent with the observation that the eddy current power loss at small constant B_m excitation,
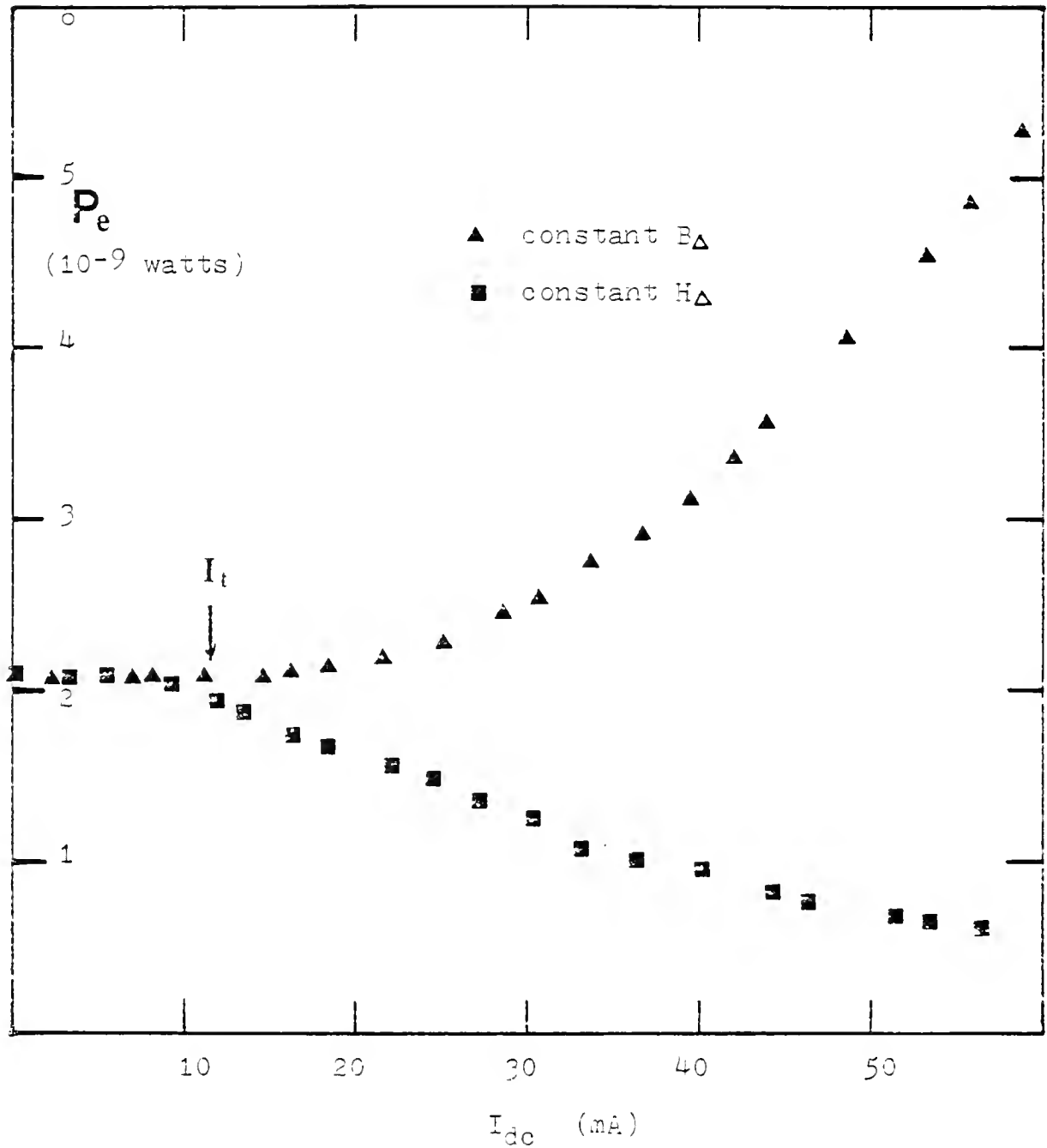
Fig. 9-4 Power loss of ferrite core under small constant
a-c field and constant flux excitations, plotted
as a function of d-c bias.

Fig. 9-5   Power loss of Metglas core under constant a-c flux excitation plotted as a function of d-c bias.

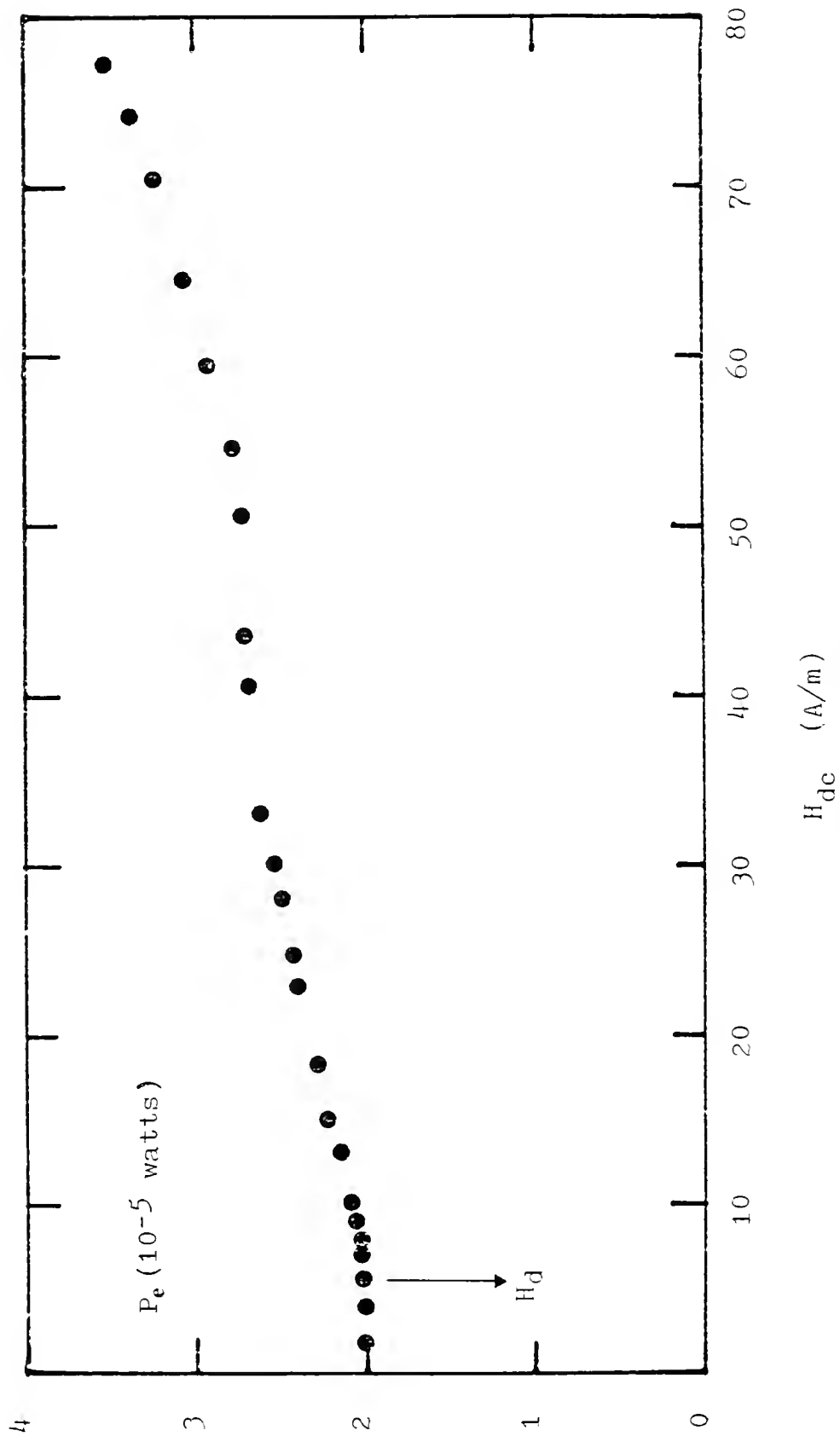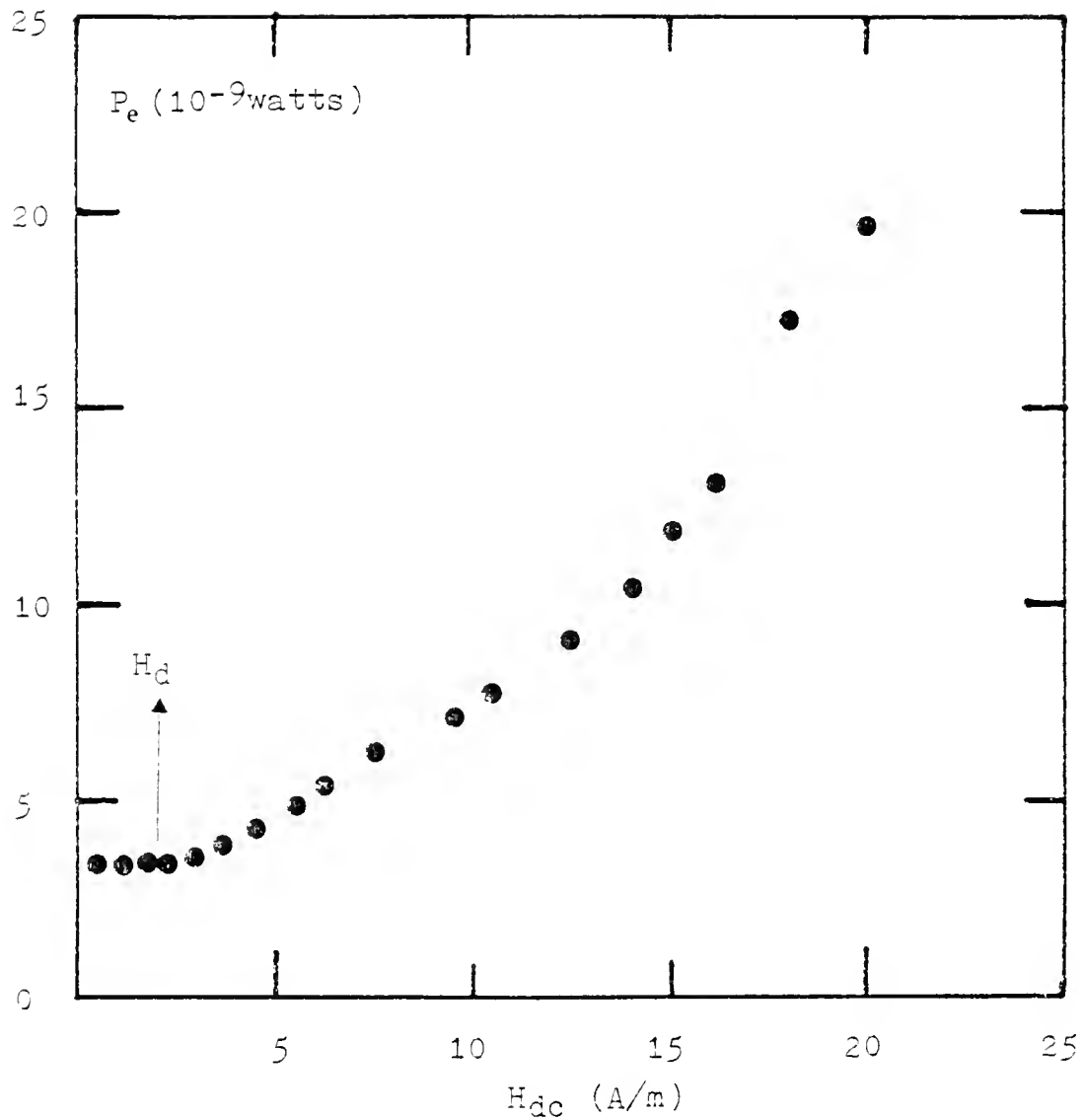Fig. 9-6 Power loss under constant a-c flux excitation
plotted as a function of d-c bias. (core #8)
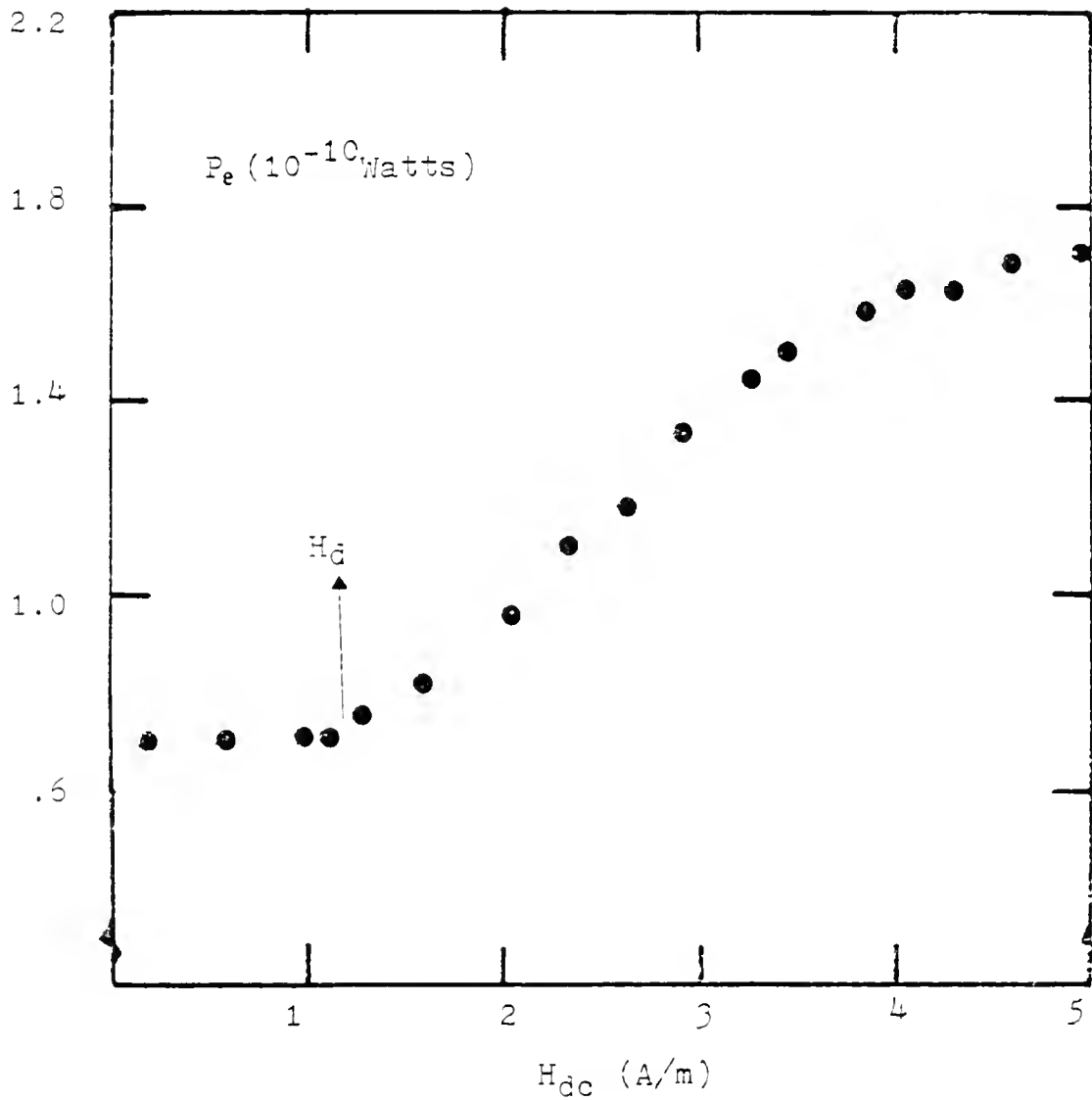
Fig. 9-7 Power loss of core #6 under a specified a-c flux
excitation, plotted as a function of d-c bias.
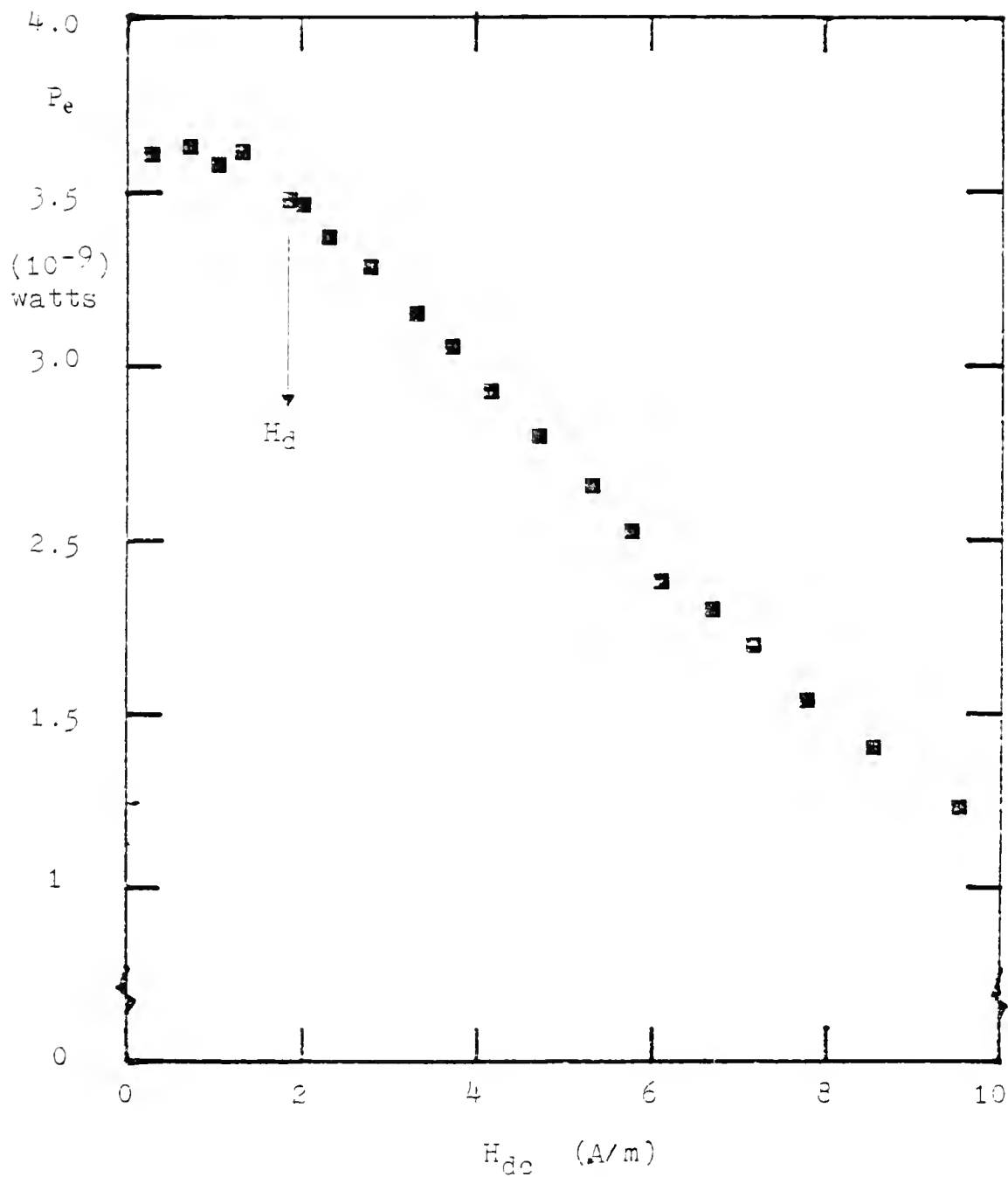
Fig. 9-8   Power loss of core #8 under small constant
H_{ac} excitation as a function of d-c bias.

increases as d-c bias increases beyond the critical field. The increase of power loss is interpreted as due to the concentration of local eddy current. The model is also consistent with the observation that at small constant H_m a-c excitation, eddy current loss decreases as d-c bias increases above the critical field where the total area of the domain walls per unit volume is assumed to begin to decrease.

.

CHAPTER 10
CONCLUSION

This dissertation has studied the modeling and characterization of inductors wound on the following core materials in toroidal form: a ferrite, an amorphous alloy (Metglas$^{\text{®}}$), a permalloy 4 mil tape wound core (core #6), three permalloy 1 mil tape-wound cores (core #1, #8 and #14) with various kinds of heat treatment.

Magnetic properties of the cores were investigated by normal inductance measurements, incremental inductance measurements, effective series resistance measurements, inductance quality factor measurements, B-H loop observations, and measurements of waveform distortion.

The major findings from this study may be summarized as follows:

For each material, the normal inductance was found to initially increase in proportion to signal amplitude, but eventually passed through a maximum. The measurements of incremental inductance show that for each material, there is a critical field below which the incremental inductance is independent of the biasing current and above which the incremental inductance decreases rapidly as direct current is increased.

A correlation between the two inductance measurements (normal and incremental) was observed for each core material: the d-c critical field was found to be equal to the peak a-c field at which a change was observed in the proportional increase of normal inductance. The critical field, H_r, is believed to define a threshold condition for a change of the process of core reversal.

A new "instantaneous" model of permeability was used to predict the amount of odd-harmonic distortion of inductor voltage waveforms. Experimental data were found to agree more closely with a domain state interpretation of Rayleigh's model.

A new mathematical model for inductance and effective series resistance was used successfully to calculate quality factor and power loss of inductors, and to derive an expanded form of Legg's equation. The model was demonstrated for specific inductors by using a computer curve-fitting program to evaluate accurate model coefficients from experimental data.

Other findings can be summarized as follows:

1. An experimental technique was derived for judging the relative volume density of domain walls. This method was used to support a model for domain wall density in measurements of incremental inductance.

2. Even in the low B_m range, the term "e" of Legg's equation was found to increase as B_m increases. Thus,

Legg's equation needs to be modified by adding a cross product term "d" to extend its application.

3. A second limitation of Legg's equation occurs when the term $aB_m + c$ as a function of B_m shows concave-down such that the term "a" is hard to define.

For further study, we recommend the following works:

1. A two-dimensional regression program may be used to analyze the data of L and of ESR of an inductor as a function of B_m and/or frequency (analyzed by B_m and f simultaneously) that probably can yield a more general mathematical model for the inductors.

2. We have mentioned in chapter 2 that the parameters "a" (hysteresis coefficient) and "d" (coefficient of cross product term) of an inductor increase as the number of turns of winding of an inductor increases. A quantitative study of this relation could be made. Also, geometry effects on the parameters have not been addressed; they are recommended to be done.

3. Direct domain wall observations on bulk materials are recommended to relate to the device performance, especially for the domain behavior around the critical field H_r and around H_{mm} where normal inductance has a maximum.

REFERENCES

[Ah59]: A. Aharoni, "Some Recent Developments in Micromagnetics at the Weizmann Institute of Science," *J. Appl. Phys.,* 30 (April, 1959), pp. 70S-78S.

[Ba19] H. Barkhausen, "Two Phenomena Uncovered with Help of the New Amplifiers," *Physik. Z.,* 20 (1919), pp. 401-403.

[Bo51] R.W. Bozorth, *Ferromagnetism.* D. Van Nostrand Co., Inc., New York (1951).

[Bo81] R. Boll and H. Warlimont, "Applications of Amorphous Magnetic Materials in Electronics," *IEEE, Tran. Mag.,* 17, No.6 (Nov., 1981). pp. 3053-3058.

[Br59] W.F. Brown, "Micromagnetics: Domain Walls," *J. Appl. Phys.,* 30(S), No.4 (April, 1959), pp. 62S-69S.

[Ch64] S. Chikazumi, *Physics of Magnetism.* Wiley, New York (1964).

[Cu72] B.D. Cullity, *Introduction to Magnetic Materials.* Addison-Wesley, London (1972).

[De80] R. M. Del Vecchio, "An Efficient Procedure for Modeling Complex Hysteresis Processes in Ferromagnetic Material," *IEEE Tran. Mag.,* MAG-16, No.5 (Sept. 1980), pp. 809-811.

[Jo24] H. Jordan, "Die ferromagnetischen Konstanten fur schwache Wechselfelder," *Elektr.Nachrichten Techn.,* 1 (1924), pp. 7-29.

[Ji83] D.C. Jiles and D.L. Atherton, "Theory of Ferromagnetic Hysteresis," Intermag-29th MMM Conference, Pittsburgh, Pennsylvania. Nov. 1983.

[Kr79] H. Kronmuller, M. Fahnle, M. Domann, H. Grimm, R. Grimm, and B. Groger. "Magnetic Properties of Amorphous Ferromagnetic Alloys," *J. Mag. Mag. Mat.,* 13, Nos. 1 & 2, (Sep. & Oct. 1979), pp. 53-70.

[Le36]   V.E. Legg, "Magnetic Measurements at Low Flux
         Densities Using the Alternating Current Bridge,"
         B.S.T.J., 15 (Jan. 1936), pp. 39-62

[Li81]   J.D. Livingston and W.G. Morris, "SEM Studies of
         Magnetic Domains in Amorphous Ribbons,"
         IEEE Tran. Mag., 17 (Nov. 1981), pp. 2624-2626.

[Ma73]   William A. Manly, Jr. "An Appraisal of Several Non-
         linear Hysteresis Loop Models," IEEE. Tran. Mag., 9,
         No.3 (Sept, 1973), pp. 256-260.

[Ma80]   Joseph A. Mas, "Design and Performance of Power
         Transformers with Metallic Glass Cores,"
         IEEE Power Electronics Specialists Conference
         (June,1980), pp. 68-79.

[Na80]   David Nathasingh and Carl H. Smith, "A New High-
         Flux, Low Magnetic Material for High Frequency
         Applications," Proceeding of Power Conversion, 7
         (March 25-27, 1980), pp. B2.1-B2.12.

[Ne42]   L.J. Neel, "Theory of Rayleigh's law of magnetiza-
         tion," Cahiers Phys., 12 (1942), pp. 1-20.

[Ne48]   L.J. Neel, "Law of Approach to Saturation and A New
         Theory of Magnetic Hardness," Phys. Radium [8], 9
         (1948), pp. 184-199.

[Ol66]   E. Olsen, Applied Magnetism, A Study in Quantities.
         Philips Technical Library, Springer-Verlag, New York
         (1966).

[Pe28]   E. Peterson, "Harmonic Production in Ferromagnetic
         Materials at Low Frequencies and Low Flux Densi-
         ties," B.S.T.J., 7 (1928), pp. 762-796.

[Pr35]   F. Preisach, "On Magnetic Lag," Z. Physik, 94
         (1935), pp. 277-302.

[Pr58]   R.H. Pry and C.P. Bean, "Calculation of the Energy
         Loss in Magnetic Sheet Material Using A Domain
         Model," J. Appl. Phys., 29, No.3 (March, 1958),
         pp. 532-533.

[Ra87]   Lord Rayleigh, "On the Behaviour of Iron and Steel
         Under the Operation of Feeble Magnetic Forces,"
         Phil. Mag., 23 (1887), pp. 225-245.

[Ri81]   J. Rivas, J.M. Zamarro, E. Martin, and C Pereira,
         "Simple Approximation for Magnetization Curves and
         Hysteresis Loops," IEEE, Tran. Mag., 17, No.4 (July,
         1981), pp. 1498-1502.

[St54]   K.H.   Stewart,   Ferromagnetic Domains.   Cambridge
         Press, London (1954).

[Te69]   R.S.   Tebble,   D.J.   Craik,   Magnetic Materials.
         Wiley-Interscience, London (1969).

[Ts79]   H. Tsunekawa, A. Nakata, T. Kamijo, and K. Okutani,
         "Microstructure and Properties of Commercial Grade
         Manganese Zinc Ferrite," IEEE. Tran. Mag., 15, No.6
         (1979), pp. 1855-1860.

[Wa80]   J.K.   Watson,   Applications of Magnetism.   Wiley-
         Interscience, New York (1980).

[Wa81]   J.K. Watson, "On the Nonlinearities of Inductors
         using   Linear   Ferrite   Toroidal   Core,"
         IEEE Tran. Mag., 17 (May, 1981), pp. 1320-1325.

[We07]   P. Weiss, "Hypothesis of the Molecular Field and
         Ferromagnetic properties," J. Phys., 6 (1907), pp.
         661-690.

[We10]   P. Weiss, "Absolute Value of Intensity of Magnetiza-
         tion at Saturation," J. Phys., 9 (1910), pp. 373-
         393.

[Wi37]   H.J. Williams, "Magnetic Properties of Single Cry-
         stal of Si-Fe," Physics Review, 52 (1937), pp. 747-
         751.

[Wi49]   H.J Williams, R.M. Bozorth, and W.Shockley, "Mag-
         netic Domain Patterns on Singal Crystals of Silicon
         Iron," Phys. Rev., 75 (1949), pp. 155-178.

BIOGRAPHICAL SKETCH

Long-Ching Yeh was born in Taipei, Taiwan, Republic of China (R.O.C.), on November 10, 1949. He received the B.S. degree in physics from National Taiwan Normal University, Taiwan, in 1973, and the M.S. degree from National Tsing Hua University, Taiwan, in 1975. From 1975 to 1977, he was in military service. He worked as an instructor at Long-Hua Technical College in 1978 and worked as an instructor at National Taiwan Institute of Technology from 1978 to 1980. Since 1980, he has been working toward his Ph.D. degree at the University of Florida, Gainesville, Florida.

I certify that I have read this study and that in my opinion it conforms to acceptable standards of scholarly presentation and is fully adequate, in scope and quality, as a dissertation for the degree of Doctor of Philosophy.
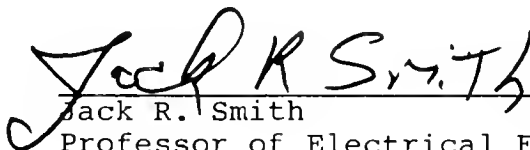
J. Kenneth Watson, Chairman
Professor of Electrical Engineering

I certify that I have read this study and that in my opinion it conforms to acceptable standards of scholarly presentation and is fully adequate, in scope and quality, as a dissertation for the degree of Doctor of Philosophy.
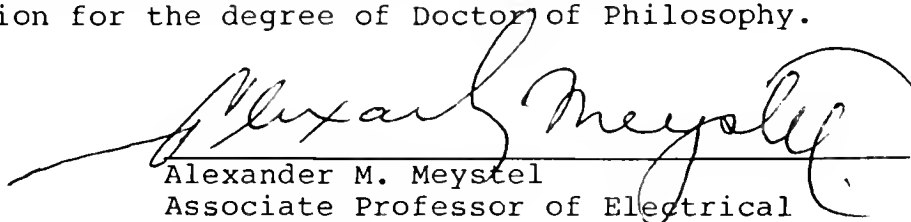
Sheng S. Li
Professor of Electrical Engineering

I certify that I have read this study and that in my opinion it conforms to acceptable standards of scholarly presentation and is fully adequate, in scope and quality, as a dissertation for the degree of Doctor of Philosophy.

Jack R. Smith
Professor of Electrical Engineering

I certify that I have read this study and that in my opinion it conforms to acceptable standards of scholarly presentation and is fully adequate, in scope and quality, as a dissertation for the degree of Doctor of Philosophy.

Alexander M. Meystel
Associate Professor of Electrical Engineering

I certify that I have read this study and that in my opinion it conforms to acceptable standards of scholarly presentation and is fully adequate, in scope and quality, as a dissertation for the degree of Doctor of Philosophy.

Pradeep P. Kumar
Associate Professor of Physics

This dissertation was submitted to the Graduate Faculty of the College of Engineering and to the Graduate Council, and was accepted as partial fulfillment of the requirements for the degree of Doctor of Philosophy.

December, 1984

Dean, College of Engineering

Dean, Graduate School